DYNAMICS OF ELECTRONIC EXCITATIONS AT C$_{60}$ SURFACES AND INTERFACES STUDIED BY SECOND-HARMONIC GENERATION

THÈSE N° 1502 (1996)

PRÉSENTÉE AU DÉPARTEMENT DE PHYSIQUE

ÉCOLE POLYTECHNIQUE FÉDÉRALE DE LAUSANNE

POUR L'OBTENTION DU GRADE DE DOCTEUR ÈS SCIENCES

PAR

René BECKER

Diplom-Physiker, Ruprecht-Karls-Universität, Heidelberg, Deutschland
de nationalité allemande

acceptée sur proposition du jury:

Prof. K. Kern, directeur de thèse
Dr M. Buck, corapporteur
Prof. M. Chergui, corapporteur
Dr W. Daum, corapporteur
Dr K. Kuhnke, corapporteur

Lausanne, EPFL
1996

Résumé

L'excitation électronique aux surfaces et interfaces est étudiée par Génération optique de la Seconde Harmonique (SHG). Dans ce but, un système OPG/OPA (Optical Parametric Generation / Optical Parametric Amplifier) a été construit. Ce système génère des impulsions laser de durée de l'ordre de quelques picosecondes dont la longueur d'onde peut être variée de manière continue entre 0.4 et 2.4 μm.

La réponse non-linéaire des surfaces solides de C_{60} ayant diverses qualités cristallines et le comportement de la génération de la seconde harmonique pour des états électroniques excités sont étudiés. L'anisotropie azimutale du signal de la seconde harmonique, qui n'est pas observable dans le cas de films minces polycristallins, est mesurée pour la surface (111) d'un monocristal fcc. La suppression du signal de la seconde harmonique sous l'effet d'impulsions lumineuses de courte durée dans le domaine où l'absorption optique est efficace, est étudiée. Ce déclenchement de l'efficacité de la SHG est étudié en détail et il a été trouvé qu'elle a son origine dans la présence d'excitons près de la surface du solide. En utilisant la méthode "pump and SHG-probe", l'excitation et la relaxation de l'état excitonique excité vers l'état fondamental peuvent être observées. L'état est peuplé plus vite que la résolution temporelle expérimentale de 45 ps ne permet de l'observer. Le temps de vie de l'exciton a été déterminé comme étant plus grand que 20 ns mais plus petit que 20 ms. A une interface quartz/C_{60} , le temps de vie est réduit à 70 ps. Le couplage de l'état excité avec le substrat conduit à une réduction du temps de vie.

Un système consistant en un sandwich métal-isolant-C_{60} est présenté. La base de ce système (métal-isolant) consiste en une couche d'espacement de molécules organiques auto-organisées à la surface d'un film mince presque parfait d'Au(111). Les molécules de C_{60} déposées ensuite sur cette couche sont électroniquement découplées du système métallique. Cependant, la relaxation de l'exciton vers l'état fondamental est déterminée par la présence du métal. En variant l'épaisseur de la couche d'espacement, la distance d entre la couche de C_{60} et le substrat métallique peut être variée dans un domaine de 10 à 30 Å. Il a été trouvé que le temps de vie décroît de 500 ps (30 Å) à 60 ps (10 Å). Le transfert non-radiatif d'énergie est décrit par un comportement en d^{-3}, qui est en accord avec la théorie électromagnétique classique.

Abstract

The electronic excitation at surfaces and interfaces is studied by optical Second-Harmonic Generation (SHG). For this purpose an OPG/OPA (Optical Parametric Generator/Optical Parametric Amplifier) system is built, that generates picosecond laser pulses continously tunable in the wavelength range from 0.4 to 2.4 μm.

The nonlinear response of solid C_{60} surfaces of different crystalline quality and the behaviour of second-harmonic-generation of electronically excited states is studied. The azimuthal anisotropy of the SH signal, which is not observable for polycrystalline thin films, is measured for the fcc single crystal (111) surface. The quenching of the second-harmonic signal by short light pulses in the range of efficient optical absorption is investigated. This switching of the SHG efficiency is studied in detail and is found to originate from the presence of excitons near the surface of the solid. By using the pump-and-SHG probe scheme the excitation and relaxation of the excited excitonic state to the ground state can be monitored. The state is populated within the experimental time resolution of 45 ps. The lifetime of the exciton is found to be larger than 20 ns but less than 20 ms. At a quartz/C_{60} interface the lifetime reduces to 70 ps. The coupling of the excited state to the substrate leads to the lifetime reduction.

A metal-insulator-C_{60} sandwich system is presented. It is based on a spacer layer of self-organised organic molecules at the surface of a thin nearly perfect Au(111) film. C_{60} molecules deposited on top of this layer are electronically decoupled from the metal system. However, the relaxation of the exciton into the ground state is determined by the presence of the metal. By varying the thickness of the spacer layer the distance d to the metal substrate can be varied in the range of 10 - 30 Å. The lifetime is found to decrease from 500 ps (30 Å) to 60 ps (10 Å). The non-radiative energy transfer is described by a d^{-3} behaviour in agreement with classical electromagnetic theory.

ii

Table of contents

1. Introduction

Applications of lasers in solid state physics and chemical physics are progressing more and more since they are able to investigate systems in their "natural" environment. The investigation of surfaces under high gas pressures, in liquids, and the study of interfaces between solids has become possible. Research in the last decades was primarily focused on techniques requiring high vacuum. Optical spectroscopy is one of the few methods which can be employed under ambient conditions. However, these methods are suffering from little surface sensitivity. Second order nonlinear optics has overcome this problem, but requires lasers for the creation of strong fields without damaging the system under study. The development of repetitive short pulsed laser systems with pulses in the pico- and femtosecond range made this possible. The establishment of highly performing light sources by optical solid state technology in optical parametric generators (OPG) provided research groups with powerful, widely tunable laser. In addition the pico- and femtosecond pulse widths allow time-resolved studies.

This high flexibility in energy range and in time scale is accompanied by other advantages that make lasers a useful tool for the study of surfaces and interfaces. The use of nonlinear optics in surface science dates back to the 80ies. Its advantages are high surface sensitivity due to symmetry selection rules and wide areas of application where conventional methods do not have access as liquids and buried interfaces. Second Harmonic Generation (SHG) was in the past applied to many types of surfaces in UHV to study for example the kinetics of adsorption processes. The understanding of the underlying microscopic processes were in the beginning based on the comparison with the classical techniques. Another field of progress is the application of nonlinear techniques in electrochemical environments.

The third field of application of nonlinear optical techniques is relatively less explored: the area of buried interfaces. Solid C_{60} surfaces and interfaces and the SiO_2/Si interface can serve as model systems in this area because of their relatively well know studied electronical and structural properties. The results of this thesis show how a second-harmonic interface signal can be used to monitor chemical processes in real process environment. The main part will profit from the time resolution of the method to study picosecond changes of optical properties. Optical switching is of interest for possible application in future opto-electronic elements. The origin of this switching process, the dynamics of electronic excitations at the interface can be studied in pump-and-SHG probe experiments. At the same time these experiments allow to study the excited state properties of molecular and solid states near a metal substrate which have been a field of interest to study energy transfer. This gives information about the energy transfer mechanism to the substrate which is a subject of fundamental research.

The following chapters are organized as follows. A short introduction to nonlinear optics will be given in chapter 2. The tunable light source will be presented in chapter 3. Application of second-harmonic generation to the chemical modification at the silicon-silicondioxid interface is discussed in chapter 4. Chapter 5 introduces the preparation of solid C_{60} and shows first studies on the system. Second-harmonic generation measurements on C_{60} single crystals and the optical switching with short pulses will be presented in chapter 6. This effect will be explored in more detail in chapter 7 for thick films on quartz substrates. Chapter 8 demonstrates that for thin films on quartz a short lived state at the interface becomes observable. In chapter 9 the Au/thiol/C_{60} sandwich structure will be presented with its preparation and the dynamics at this interface will be discussed.

2. Experimental methods

In this chapter a short introduction into nonlinear optics will be given. In the first part the macroscopic Maxwell equations will be used to explain the origin of nonlinear optical effects. Usual approximations will be introduced in which certain nonlinear optical effects are easy to formulate. In the second part these results will be extended to the special situation of electromagnetic waves in nonlinear optical crystals and how they can be used for the creation of tunable laser radiation in the visible to near infrared region. The third part shows the essential elements of second-harmonic generation as a surface probe. How surface selection rules form the basis of the inherent surface sensitivity. A description of additionally used techniques in this study like Raman spectroscopy and the scanning tunneling microscopy (STM) can be found in the literature [1, 2].

2.1 Elements of nonlinear optics

Optical effects can be described macroscopically by the Maxwell equations in which the interaction of photons with the material is included by a macroscopic polarization $\bar{P}$. In the case of small electromagnetic fields generally the approximation

$$\bar{P} \propto \bar{E} \tag{2.1}$$

is made. Optical phenomena like absorption, interference and refraction will be described within this theory for macroscopic systems. A characteristic sign of linear optical effects is that the intensity does not play an essential role in their existence. If light waves are able to penetrate and pass through a medium, this occurs in this approximation without any interaction between the waves. However, new phenomena arise if the intensity of the electric field comes near the order of the atomic (molecular) fields of typically $\approx 10^{10}$ V m^{-1} [3]. To obtain an optical field of such a magnitude, an incident intensity of $\approx 10^{14}$ W cm^{-2} is required. Intensities of this magnitude can be achieved by focusing the powerful picosecond-duration pulses that are obtainable from mode-locked lasers. The interaction of photons with themselves in the material is the microscopic reason for these phenomena which have to be treated by quantum electrodynamical approaches. The simple oscillator picture might illustrate the underlying physics. An electromagnetic wave E passing through a material will interact with the existing charges (electrons or ions). Since the field is oscillating so will the charges. An oscillating charge will again create an electromagnetic wave P. In the model of a harmonic oscillator the frequency will be the same. So the whole situation can be described by a driven oscillator which has the form

3

$$m \left[\frac{d^2x}{dt^2} + 2\Gamma \frac{dx}{dt} + \Omega^2 x \right] = -eE(t) \tag{2.2}$$

where x is the displacement from the mean position, Ω the resonance frequency, and Γ a damping constant. By applying an oscillating force $E(t,\omega)$ to this system, the charge e will show an oscillating movement described by $x(t,\omega)$ with the same frequency as E and the linear polarization will be

$$\mu(t,\omega) = -e \cdot x(t,\omega) \tag{2.3}$$

or

$$P(t,\omega) = \chi \cdot E(t,\omega) \tag{2.4}$$

This is valid only for small fields. If we come into the range where the system does not respond anymore like a simple harmonic oscillator, we have to include further anharmonic factors, $\approx x^2$, $\approx x^3$, etc. into the potential of the oscillating system. In analogy to classical mechanics these "nonlinear" terms will distort the spring when the amplitudes of the oscillations become too high. The response $x(t)$, illustrated in figure 2.1 will show oscillation terms with different frequencies such as 2ω, 3ω,....

(a)   (b)
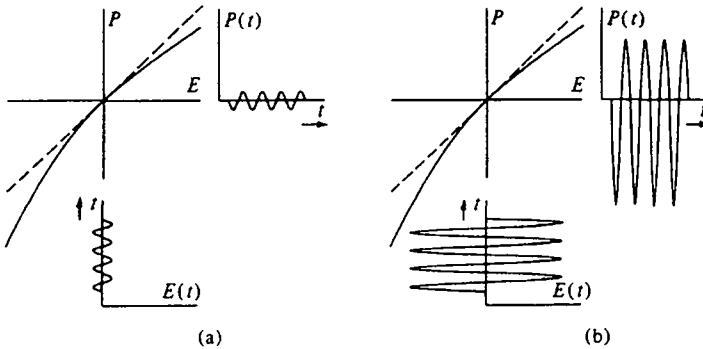
Fig. 2.1: The effect of a nonlinear dependence of the polarization P on the electric field E is shown. For small input fields (a), P does not depart significantly from a linear dependence (dashed line). At larger fields (b), the polarization has a distorted wave form which contains significant components at harmonic frequencies. From [3].

So the polarizability of the system for the electromagnetic wave will have the form

$$\bar{P}(2\omega) = \bar{\chi}^{(1)}(\omega) \cdot \bar{E}(\omega) + \bar{\chi}^{(2)} : \bar{E}(\omega)\bar{E}(\omega) + \bar{\chi}^{(3)} : \bar{E}(\omega)\bar{E}(\omega)\bar{E}(\omega) + ... \tag{2.5}$$

4

Each wave represents the electromagnetic field of a photon. Equation (2.5) can be understood in the way that $\bar{\chi}^{(1)}$ describes the interaction of one photon with the material, $\bar{\chi}^{(2)}$ of two photons and so on. This can be visualized in the Feynman graph of figure 2.2. A more detailed introduction can be found in review articles about nonlinear optical processes [4, 5] in which experiments and theoretical models are summarized. Table 2.1 gives an overview of nonlinear optical effects of different order in which the number of photons that contribute microscopically are listed. The most important group comprises the three photon processes (or three-wave mixing), which arise from the polarization term

$$\bar{P}^{(2)}(\omega_3) = \bar{\chi}^{(2)}(-\omega_3; \omega_1, \omega_2) \vdots \bar{E}(\omega_1) \bar{E}(\omega_2) \tag{2.6}$$

In the following we will restrict ourselves to these phenomena as example to outline the macroscopic theory of nonlinear optical effects. This term describes essentially all mixing phenomena including the generation of difference and sum frequencies which is illustrated in figure 2.2
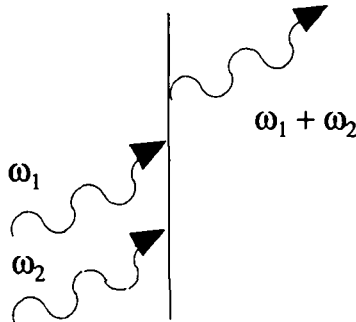

Fig. 2.2: Feynman diagram of three photon interaction. After [3].

Process	Order n	$-\omega_\sigma ; \omega_1, \ldots, \omega_n$	K
Linear absorption/emission and refractive index	1	$-\omega ; \omega$	1
Optical rectification (optically-induced d.c. field)	2	$0 ; \omega, -\omega$	$\frac{1}{2}$
Pockels effect (linear electrooptic effect)	2	$-\omega ; 0, \omega$	2
Second-harmonic generation	2	$-2\omega ; \omega, \omega$	$\frac{1}{2}$
Sum- and difference-frequency mixing, parametric amplification and oscillation	2	$-\omega_3 ; \omega_1, \pm\omega_2$	1
d.c. Kerr effect (quadratic electrooptic effect)	3	$-\omega ; 0, 0, \omega$	3
d.c.-induced second-harmonic generation	3	$-2\omega ; 0, \omega, \omega$	$\frac{3}{2}$
Third-harmonic generation	3	$-3\omega ; \omega, \omega, \omega$	$\frac{1}{4}$
General four-wave mixing	3	$-\omega_4 ; \omega_1, \omega_2, \omega_3$	$\frac{3}{2}$
Third-order sum- and difference-frequency mixing	3	$-\omega_3 ; \pm\omega_1, \omega_2, \omega_2$	$\frac{3}{4}$
Coherent anti-Stokes Raman scattering	3	$-\omega_{AS} ; \omega_P, \omega_P, -\omega_S$	$\frac{3}{4}$
Optical Kerr effect (optically-induced birefringence), cross-phase modulation, stimulated Raman scattering, stimulated Brillouin scattering	3	$-\omega_S ; \omega_P, -\omega_P, \omega_S$	$\frac{3}{2}$
Intensity-dependent refractive index, optical Kerr effect (self-induced and cross-induced birefringence), self-focusing, self-phase and cross-phase modulation, degenerate four-wave mixing	3	$-\omega ; \omega, -\omega, \omega$	$\frac{3}{4}$
Two-photon absorption/ionisation /emission	3	$-\omega_1 ; -\omega_2, \omega_2, \omega_1$ or $-\omega ; -\omega, \omega, \omega$	$\frac{3}{2}$ $\frac{3}{4}$

Table 2.1: Representative catalogue of nonlinear phenomena. From [3].

6

Armstrong et al. solved the nonlinear wave equation

$$\left[\bar{\nabla}\times\left(\bar{\nabla}\times\right)+\frac{1}{c^2}\frac{\partial^2}{\partial t^2}\right]\bar{E}(\bar{r},t)=-\mu_0\frac{\partial^2}{\partial t^2}\bar{P}(\bar{r},t)\qquad\text{with: }\mu_0=\frac{1}{\varepsilon_0 c^2}\qquad(2.7)$$

by applying the above mentioned Taylor series for the polarization up to the second order term. This leads to a system of coupled differential equations for the contributing fields at frequencies ω_j. Regarding the special case of three-wave-mixing the following amplitudes evolve for plane waves traveling in z-direction.

$$E_1\left(k_j,\omega_j\right)=A_1\cdot e^{i\left(k_j z-\omega_j t\right)}\qquad(2.8)$$

$$\frac{dA_1(z)}{dz}=\frac{i\omega_1}{cn_1}d_{eff}A_2^*(z)A_3(z)e^{-i\Delta k\cdot z}$$

$$\frac{dA_2(z)}{dz}=\frac{i\omega_2}{cn_2}d_{eff}A_1^*(z)A_3(z)e^{-i\Delta k\cdot z}\qquad(2.9)$$

$$\frac{dA_3(z)}{dz}=\frac{i\omega_3}{cn_3}d_{eff}A_1^*(z)A_2(z)e^{-i\Delta k\cdot z}$$

$$\text{with }\Delta k=k_3-k_1-k_2\qquad\text{and }n_i=\sqrt{\varepsilon(\omega_i)}\qquad(2.10)$$

Here d_{eff} describes the nonlinear optical properties of the medium as scalar parameter which, however, cannot always be done (see later in this chapter). Instead of the complex field amplitudes the measurable intensity can be written:

$$I(z)=\tfrac{1}{2}\varepsilon_0 c\cdot n\cdot\left|\bar{E}(z)\right|^2\qquad(2.11)$$

The nonlinear optical properties of the medium are included in the constant C

$$C=d_{eff}\sqrt{\frac{2\omega_1\omega_2}{\varepsilon_0 c^3 n_1 n_2 n_3}}\qquad(2.12)$$

The exact solution of the system of differential equations (2.9) can be found in the thesis by H. Krause [6]. We concentrate here on two special cases which illustrate the important nonlinear optical effects used in this thesis.

(i) Sum-frequency generation without pump depletion: Here the decrease of the fundamental frequency intensity by creation of the frequency ω_3 can be neglected:

The boundary conditions for the wave equations are:

$$I_1(z)=\text{const.}\neq 0,\qquad I_2(z)=\text{const.},\qquad I_3(0)=0\qquad(2.13)$$

7

and the solution can be simply derived

$$I_3(z) = \frac{\omega_3^2}{\omega_1 \omega_2} C^2 z^2 I_1 I_2 \frac{\sin^2\left(\frac{\Delta k \cdot z}{2}\right)}{\left(\frac{\Delta k \cdot z}{2}\right)^2} \tag{2.14}$$

This form of the solution shows the eminent importance of the phase-matching condition $\Delta k = 0$ for efficient sum-frequency generation, which will be described later in more detail.

(ii) Optical parametric amplification (OPA) with optimal phase-matching

Under phase-matching conditions the solution of eqs (2.9) for the boundary conditions

$$I_2(0) = 0 \qquad\qquad \text{and for } I_1 << I_3 \tag{2.15}$$

can be written in its analytic form

$$I_1(z) = I_1(0)\left[1 + \sinh^2\left(C \cdot z \sqrt{I_3}\right)\right] \tag{2.16}$$

and for $C \cdot z\sqrt{I_3} \rightarrow \infty$

$$I_1(z) \cong \frac{I_1(0)}{4} \exp\left(C^2 z^2 I_3\right) \tag{2.17}$$

This means, that a small input signal in a crystal with exact phase-matching conditions will be exponentially amplified by the strong pump pulse.

Until now all nonlinear optical effects could be explained with classical electrodynamics. However, optical parametric generation (OPG) demands a quantum mechanical picture, since in the classical formulation this process is not included. The classical equations (2.9) with the boundary condition

$$I_1(0) = I_2(0) = 0, \qquad\qquad I_3 = \text{const.}$$

lead to the trivial solution

$$I_1 \equiv I_2 \equiv 0$$

One basic fact has been neglected in the classical description, namely that the vacuum includes photon fluctuations of energy kT (T: temperature). The interaction with a strong pump pulse ω_3 can induce a photon splitting into two photons of energies ω_1 and ω_2, which are under certain conditions amplified as described above [7]. This phenomenon is called "parametric fluorescence" and is in relation with the amplification process a relatively new technique to create broad band tunable laser radiation. The created high frequency photon is called "signal" the lower energy photon "idler". The technique of frequency tuning will be described in 2.2.1.

In the above description the macroscopic parameter d_{eff} contains the physical properties of the material and of the photons. In the solution of the amplitude equations the susceptibility was reduced to a single parameter. In the general description in equation 2.6 it has the mathematical properties of a three rank tensor. In the case of the above Fourier description some of it's fundamental physical properties can be extracted in the case of a quadratic susceptibility solely by symmetry considerations.

(i) Kleinman symmetry

$$\bar{P}(\omega_3) = \bar{\chi}^{(2)}(-\omega_3; \omega_1, \omega_2) \vdots \bar{E}(\omega_1)\bar{E}(\omega_2) \tag{2.19}$$

Assuming that we are regarding only frequencies ω_1, ω_2 and ω_3 in the transparent region of the nonlinear material, dispersion effects of $\chi^{(2)}_{\mu\alpha\beta}$ are excluded and all permutations of μ, α and β reproduce the same matrix. This constellation is called "Kleinman symmetry" and has been used as a tool to distinguish between ionic and electronic contributions as dominant process in nonlinear optics in crystals. Its immediate application can be found in the reduction of the primarily 27 elements of the tensor to 10 independent elements. This is further discussed in 2.7.

(ii) Permutation symmetry

A consequence of the overall permutation symmetry is the Manley-Rowe power relation, which describes the exchange of power between electromagnetic wave in a purely reactive nonlinear medium. It's mathematical derivation can be found in Butcher and Cotter [3] and just the physical content will be cited here. For a sum frequency generation process $\omega_1 + \omega_2 \rightarrow \omega_3$ it evolves

$$\frac{W_1}{\omega_1} = \frac{W_2}{\omega_2} = -\frac{W_3}{\omega_3} \qquad \Rightarrow -W_3 = W_1 + W_2 \tag{2.20}$$

i.e. the power W_3 generated at ω_3 is equal in magnitude to the total power lost by the fields at ω_1 and ω_2. The quantum mechanical interpretation is that the number of photons created at the sum frequency ω_3 is equal to the number of photons annihilated at each of the two source frequencies ω_1 and ω_2. That means, that in nonlinear processes, the total **number** of photons is **not** conserved. Historically nonlinear optical processes for which Manley-Rowe is valid are called "parametric" processes.

2.2 Nonlinear optics in crystals

For the understanding of the in chapter 3.3 described tunable laser source it is essential to understand the physics of nonlinear optical processes in crystals. A short description will be given for the special case of second harmonic generation in crystals.

2.2.1 Phase-matching and frequency tuning in nonlinear optical material

In the case of second-harmonic generation (SHG), two of the three fields in equation 2.9 are of the same frequency. We thus may put $\omega_1 = \omega_2 = \omega$, in which case the first equation is the complex conjugate of the second and we need to consider only one of them. We take the input field at ω to correspond to E_1 and the second harmonic field to E_3, and we put $\omega_3 = \omega_1 + \omega_2 = 2\omega$, neglecting absorption. So the field equation becomes

$$\frac{dE^{(2\omega)}(z)}{dz} = -\omega\sqrt{\frac{\mu}{\varepsilon}}d_{eff}\left[E^{(\omega)}(z)\right]^2 e^{i(\Delta k)z} \tag{2.21}$$

where: $\quad \Delta k := k_3 - 2k_1 = k^{(2\omega)} - 2k^{(\omega)} \tag{2.22}$

Under neglected depletion of the wave at frequency ω $E^{(\omega)}(z)$ can be set independent of z and $E^{(2\omega)}(0) = 0$. The integration over the whole length l of the nonlinear medium gives:

$$E^{(2\omega)}(l) = -i\omega\sqrt{\frac{\mu}{\varepsilon}}d_{eff}\left[E^{(\omega)}\right]^2 \frac{e^{i(\Delta k)l} - 1}{i\Delta k} \tag{2.23}$$

and following Yariv [29] the output intensity becomes proportional to

$$E^{(2\omega)}(l) \cdot E^{(2\omega)*}(l) = \left(\frac{\mu}{\varepsilon_0}\right)\frac{\omega^2 d^2}{n^2}d_{eff}\left[E^{(\omega)}\right]^4 l^2 \frac{\sin^2\left(\Delta kl/2\right)}{\left(\Delta kl/2\right)^2} \tag{2.24}$$

According to this equation, most effective SHG can be expected if the condition $\Delta k = 0$ holds. If $\Delta k \neq 0$, the second-harmonic power generated at some plane, say z_1, having propagated to some other plane z_2, is not in phase with the second harmonic wave generated at z_2. This results in the interference term of eq. (2.24). Two adjacent peaks of this spatial interference pattern are separated by the so-called "coherence length", which is a measure of the maximum crystal length that is useful in producing the maximum second-harmonic power. Under ordinary circumstances it may be no larger than 10^{-2} cm. This is because the index of refraction $n(\omega)$ normally increases with ω thus Δk is given by

$$\Delta k = k(2\omega) - 2k(\omega) = \frac{2\omega}{c}\left[n(2\omega) - n(\omega)\right] \tag{2.25}$$

If we take typical values of ω and $n(2\omega) - n(\omega) \cong 10^{-2}$ for KDP [8], we get coherence lengths

10

of about 50 μm.

The technique that is used widely to satisfy the phase-matching requirement takes advantage of the natural birefringence of anisotropic crystals. The different velocities of wave propagation for different crystal directions can be used to match the refractive indices of the fundamental wave and the second harmonic frequency 2ω according to the above relation. So the nonlinear process can be extended over the total crystal length. A detailed description of the propagation of electromagnetic waves in an uniaxial crystal can be found in Yariv et al.[9]. A wave, which is traveling with a field vector component along the optical axis of the crystal is called "extraordinary wave" and a wave traveling with its field vector perpendicular to the axis is called "ordinary".

It is impossible to satisfy the phase-matching condition $\Delta k = 0$ when both waves are of the same type - that is, when both are extraordinary or ordinary. We can, however, under certain circumstances, satisfy $\Delta k = 0$ by making the two waves be of a different type. The index of refraction of the extraordinary wave in a uniaxial crystal with the angle θ between the propagation direction and the crystal optical axis is given by

$$\frac{1}{n_e^2(\Theta)} = \frac{\cos^2\Theta}{n_o^2} + \frac{\sin^2\Theta}{n_e^2} \tag{2.26}$$

The phase-matching condition $\Delta k = 0$ can be solved for frequencies ω and 2ω, using the respective phase velocities for these frequencies from the Sellmeier equation [10]. The result, the phase-matching angle θ , fixes the optical configuration for efficient second-harmonic generation. Two types of phase matching are possible in this case. "Type I phase-matching", in which an ordinary fundamental wave creates an extraordinary second harmonic wave. Combinations like e + o -> o resulting in ordinary second harmonic waves are called "type II phase-matching".

The problem of phase-matching in parametric amplification is fundamentally the same as that in second-harmonic generation. Instead of satisfying the condition $\Delta k = 0$, we have, according to (2.10), to satisfy the condition

$$\vec{k}_3 = \vec{k}_1 + \vec{k}_2 \tag{2.27}$$

which corresponds in physical terms to the conservation of photon momentum in the crystal. By using the dependence of the phase-velocity of the extraordinary wave in axial crystals on the direction of propagation defined frequencies can be selected. In a negative uniaxial crystal ($n_e < n_o$), we can, as an example, choose the signal and idler waves as ordinary while the pump at ω_3 is applied as an extraordinary wave. Using (2.26) and the relation $k(\omega) = \frac{\omega}{c} n(\omega)$, the phase-matching condition (2.27) is satisfied when all three waves propagate at an angle Θ_m to the

optic axis where

$$n_e^{\omega_3}(\Theta_m) = \left[\left(\frac{\cos\Theta_m}{n_o^{\omega_3}}\right)^2 + \left(\frac{\sin\Theta_m}{n_e^{\omega_3}}\right)^2\right]^{-\frac{1}{2}} \qquad (2.28)$$

In a crystal the indices of refraction generally depend, as shown before, on the frequency, the crystal orientation and temperature. If, as an example, we change the crystal orientation the frequencies ω_1 and ω_2 will change so as to compensate for the change in indices, and thus condition (2.28) will be satisfied for a new set of frequencies. The same can be done by using the temperature dependence of the indices as has been demonstrated first by J. A. Giordmaine and R. C. Miller [11]. Both methods can be used. When using one parameter for frequency tuning reproducibility requires that the second parameter is well stabilized.

2.2.2 Influence of crystal symmetry on nonlinear response

We now consider in more detail the permutation symmetry properties of the second-order susceptibility tensors and will describe a useful contracted notation for these tensors. As we have seen in 2.1 the induced nonlinear polarization can be written in terms of a third rank tensor which is defined by

$$\vec{P}^{(2)}(\omega_3) = \vec{\chi}^{(2)}(-\omega_3;\omega_1,\omega_2):\vec{E}(\omega_1)\vec{E}(\omega_2) \qquad (2.29)$$

or in Cartesian coordinates:

$$P_i^{(2)}(\omega_3) = \sum_{j,k} \vec{\chi}_{ijk}^{(2)}(-\omega_3;\omega_1,\omega_2)E_j(\omega_1)E_k(\omega_2) \qquad (2.30)$$

The intrinsic permutation symmetry of the tensor $\vec{\chi}_{ijk}^{(2)}(-\omega_3;\omega_1,\omega_2)$ allows the pairs of indices (j,ω_1), (k,ω_2) to be freely interchanged. In the special case of second-harmonic generation $(\omega_1 = \omega_2 = \omega)$, the susceptibility is invariant to the permutation of j and k. So the third rank tensor can be represented in contracted form as a 3x6 matrix $d_{im}(-2\omega;\omega,\omega)$ defined as

$$P_i^{(2)}(2\omega) = \sum_m d_{im}(-2\omega;\omega,\omega)E_j(\omega)E_k(\omega) \qquad (2.31)$$

where m = 1, 2.. 6 is defined corresponding table 2.2.

m	1	2	3	4	5	6
jk	xx	yy	zz	yz	zx	xy

Table 2.2: Definition indices of the nonlinear susceptibility tensor in the contracted form d_{im}.

So equation (2.31) becomes in matrix form with Cartesian coordinates

$$\begin{bmatrix} P_x^{(2)}(2\omega) \\ P_y^{(2)}(2\omega) \\ P_z^{(2)}(2\omega) \end{bmatrix} = \begin{bmatrix} d_{11} d_{12} d_{13} d_{14} d_{15} d_{16} \\ d_{21} d_{22} d_{23} d_{24} d_{25} d_{26} \\ d_{31} d_{32} d_{33} d_{34} d_{35} d_{36} \end{bmatrix} \cdot \begin{bmatrix} E_x^2(\omega) \\ E_y^2(\omega) \\ E_z^2(\omega) \\ 2 \cdot E_y(\omega) E_z(\omega) \\ 2 \cdot E_x(\omega) E_z(\omega) \\ 2 \cdot E_x(\omega) E_y(\omega) \end{bmatrix} \tag{2.32}$$

According to the spatial symmetry of the special crystal class the number of independent element can be further reduced.

If Kleinman symmetry holds, the d-coefficient notation for the second-harmonic generation may be extended to other second-order processes following [3]. The matrix will than be written as:

$$P_i^{(2)}(\omega_3) = \sum_{j,k} d_{im}(-\omega_3; \omega_1, \omega_2) E_j(\omega_1) E_k(\omega_2) \tag{2.33}$$

$$\begin{bmatrix} P_x^{(2)}(\omega_3) \\ P_y^{(2)}(\omega_3) \\ P_z^{(2)}(\omega_3) \end{bmatrix} = \begin{bmatrix} d_{11} d_{12} d_{13} d_{14} d_{15} d_{16} \\ d_{16} d_{22} d_{23} d_{24} d_{14} d_{12} \\ d_{15} d_{24} d_{33} d_{23} d_{13} d_{14} \end{bmatrix} \cdot \begin{bmatrix} E_x(\omega_1) E_x(\omega_2) \\ E_y(\omega_1) E_y(\omega_2) \\ E_z(\omega_1) E_z(\omega_2) \\ E_y(\omega_1) E_z(\omega_2) + E_y(\omega_2) E_z(\omega_1) \\ E_x(\omega_1) E_z(\omega_2) + E_x(\omega_2) E_z(\omega_1) \\ E_x(\omega_1) E_y(\omega_2) + E_x(\omega_2) E_y(\omega_1) \end{bmatrix} \tag{2.34}$$

Since all frequencies fall into the transparency region of the crystal the frequency arguments have been omitted for d_{im}.

Finally choosing polarizations $\bar{e}_i$ for E_j the equations can be transformed into a simple scalar form

$$P^{(2)} = d_{eff} E_1 E_2 \tag{2.35}$$

Here d_{eff}, the effective d-coefficient, is a scalar parameter defined by:

$$d_{eff} := \sum_{\mu jk} d_{\mu m} (e_3^*)_\mu (e_1)_j (e_2)_k = \tfrac{1}{2} \chi^{(2)}(-\omega_3; \omega_1, \omega_2) \tag{2.36}$$

Efficiencies of different nonlinear crystal configuration can be compared with this parameter which is listed for common nonlinear crystals by Dmitriev et al.[10]

2.3 Nonlinear optics as surface tool

The development of nonlinear optics as surface tool until the beginning of this decade is summarized in a review by R. B. Hall [12]. The theory of second-harmonic generation has been reviewed in some detail by Y. R. Shen et al. [13] and with special emphasis on surface physics by G. L. Richmond et al. [14]. Although the microscopic sources are still under basic investigation especially from the theoretical point of view, careful experiments are already done to extract surface specific information like adsorption kinetics [15] and surface diffusion [16] at the solid-liquid and solid-high pressure gas interface, where other techniques have no access. The results of theses studies agree well with the results from standard techniques, in cases where both are applicable, like UHV conditions. Most experimental features can be explained by theories developed first by Bloembergen et al. [17] using the macroscopic Maxwell equations in which bulk and surface effects can be regarded independently. The inherent surface sensitivity of nonlinear optical techniques and especially SHG is based on the different electronic environment of atoms near the surface, so that the nonlinear susceptibility of a medium can be split in two parts

$$\bar{P}(2\omega) = \bar{\chi}_s^{(2)} : \bar{E}(\omega)\bar{E}(\omega) \cdot \delta(z) + \bar{\chi}_b^{(2)} : \bar{E}(\omega)\bar{E}(\omega) \tag{2.37}$$

where the first term denotes the surface contribution and the second the bulk contribution [18]

To separate these two contributions is generally a difficult task. However, many crystal structures fall into a spatial class which include symmetry properties that exclude a bulk contribution as well as disordered materials like liquids and gases. In this case all bulk
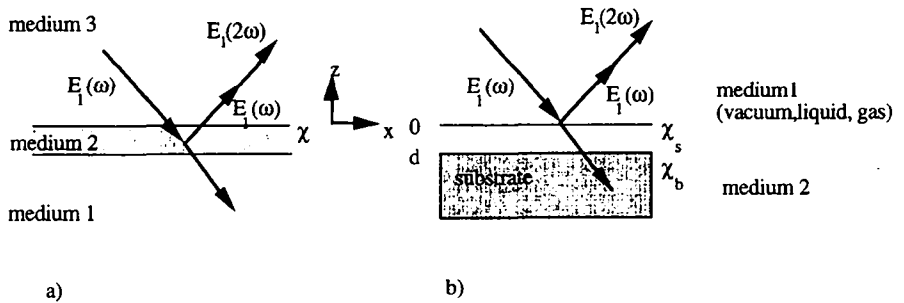
Fig. 2.3: Models of second-harmonic generation at surfaces (see text).

contributions disappear in the electric dipole approximation (higher multipole terms are for example connected with electric quadruple or magnetic dipole contributions) and only at the interface (or surface) where the crystal symmetry is necessarily broken nonlinear optical polarization must be created.

Two models are used to solve the Maxwell equations in the reflection geometry sketched in figure 2.3. Either a three layer configuration is considered, in which a nonlinear active material is embedded between two linear optical media (figure 2.3a) [17] or a thin polarization sheet is used to model the nonlinear surface properties (figure 2.3b) [13]. Both approaches yield in the case of infinitely thin nonlinear media the same result for the reflected nonlinear signal:

$$I(2\omega) = \frac{32\pi^3\omega^2 \sec^2(\Theta_{2\omega})}{c^3\varepsilon_1(\omega)\sqrt{\varepsilon_1(2\omega)}} \left| \bar{e}(2\omega) \cdot \bar{\chi}_{s,eff}^{(2)} : \bar{e}(\omega)\bar{e}(\omega) \right|^2 \cdot I^2(\omega) \tag{2.38}$$

In this equation, $\Theta_{2\omega}$ represents the angle between the propagation direction of the radiated SH light and the surface normal, $I(\omega)$ is the intensity at fundamental photon energy, and $\bar{e}(2\omega)$ is the unit polarization vector, in Cartesian coordinates, at the second-harmonic frequency. The vectors $\bar{e}(\omega)$ and $\bar{e}(2\omega)$ are related to the unit polarization vectors in medium 2 by Fresnel coefficients. The effective nonlinear susceptibility, $\bar{\chi}_{s,eff}^{(2)}$, is the sum of the surface nonlinear susceptibility, $\bar{\chi}_s^{(2)}$, and the bulk magnetic dipole (or electric quadrupole) contributions to the non-linearity. Symmetry dictates the number of independent non-zero tensor elements in $\bar{\chi}_{s,eff}^{(2)}$, that can be used to extract information about the crystalline structure of the surface as has been demonstrated successfully for the reconstructions of the Si(111) (1×1)↔(7×7) in UHV [19], Ag(111) [20] and Au(111) $(1 \times 1) \leftrightarrow (\sqrt{3} \times 23)$ [21] surfaces in electrochemical environments. Other systems have also been studied by SHG using the information from the symmetry of the nonlinear susceptibility tensor. The basic approach to study these properties is the measurement of the rotational anisotropy, i.e. the change of SHG intensity with azimuthal angle of the sample surface. By employing different polarization combinations and different scattering geometries all tensor elements of the susceptibility can theoretically be separated in symmetry and strength assuming only surface contributions from electric dipoles. As mentioned above, the rotation of the sample around its surface normal (i.e. change of azimuthal angle) corresponds to the rotational transformation of [7, 22]:

$$\bar{\chi}_{ijk}^{(2)}(\psi) = \sum \left(S_{ir}S_{js}S_{kt}\bar{\chi}_{rst}^{(2)} \right) \tag{2.39}$$

where $S = (S_{mn})$ is the rotation matrix around the z-axis. A detailed calculation for different surface symmetries can be found in [21]. Here the results for a (111) surface of a fcc crystal with C_{3v} symmetry (one threefold rotational axis and one mirror axis) are summarized for the different polarization combinations of the fundamental and the second-harmonic wavelength.

$$I_{pp}^{(2\omega)}(\psi) \propto \left|\chi_{31} + \chi_{33} + \chi_{15} + \chi_{11} \cdot \cos(3\psi)\right|^2 \tag{2.40}$$

$$I_{ps}^{(2\omega)}(\psi) \propto \left|\chi_{11} \cdot \sin(3\psi)\right|^2 \tag{2.41}$$

$$I_{ss}^{(2\omega)}(\psi) \propto \left|-\chi_{11} \cdot \sin(3\psi)\right|^2 \tag{2.42}$$

$$I_{sp}^{(2\omega)}(\psi) \propto \left|\chi_{31} - \chi_{11} \cdot \cos(3\psi)\right|^2 \tag{2.43}$$

where I_{ij} stands for i-polarisation of the incoming fundamental wavelength and j-polarization of the detected second-harmonic wavelength. Reconstructions as described before cause a change in symmetry from C_{3v} to C_s for example in the case of the Au(111) reconstruction that can be detected by measuring the rotational anisotropies of the second-harmonic intensity. For a perfect (100) surface C_{4v} is expected. 4-fold and higher symmetries however cannot be distinguished in the simple surface susceptibility model from isotropic parts of the effective surface nonlinear polarization as was experimentally also found in a picosecond SHG experiment [23]. Tom et al. found for the Si(100) surface nevertheless in nanosecond SHG experiments anisotropic components, which were assigned to magnetic dipole or electric quadrupole bulk contributions [24]. The influence of bulk effects in this case is still under discussion and several aspects have been introduced since then like nonlinear dispersion [25], strain at the interface [26], a thin crystalline SiO_2 interlayer [27] and micro roughness [28].

3. Experimental set up

3.1 Laser system

For nonlinear optical experiments high power densities of the order of GW/cm^2 are necessary, which can only be obtained by high power laser radiation. In this study a pulsed Nd:YAG laser with 20 Hz repetition rate (Continuum PY 61C-20) forms the primary light source. By active-passive mode locking one short pulse of 20 - 40 ps - depending on the saturable absorber used for passive mode-locking (Q-switch 1 or Q-switch 5, supplier: "Exciton") - at an energy of 1.17 eV (λ=1064 nm) is generated. The resulting pulse of $\approx$3.5 mJ is subsequently amplified in a second Nd:YAG rod to output powers of 70 mJ. Through efficient conversion in two KDP crystals the fundamental frequency can be doubled cf. tripled to 2.33 eV (532 nm) and 3.5 eV (355 nm), respectively. However, the frequency conversion process worsens significantly the spatial beam profile of the laser radiation due to inevitable inhomogeneities in the optical crystals. Birefringence effects of the Nd:YAG crystal may play a role, too.

This can lead to difficulties for the following nonlinear optical processes, since they are operated very close to the damage threshold of the material and inhomogeneities in the spatial pulse profile (hot spots) can irreversibly harm the optical elements. In the case of the later described optical parametric conversion process inhomogeneities can create additional difficulties to adjust the perfect beam overlap in the nonlinear crystals. Another important point is the duration of the pulses since the creation of the maximum power output increases with the square of the power density of the pulses. Here solid state lasers like the Nd:YAG in connection with nonlinear optical crystal technology have substantial advantages.

Pulse lengths of the order of picoseconds can not be measured directly by a slow photo multiplier. One method uses the second-harmonic, or more precisely, degenerate sum frequency generation process at a surface according to eq. (2.37) to obtain the spatial autocorrelation function of the optical intensity profile, from which the width of the pulse can be obtained. The measurement of a pulse of a duration of $\tau_0 = 10^{-12}$ s is thus replaced by measuring a path difference between two pulses of the order of $c\tau_0$=0.3 mm. The original pulse at frequency ω is divided by a beam splitter into two pulses of equal intensity. One of these pulses is advanced (or delayed) by τ relative to the other by traveling a different distance. The two pulses intersect again in a nonlinear optical crystal or on a surface to generate a second harmonic (2ω) pulse. The total optical SHG field is the product of the direct and retarded fields:

$$\bar{E}^{2\omega}(t) \propto \chi^{(2)} : \left[\bar{E}^{\omega}(t)\bar{E}^{\omega}(t-\tau) \right] \tag{3.1}$$

The output current of the optical detector is then incident on a "slow" detector whose output current is integrated over a time long compared to the optical pulse duration [29]

17

$$i_d(\tau) \propto \langle I(t)I(t-\tau)\rangle \tag{3.2}$$

where the brackets mark averaging over time t.

Assuming a well behaved Gaussian pulse

$$I(t) = I_0 \exp\left\{-\frac{t^2}{2\sigma^2}\right\} \tag{3.3}$$

its FWHM t_0 is correlated to its width $\tau_0 = 2\sigma$ by

$$t_0 = \tau_0 \cdot \sqrt{2\ln 2} \tag{3.4}$$

The basic set-up of an autocorrelator is schematically shown in figure 3.1. In the case of a nonlinear crystal phase-matching conditions have to be taken into consideration to maximize signal intensities. Here, the length of the crystal can play also a role when going to very short pulses. An easier set-up uses a metal surface in reflection, where the two pulses overlap spatially on the surfaces. This geometry is easier to align, but gives in general lower second-harmonic signals.
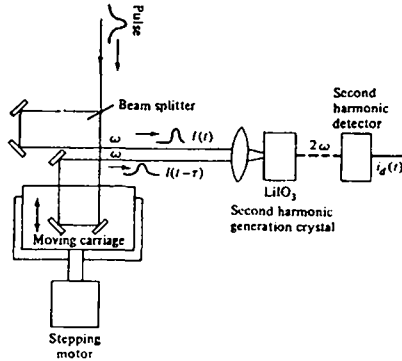

Fig. 3.1: Scheme of an autocorrelation set-up taken after Yariv [29]. In this thesis KDP crystals and metal surfaces have been used for the generation of second-harmonic radiation.

Figure 3.2a and b show the results of autocorrelation measurements for different saturable absorbers as a passive mode locker of the Nd:YAG laser system. In the case of absorber "Q-switch number 1" a pulsewidth of 31 ps was measured for the incident 532 nm pulse. This pulsewidth can be regarded as limit for the time resolution for the later described experiments (see chapter 7, 8 and 9). Using "Q-switch number 5" achieves shorter pulses of 20 ps, but resulted in lower output powers of the laser. When using the 532 nm pulses to pump a dye

laser, tunable laser pulses in the visible range can be produced. The autocorrelation curve for pulses at 590 nm are shown in figure 3.2c. The triangle form of the autocorrelation trace indicates a near rectangular temporal shape of the dye laser pulses.
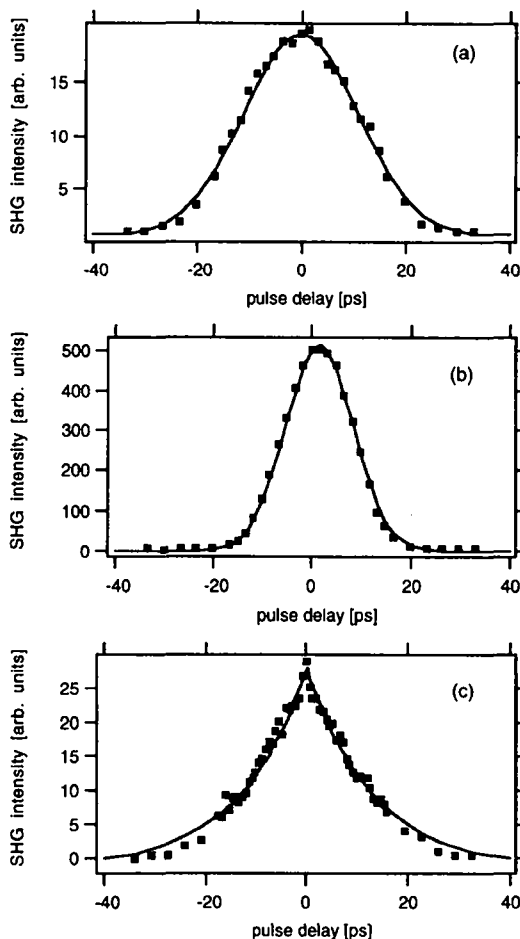

Fig. 3.2: Autocorrelation trace for 532 nm pulses of the Nd:YAG system in (a) and (b) and for a dye laser pulse of 590 nm (c) measured by second-harmonic generation from a polycrystalline gold surface. (a) and (b) fit well with a Gaussian of $\tau_0=31$ ps and 20 ps. In (a) Q-switch 1 and in (b) Q-switch 5 were used for passive mode-locking.

3.2 Detector- and data acquisition system

The above described experiment can be set up in the most economic way by using only filters to separate the second harmonic from the fundamental wavelength. To assure high flexibility of the detection system, which is necessary for wavelength dependent experiments as described later, a double monochromator (Jobin Yvon HD 10D 1200 grooves/mm) is used to obtain a low stray light level, since ambient light suppression is necessary to measure low photon intensities in the second-harmonic signal. The frequency resolution is limited by the monochromator. Photons are measured by a photo multiplier tube, directly attached to the monochromator, whose slit combination is chosen to give around 2 nm resolution, which is shown in figure 3.3 for the fourth harmonic of the Nd:YAG fundamental wavelength.
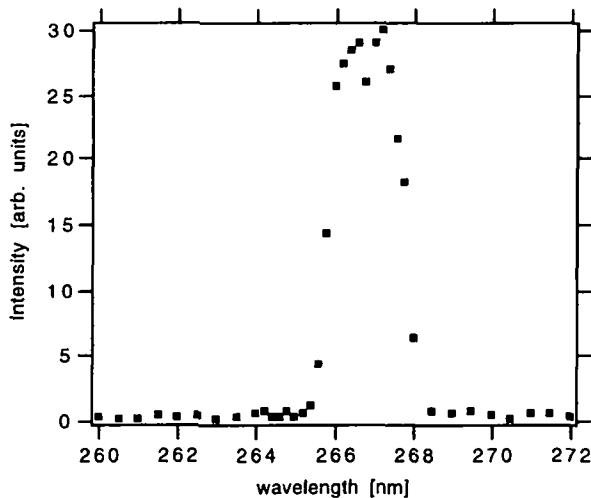

Fig. 3.3: Measured intensity of the fourth-harmonic signal of the Nd:YAG laser versus monochromator wavelength. The step width was 0.5 nm and the monochromator resolution was set to 2 nm reflecting the spectral distribution of the measurement.

For light detection two different photo multiplier tubes (PMT) (Hamamatsu R4220 and R928) are used. Photo multiplier R928 has the advantage of a broader frequency range, but lower amplification. A very important point is the linearity range of the photo multiplier, which is normally assured by the manufacturer for low photon densities per time interval. The incoming photons emit electrons from the cathode of the PMT. These charges are amplified and measured by an A/D converter. In the case of high charge densities, as happens for short intense laser pulses, the relation between analog signal and the number of incoming photons becomes non-linear. For this reason the voltage divider for the dynodes was changed to provide a linear

characteristic up to about 30 pC per pulse corresponding approximately to 15 photons per pulse.

The analog charge signal of the PMT is converted by a CAMAC ADC to a 10 bit value which can be read out via an IEEE data bus system controlled by a HP workstation. To suppress the influence of photons which are not created due to the laser pulses, PMT signals are only collected in a 100 ns time window around the instant when a laser pulse leaves the Nd:YAG cavity. The CAMAC is triggered by a signal from a photo diode, that was mounted near the cavity and monitors the build-up of each laser pulse. In the following the calibration of the ADC counts in photons incident per pulse is discussed. Figure 3.4 shows the distribution of counts obtained for a large number of measurements at a fixed photon fluence. The sharp peak corresponds to the dark signal (offset) of the ADC, which represents the measurements in which no photon arrives. The peak (or shoulder) to the right of this offset corresponds to the distribution of charges provided by the PMT in the case where one or more photons were measured during one laser shot. The integrated charge is summed over each measurement (i.e. laser shot) as single photons cannot be resolved in time (ps!). Reducing the photon flux until the probability that 2 photons enter the PMT during one measurement becomes negligible a certain charge distribution is obtained. The center of gravity of this distribution is ascribed to the mean charge (or count rate) corresponding to one single photon. By increasing the supply voltage of the multiplier this value can be increased. All SHG experiments were done at maximum allowed PMT supply voltage of 1200 V where one photon corresponds to around 8 counts.

Beside reading out the CAMAC data the computer controls all electromechanical elements like stepping motors.
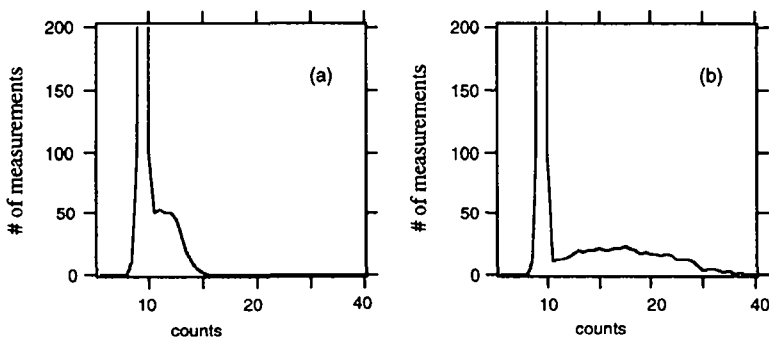

Fig. 3.4: Characterization of the photon sampling technique. Integrated charge distributions supplied by the PMT for one laser shot are integrated over several measuring cycles. (a) shows the distribution for a PMT voltage of 1050 V, (b) for 1200 V. The separation between the "zero" photon and the "one" photon peak (shoulder in (a)) increases.

3.3 The tunable pulse source

For high efficiency of nonlinear processes the power density has to be as high as possible. So short pulses are preferable to generate nonlinear optical processes. By use of parametric optical oscillators strong ns pulsed light sources can be built and are already commercially available. In the case of single pulses this concept is not applicable since pulse trains are required to drive a nonlinear optical oscillator. However, strong light sources for single pulses can be built with optical parametric generation and subsequent amplification. For a tunable laser source in the visible /NIR range from 0.5 - 3 eV (2500 - 410 nm) photons of energies around 3.5e V are necessary to be converted by nonlinear generation according to chapter 2.1 into two different photons of lower energy. The fundamental wavelength of 1064 nm (1.17 eV) can be tripled to 355 nm (3.50 eV) and will be used as pump pulse for the nonlinear conversion process with signal frequencies in the range of 1.7 - 3 eV and idler frequencies of 0.5 - 1.7 eV. Energy tuning is achieved by rotating the nonlinear crystals.

The laser system built in this thesis follows the basic concept by Krause and Daum [30, 31] and uses LiB_3O_5 (LBO) nonlinear crystals for the design of an angle tuned OPG/OPA system. The system is sketched in figure 3.5. The 355 nm pump beam enters the first LBO crystal generating parametric super fluorescence in a broad band divergent beam. A standard dielectric 355 nm mirror and a color filter separate the undepleted pump beam from the parametrically generated components which are used for seeding the subsequent parametric amplification in the second LBO crystal. Either the visible signal or the infrared idler component is spectrally narrowed by a diffraction grating (Gitter) in Littrow geometry. The reflected light is focused by an achromatic lens (Achromat) on an adjustable slit (Spalt) and is recollimated by a concave mirror (Konkavspiegel). A dove prism (Dove-Prisma) reverses the beam. The pump beam merges with the seed beam after traveling an adjustable delay line (Verzögerung). In the second LBO crystal the seed beam is parametrically amplified. The residual pump pulse is separated from signal and idler by a standard 355 nm mirror and a color filter. The wavelength control is obtained by tuning the angles of the LBO crystals.

Temperature tuning has already been successfully used for LBO crystals, but the angle tuning wavelength control has advantages in flexibility since the rotation of the crystal can easier and faster be controlled than the temperature. Like KDP and most nonlinear crystals LBO is slightly hygroscopic. For this reason gentle heating of the crystal is necessary to prevent the adsorption of water and the crystal from rapid degrading. Due to the heating the crystal parameters of LBO in the Sellmeier equations are changed from the room temperature values [6]. The crystal temperature needs to be stabilized to 1°C which is enough for correct angle tuning as can be seen from figure 3.6 were the phase matching angle change at 526 nm with temperature is shown. An angular correction of 0.008 °/K can be determined from this curve. A summary of the properties of LBO and a comparison with other nonlinear optical crystals can be found in
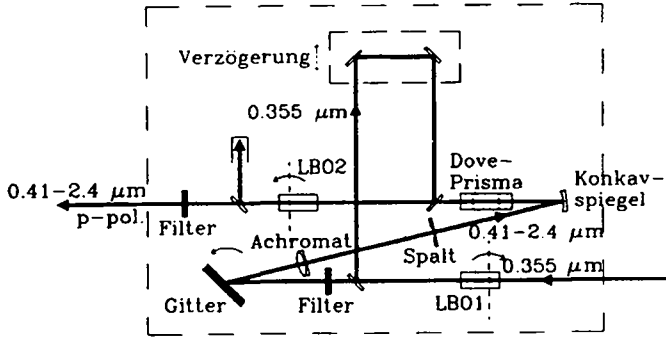
Verzögerung

0.355 μm

0.41-2.4 μm
p-pol.

Filter

LBO2

Achromat

Dove-Prisma

Kohkav-spiegel

0.41-2.4 μm

Spalt

0.355 μm

Gitter   Filter   LBO1

Fig. 3.5: Schematic diagram of the LBO parametric generator and amplifier. LBO1, LBO2: first and second LiB$_3$O$_5$ crystal; Filter: color filter; Gitter: grating; Achromat: achromatic lens; Spalt: adjustable slit; Konkavspiegel: concave mirror; Dove-Prisma: dove prism; Verzögerung: delay for 355 nm pump beam (from [6]8).

the handbook of Dmitriev et al. [10].

Most important for the maximum efficiency of the OPG/OPA system is the beam profile of the pump wavelength at 355 nm. A Gaussian profile of the TEM$_{00}$ mode is most favorable. Krause et al. used a 12 m beam path for the 1064 nm beam from the laser to select this mode before generating the pump pulses by frequency tripling. In the set-up described in this thesis it is the 355 nm beam which is spatially filtered before entering the first LBO crystal (fig. 3.5.). L1, SP and L2 form the spatial filter and the lenses are used as a telescope to adopt the pump beam energy density. Slight smoothening of the spatial profile is obtained if 10 - 15 % of the intensity is cut-off by a 100 μm pinhole. Sapphire pin holes (SP) of diameters between 200 and 20μm have been manufactured in the LOA (Laboratoire d'Optic Appliquée) of the EPFL by laser drilling. No vacuum assembly was necessary for the pinhole design, since no electric discharge due to the field breakthrough in the focal area was observed. If too much intensity is cut off by the pinhole, intensity fluctuations (spikes) occur due to ablation of particles ejected into the focal area of the laser beam inside the pinhole.
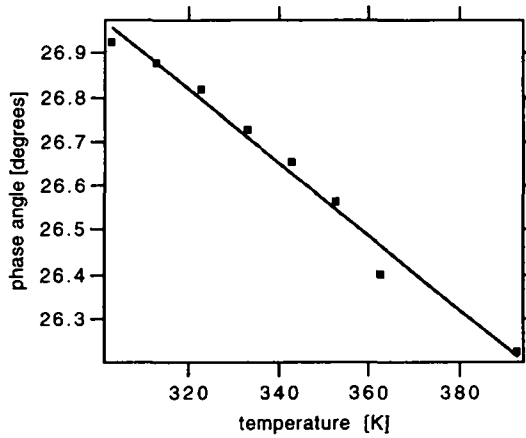
Fig. 3.6: Change of phase-matching angle (around 526 nm) with temperature for one LBO crystal. The crystal normally operates at 323 K.

Another difference to the collinear design by Daum et al. is the right angle geometry of the beam paths between the two nonlinear crystals. They allow precise alignment of the delay between pump pulses and generated signal and idler pulses from the first LBO crystal, that are directed by dielectric (DM) and broad band metallic mirrors (MM) into the second LBO crystal, where they are amplified by the pump pulse. The two pulses have to be very well overlapped. Since the dielectric mirrors (DM) transmit of the order of 0.1% of the pump radiation the residual intensities sketched as dashed lines exit at DM 6 can be overlapped on the fluorescence screen (FS) in figure 3.7. This set-up acts as a classical interferometer for the residual intensity with the two branches DM 4 - DM 5 - DM 6 and DM 4 - MM - DM 6. Temporal overlap and parallel beam alignment can be checked by inspecting the interference pattern, that is only observable in case of alignment of signal and idler with the pump pulse in the second LBO crystal. The pump pulse is taken out of beam behind the second LBO crystal by a dielectric mirror and a color filter (NBF). The idler or signal can be selected by a long pass filter (LPF: LCRG-695, supplier: Laser Components) or a band pass filter, respectively.

As pointed out in chapter 2 changing the angle of the LBO crystals results in the change of the phase matching conditions for the generated wavelengths of the OPG/OPA system. Thus by tuning the LBO crystals the output photon energy can be selected as shown in equation (2.28). Fig. 3.8 shows the relation between crystal rotation and signal frequency for the LBO

OPG/OPA system. The rotation angle α is directly related to the internal phase-matching angle φ through

$$\sin(\phi - \phi_{cut}) = \frac{\sin\alpha}{n(\lambda = 355nm)} \qquad (3.5)$$

where ϕ_{cut} is the cut angle of the crystal, which is in the present case 24.5°. The measured values can be well fitted by a parabolic function that is included in the figure. To adjust directly the frequency of the OPG/OPA these parameters are evaluated and then used for the recalculation of the rotation angle of the specific frequency values. The use of two crystals has the advantage that beam displacements created by the rotation of the nonlinear crystals can be compensated by tuning the crystals in the same directions while conserving the phase matching conditions.

Output energies of the order of 200µJ have been obtained from this set-up. Increasing the power density of the pump pulses close to the damage threshold of the LBO crystals and further optimization of the optical set-up will be necessary to reach higher values. The relative energy output of the system over a wide frequency range is shown in figure 3.9.
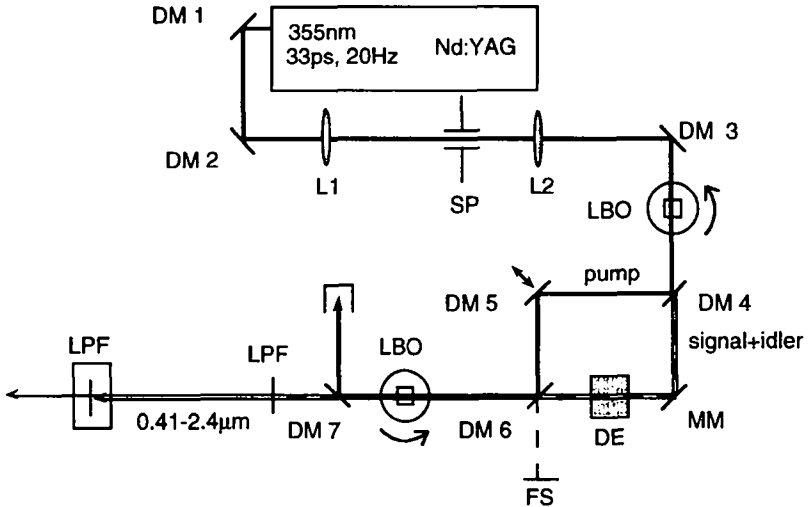

Fig. 3.7: Schematic diagram of the modified OPG/OPA. LBO: crystals on rotation stages; DM: 355 nm dielectric mirrors; MM: metallic mirrors; L: lenses; SP: sapphire pin hole; FS: fluorescence screen; LPF: long pass filter; DE: dispersive element.
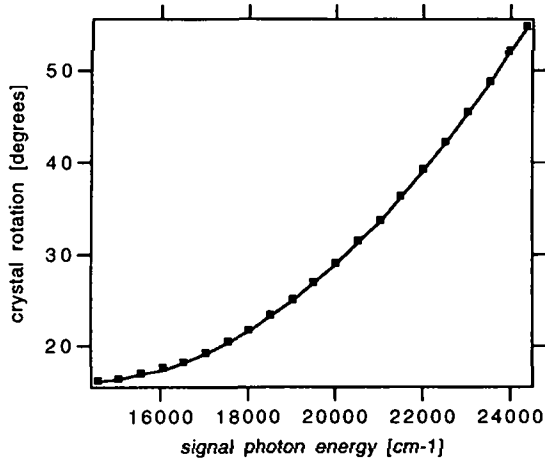
Fig. 3.8: Angle tuning curve for the OPG/OPA with LBO crystals. The point are measured values that fit a parabolic function implemented in the software which rotates the crystals for a given photon energy.
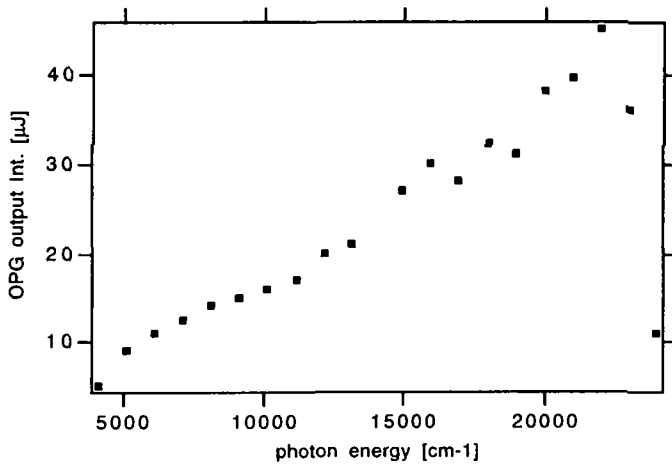

Fig. 3.9: Measured OPG/OPA spectral energy distribution. The beam energy falls off to lower photon energies.

For the effective use as tunable pulse source for spectroscopic applications the bandwidth of the radiation plays an important role. Figure 3.10 shows the bandwidth of the OPG/OPA as function of the photon energy for the signal frequency. The bandwidth rises drastically near the degeneracy frequency, where two photons of the same energy are created. The bandwidth is determined by the divergence of the pump beam [7]. The behavior can roughly be described with a quadratic inverse function as shown in figure 3.10.

To reduce this bandwidth an additional dispersive element (DE) has to be introduced after the first LBO crystal as indicated in the set-up in figure 3.7. Daum et al. used a grating in Littrow geometry to reduce the bandwidth to less than 5 cm^{-1}[31] at degeneracy. Another form of dispersive element is a Fabry-Perot interferometer which provides almost constant resolution and good transmission over a wide range. Such an element is not commercially available but has been designed for this system to reduce the bandwidth of the OPG/OPA.
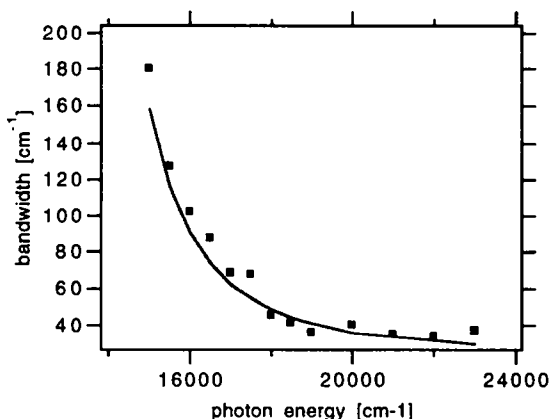

Fig. 3.10: Bandwidth of the OPG/OPA measured with the double monochromator with 0.1 nm resolution. The sharp rise due to the degeneracy at 14085 cm^{-1} can be roughly approximated by a fit to a quadratic inverse function.

In this chapter the set-up of the laser system used for the following nonlinear optical experiments has been presented. Different to most second-harmonic generation experiments in the past done at fixed frequencies it offers the possibility of continuous variable frequency experiments in the visible to near infrared range. Bandwidth and power output can still be improved and the introduction of a second conversion stage with nonlinear optical crystals like AgGaS$_2$ and CdSe it is possible to extend the variable range into the middle- to far-infrared [6, 20].

27

The in the preceding chapters described elements are now combined for second-harmonic generation experiments, in which the nonlinear response can be studied as function of different experimental parameters, like azimuthal angle, preparation, etc. Most experiments are undertaken either in transmission for a fixed polar angle as indicated in the inset of figure 3.11 for a thin film on a solid substrate. One special case is the measurement of the second-harmonic response of the sample when brought into electronic excited states by photons of different energies. In this case two beam pathways are necessary: one for the exciting pump photons, the other for the second-harmonic generating probe photons. Both overlap spatially and temporally at the sample.

Figure 3.11 shows the optical set-up for a typical pump-and SHG probe experiment, which will be described in more detail in chapter 6.3. The 355 nm radiation of the tripled Nd:YAG fundamental frequency or the tunable output of the OPG/OPA system described in chapter 3.3 are taken as pump pulses. For probing the sample, the fundamental photons of the Nd:YAG system are separated and delayed relative to the pump photons. This delay can be adjusted to vary the delay times from some picoseconds to ≈ 1 ns at maximum. The 1064 nm radiation is then slightly focused onto the sample, which is placed in a high vacuum chamber. The SH photons are generated at the sample, collected by a second lens and directed into the detection system. The intensity of the SH signal can then be measured as function of delay times as demonstrated in chapter 6. By minor changes in the set-up the same experiments can be pursued in reflection geometry.
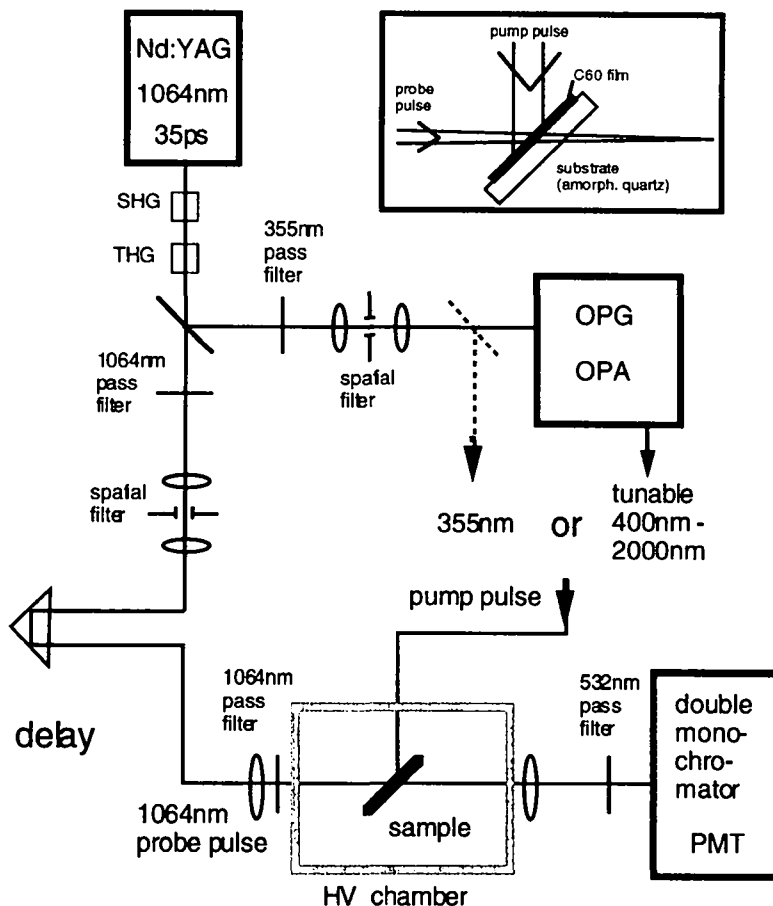
Fig. 3.11: Optical set-up for SHG and pump-and SHG probe experiments. The UV wavelength of the Nd:YAG laser system is used either directly as pumping pulse or is injected into the OPG/OPA set-up of figure 3.7 to create tunable laser pump pulses. The 1064 nm radiation is delayed relative to the pump pulses and used as probe for the generation of second-harmonic generation at the sample. Additional spatial filtering stages are included in all beam lines to insure homogeneous beam profiles. The set-up is shown for transmission experiments as indicated in the inset for films on solid substrates in a vacuum chamber. With minor changes in the set-up measurements in reflection geometry are possible.

4. Second-Harmonic Generation at the Si-SiO₂ Interface

One of the first systems to which nonlinear optics has been applied as surface and interface sensitive tool are silicon surfaces and interfaces. Particularly the Si(111) surface, a surface that can be easily prepared by wet chemistry [32] has served for extensive studies of SHG and SFG [33, 34]. The Si(111) surface is predominantly of academic interest, while the Si(100) surface is of more importance for technological applications. The growing of well defined oxides as the first manufacturing step in the device production of storage devices is still a subject of current research since it strongly influences the quality of the Si/SiO₂ interface [35] and its electrical performance. Secondary fabrication processes are in general applied to modify the interface in order to improve its structural and electrical properties [36]. A comprehensive summary of the physics and chemistry of the Si-SiO₂ interface can be found in C. R. Helms et al. [37]. Most of the production steps are done at high temperatures under high pressure conditions where classical surface science techniques do not permit in-situ studies. Optical techniques like SHG, however, have the potential to do this and have already proven to be a versatile tool for the diagnostics of semiconductor surfaces and interfaces [38].

Second-harmonic generation has already proven to be successful in the identification of interface states at the Si-SiO₂ interface [26] and will be used in the following to characterize different preparations of the oxide growth on Si(111) and the effect of interface modifications for this typical semiconductor-insulator interface. We will see that SHG can serve as a tool to study the etching process of the oxide in-situ in fluorinated etchants.

4.1 Experimental

The silicon oxide is grown on n-Si(111) (Siltronix, P-doped, 3 - 5 Ωcm) in a typical low pressure thermal oxidation setup [39] under clean room conditions. Before every growth process a standard cleaning procedure has been applied which consists of dilute (5%) HF rinsing for some seconds, sulfuric acid bath for ca. 20 minutes and final rinsing in deionised water (>18 MΩcm). The oxide is grown in different growing procedures resulting in 150 nm dry oxide, in pure oxygen vapor at 1100°C for 80 min. (preparation A), or 150 nm humid oxide, grown in water steam at 1100°C for 11 min. (preparation B). The water steam was created by the reaction of hydrogen and oxygen in stoichiometric ratio in the growth chamber. Both procedures yield an amorphous oxide layer.

A second preparational procedure has been the post-annealing process of 50 nm dry oxide at 450°C. The samples were either annealed in pure nitrogen vapor (preparation C) or in a mixture of nitrogen and hydrogen (preparation D). Wet oxide interfaces exhibit also a high degree of atomic roughness. Interfaces grown under dry conditions exhibit less roughness and less

interface defects [40]. Nevertheless additional post oxidation annealing procedures are used to modify the interface. Hydrogen is known to easily diffuse to the interface [41] where it causes the Fermi level to move from a pinned position to its bulk position [42].

Etching of 150 nm wet oxide were performed in aqueous ammoniumfluorid solution (40%) which is known to etch the Si(111) surface only at very low etching rates, which results in a flattening of the Si(111) surface [33]. The etching was performed in a Teflon cell which has been closed with a fused quartz window. After etching away all the silicon oxide the surface should stay hydrogen terminated.

For the SHG measurements at the Si(111)-SiO$_2$ interface the doubled frequency of the Nd:YAG laser at 2.34 eV (532 nm) was used. The pulsed radiation had an incident angle of 50° with the beam being focused to a spot size of ca. 2 mm^2. The fluence was kept below 200 µJ at least one order of magnitude below the appearance of any damage which occurs above 100 mJ cm^{-2} [43]. The geometry of the experimental set-up is similar to that described in chapter 3 (see figure 3.11). No pump pulses are used, however, and instead of the fundamental frequency at 1064 nm, the 532 nm radiation is selected for the probe beam path. The necessary optical filters were used. The output of the laser is polarized. The second-harmonic frequency at 4.68 eV (266 nm) has been measured as a function of the azimuthal angle for different polarization combinations.

4.2 Second-Harmonic Generation at the solid-solid interface

Figure 4.1 (left hand side) shows the azimuthal dependence of the second-harmonic intensity for p-s and s-s polarization combination of the SiO$_2$-Si interface prepared under dry (H free) growing conditions (prep. A). The first index denotes the polarization of the fundamental and the second of the second-harmonic frequency. Figure 4.1 (right hand side) shows the equivalent measurement for wet growing conditions (prep. B). Fitting curves of the measurements with the following empirical formular for the phenomenological interface nonlinear response

$$I^{SHG}(\psi) \propto \left| a + e^{i\phi} \cdot \cos(3\psi) \right|^2 \tag{4.1}$$

are represented as solid lines in the figures with isotropic and anisotropic components and a phase factor ϕ. The tensor elements of the nonlinear susceptibility are in general complex numbers and since isotropic and anisotropic are summed coherently their phases have to be taken into account. Only the relative values of amplitude and phase, a and ϕ, can be determined in this way.
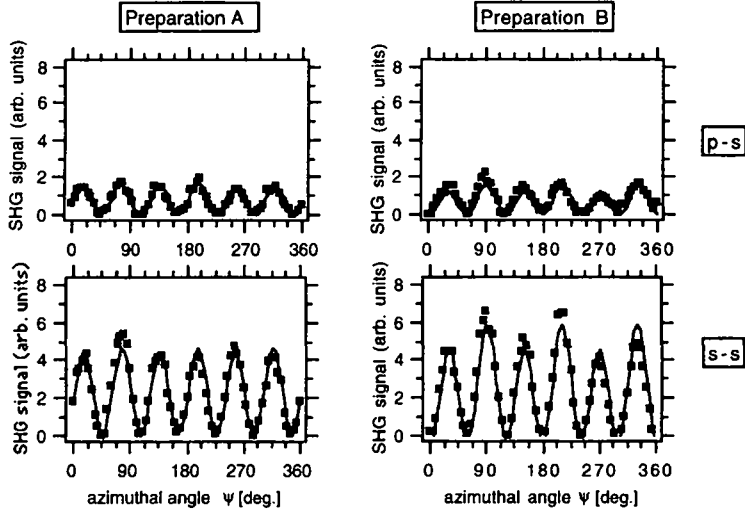
Fig. 4.1: Azimuthal dependence of the second-harmonic signal for different polarization combinations, that are compared to different preparational procedures A and B (see text). The solid lines are fits according to eq. (4.1). The fit parameters are compared in table 4.1.

(s-s):	Prep.	A:	a	= 0.14,	ϕ	= 291°	(±10°)
	Prep.	B:	a	= 0.07,	ϕ	= 341°	(±10°)
(p-s)	Prep.	A:	a	= 0.17,	ϕ	= 308°	(±10°)
	Prep.	B:	a	= 0.31,	ϕ	= 306°	(±10°)

Table 4.1: Fit parameters according to eq. (4.1) of the azimuthal angle dependence of the SHG signal shown in figure 4.1. A relative phase shift between isotropic and anisotropic component appears for preparation B.

The rotational spectra show only minor differences at first sight. However, a relative phase shift between the isotropic and anisotropic component in case of preparation B can be observed. It is known that temperature treatments strongly influence the structural properties at the interface due to stress creation. This effect on the nonlinear optical properties has already been observed and discussed by Daum et al. [26] for the Si(111) and the Si(100) interfaces. Since the wet-oxidation process is much faster than the dry process, the interface stays much shorter under the influence of high temperatures, for the same oxide thickness.

In a second experiment dry grown oxide-silicon interfaces have been subjected to a secondary

processing step in which they were annealed in a nitrogen (prep. C) and a nitrogen/hydrogen mixture (prep. D). Figure 4.2 shows the azimuthal SH intensities for the same polarization combinations as before. The fitted curves have been obtained following the same procedure as for figures 4.1. No change in the relative intensities between the two components could be found. But again a rotation of the relative shift appears in the s-s component. The parameters are listed in table 4.2. They cannot be directly compared to table 4.1 since differences can be expected between the two interfaces due to thermal relaxation of stress at the interface. However, relative changes, as in the rotation of the relative phase, can be attributed in both cases to the influence of hydrogen.
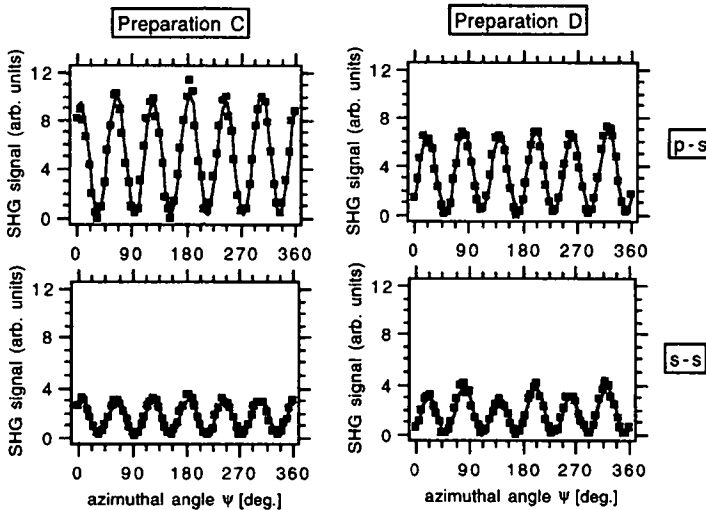

Fig. 4.2: Azimuthal dependence of SHG as in figure 4.1.

(s-s)	Prep.	C:	a	=	0.09,	ϕ	=	271°	(±10°)
	Prep.	D:	a	=	0.09,	ϕ	=	315°	(±10°)
(p-s)	Prep.	C:	a	=	0.07,	ϕ	=	286°	(±10°)
	Prep.	D:	a	=	0.10,	ϕ	=	291°	(±10°)

Table 4.2: Fit parameters according to eq. (4.1) of the azimuthal angle dependence of the SHG signal shown in figure 4.2. A relative phase shift between isotropic and anisotropic component appears for preparation B.

An isotropic component in p-s and s-s polarization combination cannot be explained in the phenomenological theory of the simple interface model (see formulae 2.40 - 2.43). It has been found by J. L. Daschbach et al. [44] that for a hydrogen terminated Si(111) surface a phase change appears in p-p polarization, which they related to the band bending at the silicon surface. In the same manner the effect of hydrogen might explain these experimental results of the phase change when hydrogen is applied during growth or post annealing processes.

4. 3 Oxide etching

In-situ etching experiments were undertaken which could follow the signal intensity with decreasing a-SiO$_2$ thickness. At the beginning of the measurement the sample containing cell was filled with water, which was after alignment exchanged with the etching solution. The intensity was measured during the etching over 170 min. and the signal stayed constant until the etching front approached the silicon surface. The last ten minutes of the etching process, which is started with the exchange of the solution, is shown in figure 4.3.
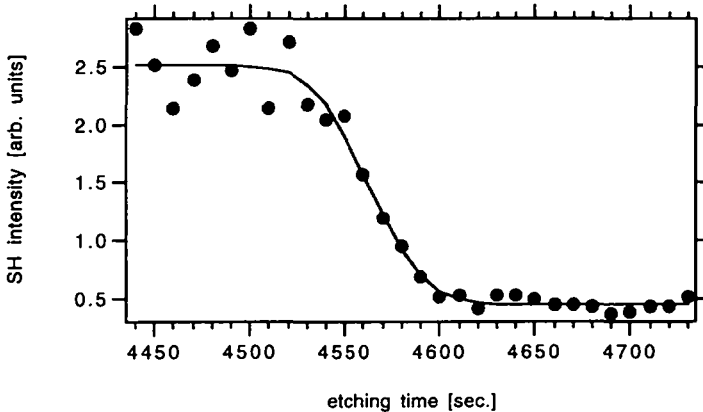

Fig. 4.3: Second-harmonic intensity in the last stage of the etching process in 40 % NH$_4$F(aq.). A rapid decrease of the signal from 90 to 10 % of the total intensity is observed in 60 seconds. The signal stays constant afterwards.

The decrease of second-harmonic intensity from 90 % to 10 % takes place within 60 sec. For a total thickness of 150 nm an etching rate of ca. 0.03 nm s^{-1} was determined. Assuming a constant etching rate also in the late stages the drop in intensity corresponds to 2 nm indicating a

small roughness. This experiment shows that the source of the nonlinear response is located at the interface. The decrease has already been observed at a photon energy of 1.17 eV for the fundamental beam. [45]. No linear optical effects were found to contribute at this wavelength. Kulyuk et al. considered different effects responsible for the explanation of the rapid decrease. Inhomogeneous deformation was found not to exceed 10 %. A thin oxide transition layer with high susceptibility was proposed to be responsible for the large second-harmonic signal at the Si-SiO$_2$ interface. The overlaying quartz layer is known to be amorphous, so that the inversion symmetry does not allow a second-harmonic signal in the dipole approximation. However, a crystalline phase in the quartz layer might give a small second-harmonic signal which could explain the additional isotropic term. The interpretation of the microscopic source of the nonlinear response of the SiO$_2$-Si interface has been subject of numerous studies and is often discussed controversially in the literature. Stress induced effects, a crystalline interlayer at the interface, interface roughness, quadrupolar bulk response and band bending due to surface charge carriers are considered important factors [26, 46-52]. The later effect induces an additional contribution from the third order polarizability at the interface. This ordered oxide layer may also be responsible for the isotropic component seen in the azimuthal measurements. The rapid decrease only in the last stage when the last parts of the oxide is etched away excludes the existence of large crystallites at the interface.

5. C$_{60}$ preparational methods and preliminary experiments

After the discovery of the arc-discharge preparation methods most experiments of the solid phase of C$_{60}$ have been performed on films, which have been evaporated onto solid substrates. The structure of these films depends on the substrate and the deposition parameters. Numerous studies have been performed on the growth of C$_{60}$. A full review by Weaver et al. [53] summarizes the results until 1994. In general there is a large difference between films grown on metal surfaces and insulator surfaces, which indicates a large metal-C$_{60}$ interaction, which is due to charge transfer from the metal to the adsorbed molecule [54]. On semiconductor surfaces the important factor seems to be the low corrugation of the substrate that allows nearly epitaxial growth [55]. At reactive surfaces like the (7x7) reconstructed Si(111) surface the growth is influenced due to the strong bonding of C$_{60}$ with the dangling bonds of the Si surface. On insulator surfaces (fused quartz, Al$_2$O$_3$, NaCl, MgF$_2$, etc.) most C$_{60}$ films are polycrystalline with domain sizes ranging from several nanometers to micrometers [56]. Only mica allows nearly epitaxial growth with lateral crystal domains of several hundred micrometers due to the periodic structure of the SiO$_4$ tetraheders [57]. The following table 5.1 gives a classification of bonding of C$_{60}$ to solid substrates with its desorption temperature.

bonding	substrate	desorption temperature [K]
van-der-Waals	graphite, GeS, mica, a-SiO$_2$, Al$_2$O$_3$, NaCl, MgF$_2$	≈ 500
ionic (charge transfer)	Au, Ag, Cu	$\approx 700 - 850$
covalent	Ge	≥ 1000
	Ni, Pt, Al, Si(111) 7x7	no desorption before dissociation

Table 5.1: Desorption temperatures of C$_{60}$ for different substrates after Weaver and references therein [53].

5.1 Single crystal growth

Crystalline order on a macroscopic scale and impurities like embedded atoms and molecules in the crystal structure can have important influences on the nonlinear properties as has been seen already in the silicon experiments (see chapter 4).

For this reason high purity single crystals of C_{60} will be used for experiments. They have been grown by H. Berger (IPA) using the temperature gradient growth technique [58]. The starting material was commercial C_{60} powder (Hoechst AG, 96% purity), which has been purified further by several sublimation cycles. Most impurities are C_{70} molecules or organic contaminants left over from the HPLC (High-performance liquid chromatography) purification process. By outgassing the powder at 200° C in vacuum (10^{-3} mbar) organic contaminants are removed. The vapor pressure of C_{70} is lower than the vapor pressure of C_{60} in the temperature range from 400 to 600°C so that in a C_{60} sublimation process around 400°C the percentage of C_{70} molecules is largely reduced.

TEM (Transmission Electron Microscope) images of large single crystals show the natural surfaces being (111) and (100) faces (fig. 5.1). The single crystal grows predominantly into these two directions, which is in agreement with the thin film studies in which most growth modes show a polycrystalline mixture of (111) and (100) grains. Very large crystals of up to 10 x 10 mm^2 and about 3 mm thick have been grown.
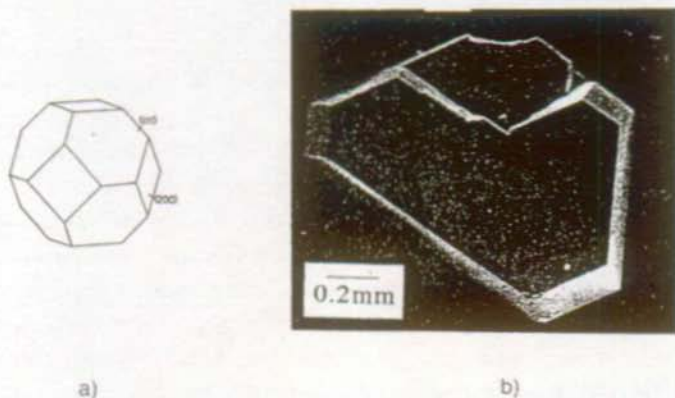

a)   b)

Fig. 5.1: (a) Theoretical equilibrium crystal. From [59]. (b) SEM picture of a well developed C_{60} crystal grown by a vapor transport technique, from [58].

5. 2. Thin film growth and characterization

The thin film preparation by evaporation on solid substrates has been used for the first characterizations of fullerenes in the solid phase [60, 61]. In the preparation care has to be taken to prevent the incorporation of impurities during the deposition process and the diffusion of impurities into the solid afterwards. Impurities can also be created by photochemically induced processes. They will be discussed in the following paragraphs. The preparation is carried out in a vacuum chamber.
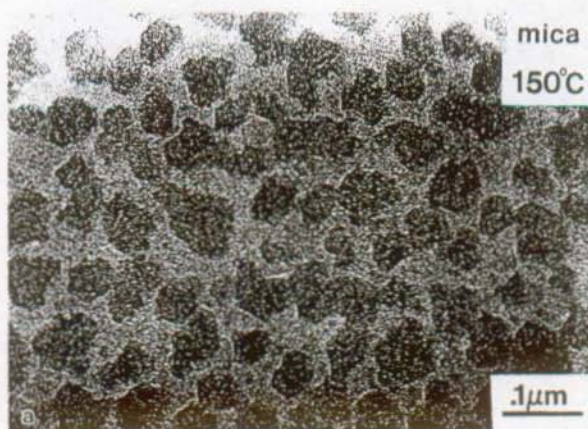
Fig. 5.2: Low magnification bright-field TEM images of C_{60} deposited on mica at 150°C. From [57].

Before deposition of C_{60} the Knudsen cell (WA Technology) with a graphite liner is preheated to 250°C close to the sublimation temperature to evaporate incorporated oxygen and any other metastable C_{60} derivatives. For the actual deposition a cell temperature of 450°C at base pressures around 10^{-6} mbar is employed. For the deposition on fused quartz the substrate temperature is held between room temperature and 140°C. On untreated silicon wafers which are covered with an oxidized overlayer growth is polycrystalline with the tendency to build larger nanocrystals at higher substrate temperatures [62]. An example of the nanocrystalline structure can be seen in a transmission electron microscopy image of C_{60} films on mica in figure 5.2. The thickness of the films is measured ex-situ by an alpha-step profile scanner to calibrate the effusion cell and was found to be roughly linear in deposition time. Small deposition rates of around 0.05Å/s are used. Other substrates showed under the same conditions different deposition rates, eg. there is almost no sticking on Teflon.
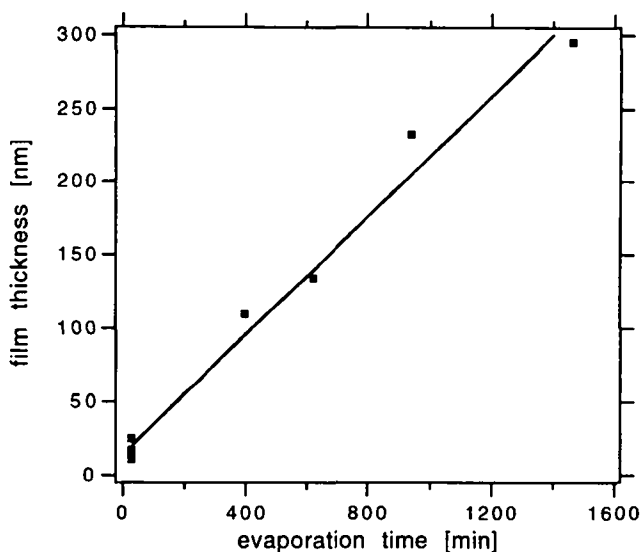
Fig. 5.3: The film thickness follows linearly the evaporation time for C_{60} deposition on quartz substrates for one given deposition geometry at constant substrate temperature (T = 140°C).

After the preparation process the films have been cooled down slowly (1 K/s). They are transferred to a separate vacuum chamber, which has a base pressure of 10^{-5}mbar. The transport through air is carried out under darkroom illumination in order to avoid irreversible chemical reactions (see 5.2.2).

5.2.1 Impurities during the deposition

One of the major impurities is always the next higher stable fullerene C_{70}. Concentrations of all other fullerenes are negligible. However, the low operating temperature of the cell and the relatively large difference between the vapor pressure of C_{60} and C_{70} [63, 64] ensure the deposition of purified C_{60} films.
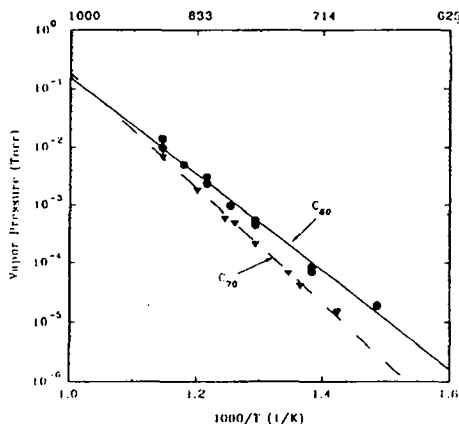
Fig 5.4: Vapor pressure of C_{60} and C_{70} Buckminsterfullerenes. From [64].

The chemical purity of the sublimated C_{60} films has been controlled by vibrational spectroscopy (IR and Raman) which does not show any impurities like C_{70} [65]or oxygen in the films. In *particular Raman spectra show only the typical modes for C_{60} (fig. 5.5)*
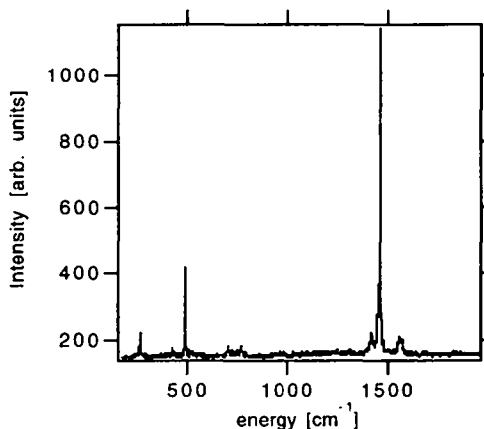

Fig. 5.5: Raman spectrum of a film grown on an amorphous quartz substrate at room temperature. The assignment of the modes is given in table 5.2. Prominent features are the $H_g(1)$ (273 cm^{-1}), the $A_g(1)$ (498 cm^{-1}) and $A_g(2)$ mode (1469 cm^{-1})

Due to its icosahedra symmetry the 174 vibrational degrees of freedom are reduced to 46 fundamental vibrational modes. Only the A_g and H_g modes are Raman and the F_{1u} modes are infrared active. The inversion symmetry of the buckyball does not permit modes being infrared and Raman active at the same time. A full description of the modes is given in Table 5.2

[66].The vibrational modes of the C_{60} solid are predominantly of molecular nature and therefore very sensitive to impurities chemically bound to the C_{60} cage. Especially the pentagonal pinch mode $A_g(2)$ at 1469 cm^{-1} has been used in the past to assign chemical reactions in C_{60} films as will be discussed in the next paragraph.

Mode	Frequency Infrared [cm^{-1}]	Frequency Raman [cm^{-1}]
$v_1(A_g)$		497.5
$v_2(A_g)$		1469
$v_1(F_{1g})$		502.0
$v_2(F_{1g})$		975.5
$v_3(F_{1g})$		1357.5
$v_1(F_{1u})$	526.5	
$v_2(F_{1u})$	575.8	
$v_3(F_{1u})$	1182.9	
$v_4(F_{1u})$	1429.2	
$v_1(H_g)$		273.0
$v_2(H_g)$		432.5
$v_3(H_g)$		711.0
$v_4(H_g)$		775.0
$v_5(H_g)$		1101.0
$v_6(H_g)$		1251.0
$v_7(H_g)$		1426.5
$v_8(H_g)$		1577.5

Table 5.2: Assignment of the vibrational modes for an isolated C_{60} molecule. First order IR- and Raman-active modes have F_{1u} and (A_g, H_g) symmetries, respectively. From [66].

5.2.2 Photo induced effects

Reaction of C_{60} with oxygen under illumination [67, 68] can well be studied by Raman spectroscopy. In the beginning of fullerene research the measurements were discussed controversially. A final conclusive picture evolved in the last two years that describes the photo polymerization processes of C_{60} and C_{70}. A full report by Eklund et. al ([69] and references therein) discusses the experimental observations in detail. The results will be summarized here

since they will be used later (see chap. 7).

UV or visible light illumination of C_{60} films and single crystals under vacuum conditions (10^{-6} mbar) change the $A_g(2)$ pentagonal pinch mode (at 1469 cm^{-1}) as can be seen in figure 5.6c. With increasing illumination time the initial mode disappears and a weaker mode at 1459 cm^{-1} appears. This change can be interpreted as a 2 + 2 cycloaddition reaction between parallel carbon double bonds on adjacent molecules as is schematically shown in figure 5.6b. A bimolecular photochemical reaction involves a C_{60} monomer in the excited triplet state and a ground state monomer. The breaking of the double bond softens the vibrational mode which leads to a decrease in frequency. The intensity is lowered due to less polarizability since the delocalized electrons are absent in the polymeric phase. In general photon fluxes of 8.3 mW mm^{-1} at 488 nm from a Ar ion laser are used to photo transform a 4500 Å C_{60} film completely during 700 min.
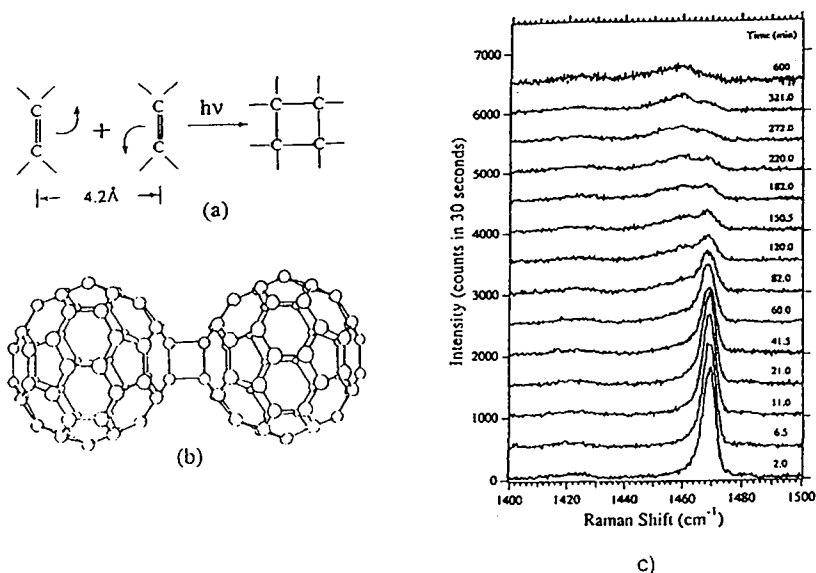

Fig. 5.6: (a) Schematic "2 + 2 cycloaddition" reaction between parallel carbon double bonds on adjacent molecules and the reaction product: C_{60} dimer (b). The time-evolution of the Raman spectra near 1469 cm^{-1} of a C_{60} film (ca. 450 nm) on a suprasil substrate. The film was encapsulated in vacuum and studied at room temperature (c). From [70].

The polymerized form can be retransformed to the fcc pristine structure by heating to around 150°C and an activation barrier of 1.25 eV was found. This energy has been identified with the thermal barrier to dissociate a monomer from a dimer or higher oligomer in photo polymerized C_{60} [69].

5.2.3 Extrinsic contamination studied by SHG

An evacuated glass chamber equipped with a fullerene evaporation cell has been installed to perform in-situ experiments of the growth process and to study in detail the influence of extrinsic contaminations like oxygen, nitrogen or argon on C_{60} films.
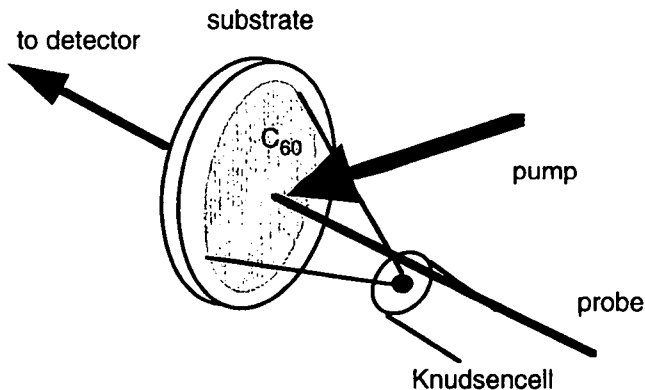

Fig. 5.7: Schematical picture of the in-situ SHG geometry in transmission. The Knudsen cell is situated under the optical plane and is directed with an angle of 45° to the substrate.

An ultrasonically cleaned tantalum effusion cell with an orifice of around 500 micrometer (see fig. 5.7) has been positioned in front of the quartz substrate with an inclination of 45° to the optical plane. The resistively heated effusion cell was filled with about 40 mg pure C_{60} powder (99.9% supplier: MER Corp.) and preheated very close to the sublimation temperature of C_{60} for at least 12 hours. After the outgassing process a white-yellowish haze could be seen on the wall facing the effusion hole, indicating contaminations of the original powder that had been evaporated. The substrate which had been positioned far away from the deposition area during the outgassing process was then moved into preparation site for transmission SHG experiments during the film growth. A second evaporation cycle showed clean C_{60} on the glass chamber. Typical laser intensities for the fundamental pulse at 1.17 eV (1064 nm) have been 200 μJ focused on an area of around 0.5 mm². A typical SHG signal following the film growth can be seen in figure 5.8. The deposition rate is 0.43 Å/s.
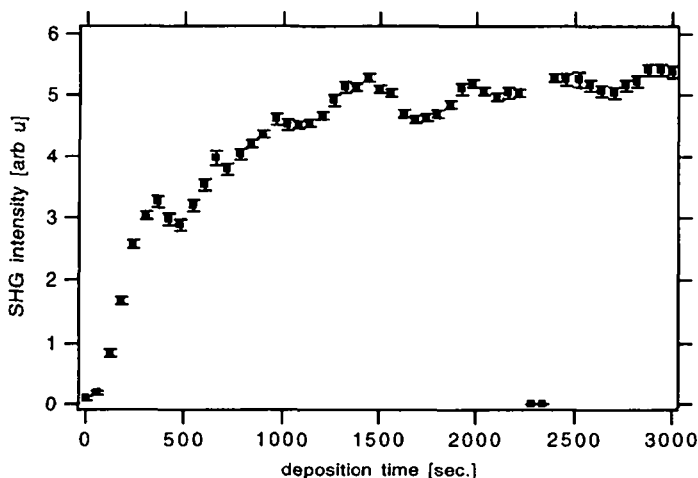
Fig. 5.8: The observed second-harmonic intensity during film growth onto an amorphous quartz substrate in transmission geometry. At 0 sec. the deposition started and was stopped after 2400 sec. The laser beam was blocked for 120 sec. to control the baseline. Periodic oscillations are probably due to oscillations in the laser intensity.

At 2400 seconds the deposition was stopped resulting in a film of ≈ 104 nm thickness. The loss in intensity at this point is due to blocking of the laser beam. Afterwards the intensity did not change indicating that the laser pulses did not harm the film. Oscillations in the intensity during deposition are probably due to oscillations in the laser intensity, since calculations of the second-harmonic signal in a three-layer-model following Bloembergen et al. [17] shows an oscillating behavior only for film thicknesses on the scale of the photon wavelength consistent with the measurements of Wilk et al. [71]. Azimuthal scans of thin films of C_{60} that were deposited on quartz at different substrate temperatures during deposition all showed rotational isotropy as shown in figure 5.9.

Figure 5.10 shows the behavior of the second-harmonic signal when the chamber is backfilled by oxygen at different pressures. The films were prepared *in-situ* and the SH signal was monitored every ten seconds averaging over about 200 laser shots. The oxygen pressure was increased in discrete steps and kept constant for periods of about 5 minutes. The second-harmonic intensity was measured simultaneously. With increasing oxygen pressure an increase of second-harmonic intensity could be measured. When pumping off the oxygen the intensity decreased. The effect was found to be fully reversible.
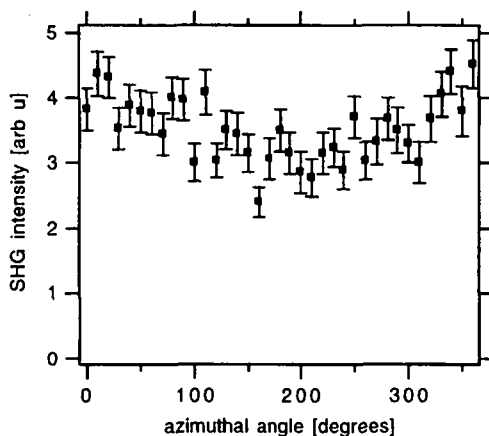
Fig. 5.9: Azimuthal scans for p-p polarization of the thin film deposited on amorphous quartz. No azimuthal anisotropy is observed indicating a polycrystalline structure of the film.
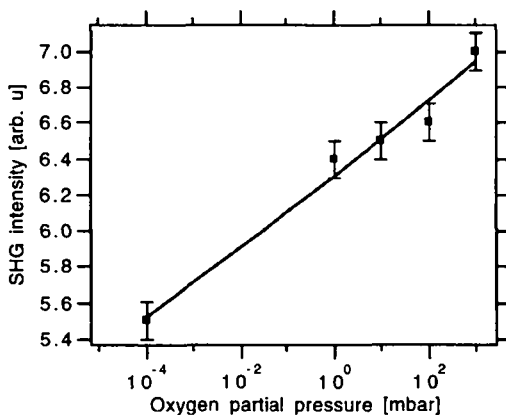

Fig. 5.10: Second-harmonic signal for different oxygen pressures and the film prepared in-situ in figure 5.8. The pressure dependence is reversible.

Several groups investigated the diffusion process of oxygen molecules into the solid pristine structure of C_{60} crystalline material [53]. Under high pressure at room temperature the intact molecule seems to occupy octahedral interstitial sites in the fcc lattice. The same experiments have been done for nitrogen and argon and the same behavior was found. It is thus very likely that the gases are intercalated into the fullerite structure causing a change in the second-harmonic intensity. A similar reversible behavior of the SHG signal has also been found when applying nitrogen and argon instead of oxygen. This and the reversibility indicate that no chemical reaction has taken place. It is therefore reasonable to believe that the preparation ex-situ and the transfer of the samples at ambient atmosphere into the analyzing chamber incorporated gas molecules in the samples, which are removed by pumping off the chamber.

6. Optical suppression of SHG at the C₆₀ single crystal

The physical and chemical properties of fullerenes, specifically of C_{60}, have been subject of intense experimental and theoretical study in recent years. In view of potential applications much interest is due to their nonlinear optical properties like nonlinear absorption [72], optical limiting [73], optically induced absorption [74, 75] and the large values of third and second order nonlinear susceptibilities [76-78]. Detailed studies were recently performed for second harmonic generation (SHG) from C_{60} thin polycrystalline films [71, 79, 80]. Not much work was yet done on nonlinear properties of C_{60} excited states and no SHG study from single crystal surfaces has been reported. From the analogy to linear conjugated organic molecules it might be expected that nonlinear optical properties can be drastically changed by optical excitation [81]. The general importance of such an effect is related to the understanding and tailoring of fast switching elements for photonics which require a weak pump beam and a quasi instantaneous and absorptionless response of an intense probe beam.

The pump-and-probe technique provides a unique tool to study the dynamics of ultra-fast phase transitions [82] and excited states in molecular and solid systems [38]. The idea of the experiment is to use a picosecond pump pulse to prepare the system in an excited state and to monitor the relaxation to the initial state by a time-delayed probe pulse. This method was already applied to pulsed-laser annealing of semiconductors [83] , to the orientational relaxation of molecules at the liquid-liquid interface [84] and the influence of photo-excited carriers on the dynamics of vibrational modes at surfaces [85].

6.1 Experimental

Nonlinear optical experiments are performed with the set-up described in chapter 3.3. The fundamental and the third harmonic from a Nd:YAG laser are used as probe and a pump pulse, respectively, in a pump-and-probe scheme. The probe beam at 1.17 eV is focused to a 1.2 mm² spot. The pump pulse (3.5 eV) illuminates a much larger area. The measurements were performed at room temperature in air and in high vacuum (10^{-5} mbar).

C_{60} is transparent at the probe wavelength. The generated SH lies in a region of small absorption above the optically forbidden band-gap. The resonance conditions are thus the same as in a recent thin film study [71]. The pump beam is close to the second absorption maximum (3.56 eV) corresponding to the molecular h_g-> t_{1u} transition [86, 87]. In the reflection and transmission measurements the angle of incidence of pump and probe beam with respect to the surface normal are 45°. The pump beam is incident at a small angle to the probe beam in the surface reflection geometry as seen in figure 6.1. In the crystal transmission measurements pump and probe beam are separated by about 90°. In both geometries difference frequency

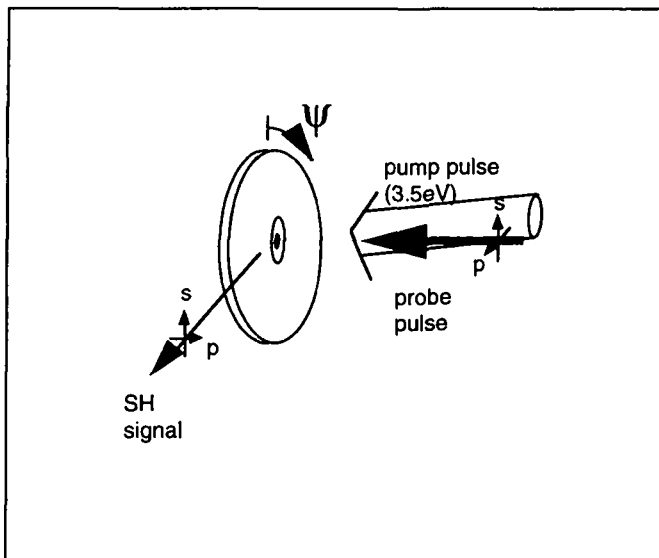generation between pump and probe beam cannot occur in the direction of the detector.

Fig. 6.1: Scheme of a pump-and-probe SHG experiment from a single crystal. The crystal can be rotated around the surface normal. The incoming fundamental and outgoing second-harmonic probe beams can be polarized as indicated. The pump pulse covers an area much larger than the probe beam.

6.2 SHG at the single crystal

Figure 6.2 shows the measured SH signal (circles) from the C_{60} crystal surface without pump beam as a function of azimuthal angle for four polarization combinations. As in the case of the silicon single crystal surface the azimuthal dependence of the signal was fitted to

$$I_{SH}(\psi) = \left[a + s \cdot \sin(3\psi + \Phi) + c \cdot \cos(3\psi + \Phi)\right]^2 \tag{6.1}$$

as deduced from equation 2.40 - 2.43. The parameters a, s, c, and Φ of the best fit (solid lines in fig. 6.2) are given in table 6.1. One of the amplitudes s or c was set to zero in order to obtain a unique solution with a constant azimuthal phase Φ in all fits. In contrast to the polycrystalline films deposited on solid substrates, which exhibit no azimuthal anisotropy (figure 5.9), the
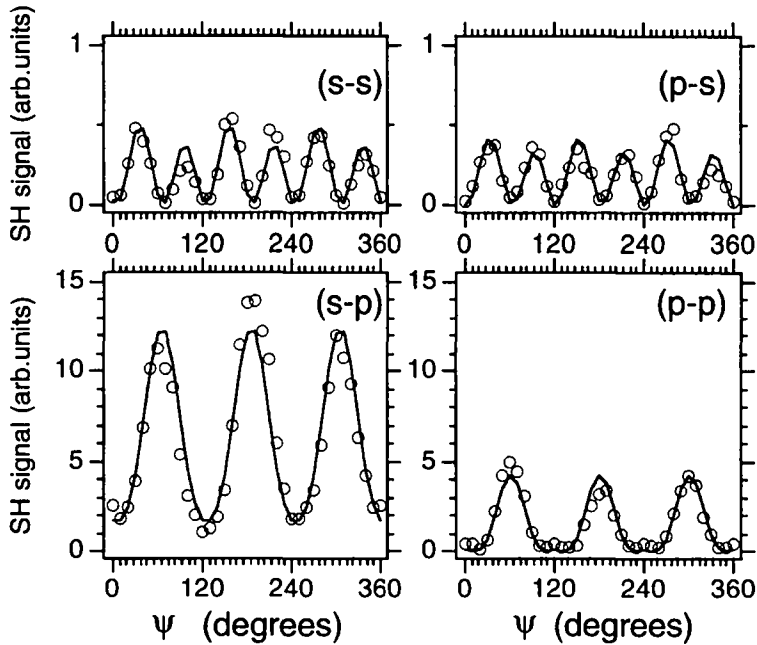

Fig. 6.2: Azimuthal scans for different polarizations of the incident fundamental and the observed second-harmonic beam. The open circles are the measured points, the lines are best fits to eq. (6.1) with the parameters given in table 6.1. In the short notation the first and second letters indicate the polarizations of the incident fundamental (1.17 eV) and the polarization of the generated second-harmonic beam (2.33 eV), respectively.

single crystal surface exhibits isotropic and threefold contributions compatible with SHG at an fcc(111) surface. Solely from these data it is not possible to separate all tensor elements. For a further separation, data from the (100) surface must be taken into consideration. However, it is also possible to decide whether a bulk source contributes to the signal by probing the information depth of our the second-harmonic signal. This is one of the ideas of the pump and probe SHG experiment which will be discussed in the following chapters.

polarization: fund. - SH	a	s	c	ϕ (degrees)
s-s	0.04	0.66	-	6
s-p	2.40	-	-1.14	6
p-s	0.04	0.61	-	3
p-p	0.90	-	-1.17	2

Table 6.1: Fit parameters of the azimuthal scans in figure 6.2. The fit function is given in eq. (6.1).

6.3 Optical switching at the single crystal surface

There is a strong debate about the source of SHG in C_{60}. The centrosymmetric structure of the molecular symmetry I_h and the fcc structure in the solid state forbid any electric dipole allowed bulk contribution and the dominant second-harmonic signal should have its origin at the surface. The small van-der-Waals interaction in the solid state makes it a classical example for a perfect semiconductor surface which does not show reconstruction effects at the surface. The high spatial symmetries of the ground state properties seduce to expect an increase of a second-harmonic signal when this system is disturbed as it was indeed reported for degenerate four wave mixing (DFWM) in C_{60} toluene solutions [88]. In fact, the contrary happens.

When the crystal surface is optically pumped at 3.5 eV the generated second-harmonic signal is substantially affected. As shown in figure 6.3a it falls off on a short time scale and stays constant. Equivalent pump-and-probe transients are found for different azimuthal angles and other polarization combinations of the fundamental, SH and pump beams. The second-harmonic signal is in all cases quenched without indication of the creation of an additional isotropic or threefold component. The monotonic decrease of the second-harmonic intensity with increasing pump fluence (see figure 6.4) over three orders of magnitudes excludes this explanation, since then one might expect that it reaches zero and increases again. The lifetime of the observed state which quenches the second harmonic signal can be estimated from figures 6.3 a, b to be longer than 20 ns. However, when the following laser pulse arrives after 50 ms the signal has completely recovered. The lifetime τ is thus 20 ns $< \tau <$ 20 ms. In transmission through a 1 mm thick crystal the observed SH signal is generated near the exit face. Signal reduction occurs when the exit face is pumped (fig. 6.3b) while it does not occur if the entrance face is pumped (fig. 6.3c). Thus no remarkable transient absorption occurs for the fundamental beam. For the SH frequency the transient absorption change [89] cannot explain the observed decrease in SH signal. The observed decrease is thus based on a true change of non-linear susceptibility. This will be further underlined with pump-and-probe experiments from thin films in which this transient absorption has been further studied.

The absorption of the pump photons and its influence on the second-harmonic signal can be modeled in a simple two state system where the excited state S* of the system is known to relax to the ground state within time constant τ. The time dependence of the population n* of the excited state can be described by the rate equation

$$\frac{dn^*}{dt} = -\frac{n^*}{\tau} + P(t) \tag{6.2}$$

where P(t) describes the intensity and the temporal shape of the pump pulse. The population n and n* are conserved corresponding

51

$$n * + n \equiv 1 \tag{6.3}$$

The second-harmonic will consist of coherently superposed contribution of the susceptibilities of the populated states according to

$$S_{SHG} \propto \left| n(t) \cdot \chi^{(2)} + n * (t) \cdot \chi^{(2)} * \right|^2 \tag{6.4}$$

The experimentally measured normalized signal has to take into consideration the temporal form of the pump pulse, in which case the convolution of the expression with a Gaussian $G(t)$ has to be considered

$$I_{norm}^{SHG}(t) = \frac{I^{SHG}(t)}{I_0^{SHG}} = \left| \sqrt{S(t-t')} \circ G(t') \right|^2 \tag{6.5}$$

In which case we get analytically

$$I_{norm}^{SHG}(t) = \left| 1 + \frac{A *}{2} e^{-\frac{t}{\tau}} \cdot e^{-\frac{\sigma^2}{2\tau^2}} \cdot \left[1 - erf\left\{ \frac{1}{\sqrt{2}} \cdot \left(\frac{\sigma}{\tau} - \frac{t}{\sigma} \right) \right\} \right] \right|^2 \tag{6.6}$$

with the error function $erf(t)$, the Gaussian pulse width of the pump pulse σ and $A*$ the effective strength of the populated state. With this formula the time dependence of the normalized second-harmonic signal can be fitted. The lifetime τ is estimated to be $\tau \geq 20$ ns Typical values for the decrease of SHG are around 35 ± 5 ps, which fits well with pump-probe correlation times of 45 ps.
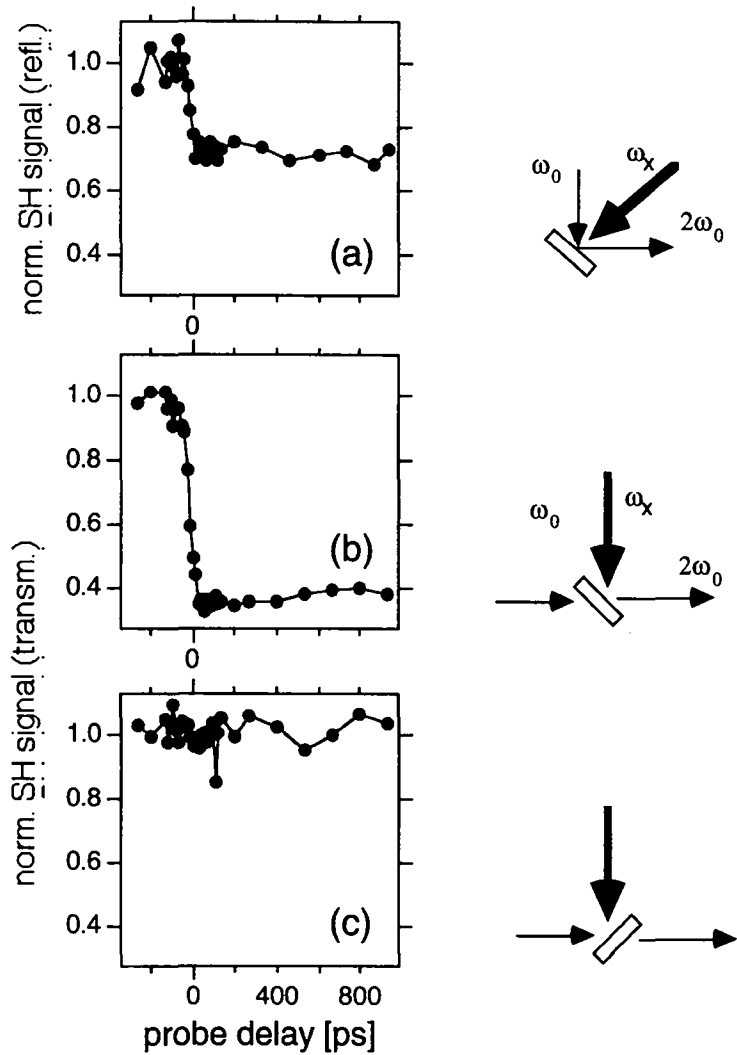
Fig. 6.3: UV pump-and-probe second-harmonic transients at an azimuthal angle of $\psi = 60°$. The second-harmonic signal is normalized to the signal without pump pulse. Second-harmonic in reflection from the crystal surface (p-p polarization): (a) single pulse, pump density 1.3 $\mu J/cm^2$. Second-harmonic signal in transmission through the crystal (containing p-p plus p-s contributions): (b) pump beam incident on the back of the crystal, pump density 6.4 $\mu J/cm^2$; (c) pump beam incident on the front of the crystal, pump density 4.6 $\mu J/cm^2$.
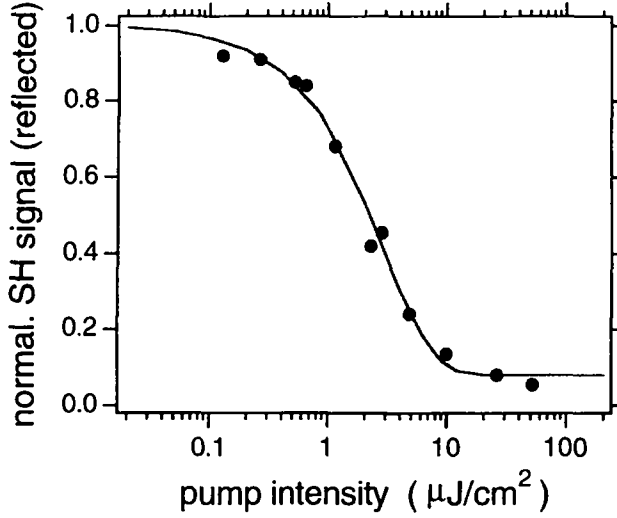
Fig. 6.4: Normalized second-harmonic signal at 330 ps probe delay as a function of pump intensity at 3.5 eV. The full circles and the line represent the measured values and the exponential fit of eq. (6.7), respectively.

To determine the efficiency of the pump photons onto the second-harmonic generation the suppression of the signal with varying pump intensity has been measured. The probe delay was fixed at 330 ps and the second-harmonic intensity was measured alternating between open and blocked pump beam. The intensity was averaged over 1000 laser shots. In each measuring interval photons arriving with blocked probe but open pump pulse were measured, too. For high pump intensities ($> 20\mu J$ cm^{-2}) a background of 532 nm photons of up to 10 % of the unsuppressed second-harmonic intensity was found with the pump beam open. It could be related to photons in the path of the 355 nm beam which were left over from the conversion process in the KDP crystals. This counting rate was subtracted from the second-harmonic intensity with open pump. The corrected values for the decrease of the SH signal at 330 ps delay with increasing pump intensity are shown in figure 6.4 in a semi-logarithmic plot. The best fit single exponential to the data is obtained as

$$I_{SH}(p) = R + (1-R) \cdot e^{(-\gamma \cdot p)} \tag{6.7}$$

where p is the pump energy density in $\mu J/cm^2$, R an unquenchable component, which is for the single crystal negligible with 0.08 and γ the efficiency parameter. The 1/e value is reached at a

pump density of $\gamma = 3$ μJ/cm^2 . A weak beam is thus sufficient to control the SHG efficiency over at least one order of magnitude.
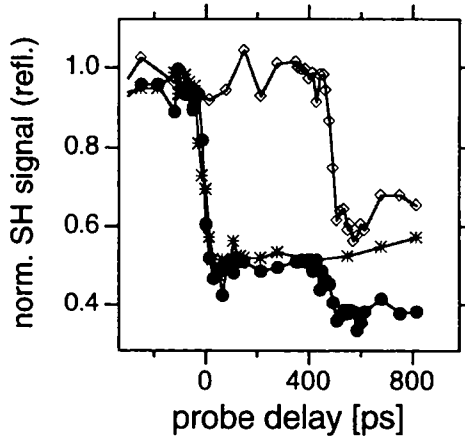

Fig. 6.5: UV pump-and-probe second-harmonic transients at an azimuthal angle of $\psi = 60°$. The second-harmonic signal is normalized to the signal without pump pulse. Second-harmonic in reflection from the crystal surface (p-p polarization): response to two separate pump pulses of approximately 1.5 μJ/cm^2 each (stars: pulse incident at t = 0 ps, diamonds: delayed pulse at t = 500 ps) and response to two successive pulses (full circles).

The effect of two successive pump pulses is demonstrated in figure 6.5. The first pulse reduces the SH signal to 54%, the second to 62%. The decrease measured after the two pulses is 37% and agrees with the product 54% x 62% = 33%. This indicates that the decrease is a function of the time integrated intensity and does not primarily depend on the pulse power.

The whole intensity of the pump radiation is absorbed in a thin surface layer which can be estimated by the inverse of the absorption coefficient α. For 355 nm photons this corresponds to around $\frac{1}{\alpha} = 30$ nm [87] . The Lambert-Beer law for the absorption describes the intensity present at a given distance x from the surface:

$$I(x) = I_0 \exp\{-\alpha x\} \tag{6.8}$$

where I_0 is the total intensity applied to the medium. Thus the absorption per unit length at the surface is

$$-\frac{dI(x)}{dx}\bigg|_{x=0} = \alpha \cdot I_0 \tag{6.9}$$

The 1/e value 3 $\mu J/cm^2$ at 3.50 eV corresponds to 5.4 10^{12} photons/pulse m^{-2} absorbed at the surface. For the (111) surface of an fcc fullerite the ratio of absorbed photons to C_{60} molecules becomes 8×10^{-4}. Even if all excitations are considered to migrate rapidly (< 45 ps) to the surface the excitation density in the top layer would still remain below 4%. The depth over which the photons are absorbed following the Lambert-Beer law can be calculated following the scheme in figure 6.6. The dashed square corresponds to the same area as the integration over the exponential absorption curve.
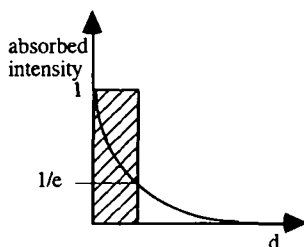

Fig. 6.6: Schematic picture of the absorption of the pump photons by a thin film in the surface region. The absorption falls off exponentially according to the Lambert-Beer law. The integrated absorption corresponding to the area under the exponential curve is equal to the dashed area.

If we suppose that the second-harmonic effect is restricted to the surface of the crystal, which is a reasonable assumption as will be discussed in chapter 7 in detail, we can calculate the quenching cross section for a molecular surface density of about 1.5 10^{14} m^{-2} for the fcc (111) surface.

The microscopic quenching cross section can be defined as follows

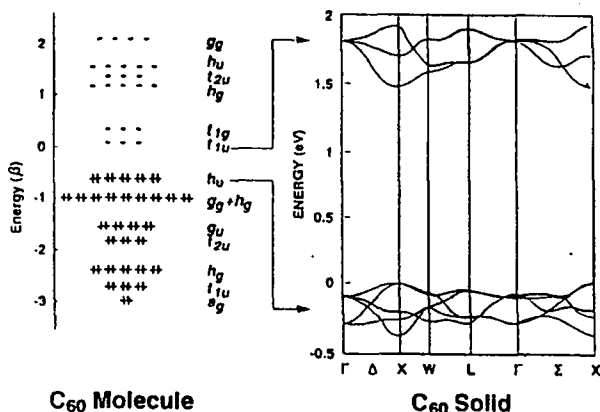$$\eta_{pump} = \hbar\omega\gamma \tag{6.10}$$

and we obtain in this case $\eta_{pump} = 19nm^2$. In view of the small fraction of excited molecules the explanation of the SH suppression by depletion of the ground state can be ruled out. Further experiments in chapter 7 will support this.

7. Origin of SHG in solid state C_{60} and the mechanism of optical switching

7.1 Optical properties and electronic states

Optical absorption of C_{60} in hexane solution fitted considerable well with Hückel calculations of the free C_{60} molecule. In addition, the optical absorption of solid C_{60} films showed a weak onset of absorption already at 1.82 eV. Saito et al. [90] calculated in a microscopic total-energy calculations the electronic states for the free C_{60} cluster which could well reproduce the molecular features and extended the calculation in a LDA approach to a fcc cluster solid and found the fullerite structure being a direct bandgap semiconductor with a bandgap of 1.5 eV. This direct transition is optically forbidden and the low absorption in this frequency region has been attributed to lifting of the dipole selection rules by the crystal field, so that the calculation were found to be in good agreement with the experiment considering the fact that LDA generally underestimates bandgap energies, but well reproducing band structures of ground states.

Fig. 7.1: Electron energy levels for C_{60} in molecular and solid state form. The energies deduced from Hückel calculations are shown at the left for the π-levels, along with their degeneracy and symmetry. The right portion shows how the degenerate h_u and t_{1u} levels broaden into the valence and conduction bands described in the Brillouin zone of the fcc structure. The electronic properties retain a high degree of molecular character. From [53].

However, PES (Photoelectron Spectroscopy) and IPES (Inverse Photoelectron Spectroscopy) found a separation of HOMO and LUMO band centers of 3.7 eV and an extrapolated band edge separation of 2.3 eV. The bandwidth was found to be very small around 0.4 eV [91]. This was in contradiction with the optical absorption measurements and its solid state interpretation. S.

G. Louie [92]used a first-principle quasi particle theory which describes well the single particle properties of the fullerite, including the low band dispersion [93]. Like Lof et al. he pointed out the importance of the interaction term between quasi electrons and quasi holes in the hamiltonian to describe optical processes. They proposed the existence of a Frenkel exciton with an excitation energy of ≈1.6 eV and a further triplet exciton at 1.34 eV in the quasi particle bandgap of 2.3 eV. This large exciton binding energy could explain the observed discrepancy between the quasi particle gap and optical absorption threshold.
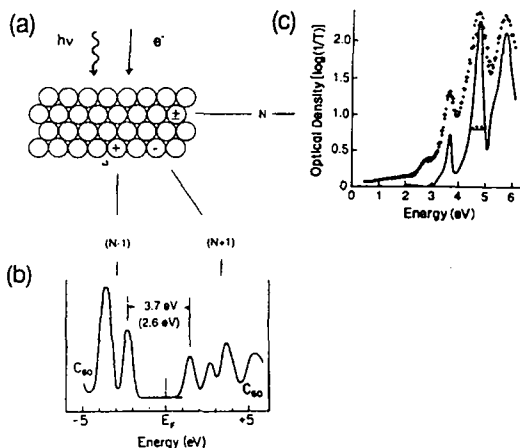

Fig. 7.2: (a) represents an array of C_{60} molecules exposed to photon and electron beams of variable energy, representing photoemission and inverse photoemission. The lowest energy optical absorption process corresponds to the creation of an electron-hole pair bound by the Coulomb energy on the same molecule, an exciton. Separation requires ionizing radiation that results in isolated electrons and holes, namely the (N-1) and (N+1) states of the molecular solid. The energy distribution of (N-1) and (N+1) states is measured by photoemission and inverse photoemission. The results from PES and IPES are reproduced in (b), referenced in energy difference to the Fermi level. The separation of HOMO and LUMO band centers is 3.7 eV and the extrapolated band edge separation is 2.6 eV. The latter approximates the transport gap. (c) compares optical absorption spectra for C_{60} in decline (lower curve) with C_{60} in thin film form. The dominant structures reflect dipole-allowed molecular transitions that are only slightly modified in the solid state. From [53].

There has been further support of the existence of the exciton by EELS (Electron Energy Loss spectroscopy) [94] and two-photon excitation measurements of C_{60} single crystals [95]. Transient absorption spectroscopy was capable to measure lifetimes of the excited states of C_{60}. For the free molecular system in solution (liquid or glassy) the first excited electronic state S_1 has broad absorption maxima at ca. 513, 759 and 885 nm with a lifetime of at least 1.2 ns [96].

From S_1 the molecule undergoes intersystem crossing to the triplet state T_1 characterized by a strong absorption maximum at ca. 750 nm [96, 97]. The triplet state is formed with a quantum efficiency close to unity and its intrinsic lifetime in frozen matrix is about 50 ms [98, 99]. In liquid solution at room temperature, triplet-triplet annihilation reaction is also observed which shortens the apparent lifetime [96]. Due to its long lifetime the triplet state can also be easily quenched by impurities [100] , which makes it difficult to measure reliable values. The transient spectrum of the solid state does not resemble the spectra of either the excited singlet state or the triplet state of monomeric C_{60} and has been attributed to a singlet exciton in its free and self trapped state with lifetimes of less than 15 ps and 250 ns, resp. [89]. A theoretical approach of Tsubo and Nasu [101] explicitly separated the intra- and intermolecular contributions to the Hamiltonian, and yielded the result that the oscillator strength in the region of 2.5 eV was considerably enhanced by intermolecular interactions. This result led to the conclusion that the absorption in this region in the solid state leads to a charge transfer exciton. Such a charge transfer exciton is expected to interact strongly with external electric fields and can be the dominant precursor of photocarriers [102]. The second transient absorption at 1.88 eV has been assigned as the exciton in its self trapped state. The triplet exciton at 1.68 eV was found to have lifetimes of the order of milliseconds. These spectroscopic data can be summarized in the following scheme shown in figure 7.3.
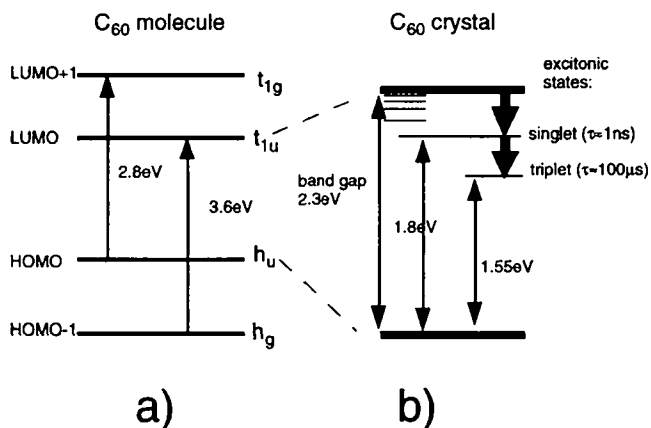

Fig. 7.3: Corrected electron energy levels for C_{60} in molecular (a) and solid (b) form extending the one particle approach of figure 7.1 to explain the experimental data of figure 7.2. The bandgap has been adjusted to 2.3 eV according to Lof. et al. [91]. Excitonic states exist in the optically forbidden bandgap, giving rise to optical absorption.

7.2 SHG & optical switching at thick C_{60} films (≥ 100 nm)

To explore the source of second-harmonic generation and the physical origin of the switching mechanism of C_{60} gas phase deposited films are studied under controlled experimental conditions.

The most prominent difference between films vapor deposited on quartz substrates and single crystal SHG characteristics of the preceding chapter is the missing rotational anisotropy of the SHG signal. This is consistent with the fact that thin films consist of small grains as could be seen in the TEM image of chapter 5. The grain size might be studied by changing the macroscopic area of the probe laser spot. However, due to the theoretical limitation of focusing the spot size cannot be made smaller than several micrometers, which is already the maximum grain size obtained in thin films under optimized growing conditions [56]. Furthermore it is a considerable experimental task to fix the rotational axis on one single grain with micrometer precision. The influence of this grain structure on the rotational anisotropy is evident and might be a further support for the interpretation of SHG from single crystal surfaces and the influence of disorder in chapter 4. As we will see later the switching process is influenced by the crystalline order, but is still a prominent effect even in polycrystalline films.

SHG studies have been performed with thin films deposited on insulating or semiconducting substrates. The first reported results came from H. Hoshi et al. [77] who studied the polar angle dependence for thin films on silica substrates. The first thickness dependent study was done by X. K. Wang et al. [78] at the fundamental frequency of 1064 nm. They found a square root behavior of the second-harmonic signal with the film thickness in contradiction to a mere surface contribution and interpreted it in terms of electric quadrupole contributions of the bulk crystal structure. Since they were working in air they could not exclude impurities as sources of the signal. However, their thickness dependent measurements were not conclusive enough and they saw only isotropic contributions in their azimuthal scans.

Koopmans et al. [80] performed UHV experiments on miscut silicon wafers using fundamental light in the wavelength range of 774 - 620 nm, which showed resonance enhancement at 688 nm ($2\hbar\omega = 3.6$ eV). The film thickness dependence as measured in-situ during film growth in reflection geometry at the resonance frequency. They could nicely observe the periodic SHG intensity induced by interference of interface and surface contributions. At thicknesses above 300 nm only the surface SHG seemed to contribute. In their study they found indications for weak electronic interactions between the overlayer and the substrate. It has to be mentioned that the silicon wafer was oxidized, therefore covered with an oxide layer some nanometers thick. However they could not definitively separate surface and bulk contributions. In a second study they interpreted the resonance in a molecular orbital scheme for C_{60} and used group theoretical arguments to separate surface, interface and bulk tensor components at the resonance frequency

for the isotropic thin films. The SHG resonance was explained in terms of the h_g (second highest occupied molecular orbital) -> h_u (HOMO) -> t_{1u} (LUMO) ->h_g excitation sequence of molecular C_{60}. The SHG signal was found to be predominantly of bulk character and dominated by the magnetic-dipole h_u-t_{1u} transition [79]. Later this interpretation was changed to a double resonance of the $^1T_{1g}$ excitonic state at 1.8 eV and the ($g_g + h_g$) - t_{1u} ED transition at 3.56 eV [103].

Wilk et al. [71] measured SHG in both transmission and reflection geometry from C_{60} films deposited by sublimation in a UHV chamber. Their study differed from that of Koopmans et al. in that they used fundamental light at 1064 nm. Thus, the second-harmonic frequency ($2\hbar\omega$ = 2.33 eV) is in the tail of the electric-dipole allowed h_u-t_{1g} transition of C_{60} [71]. While the results of Koopmans et al. were dominated by a bulk contribution with double resonance enhancement, including the input resonance with the magnetic-dipole transition at 1.81 eV, their results had contributions from both the surfaces and the bulk and are only nearly singly resonant at $2\hbar\omega$ = 2.33 eV.
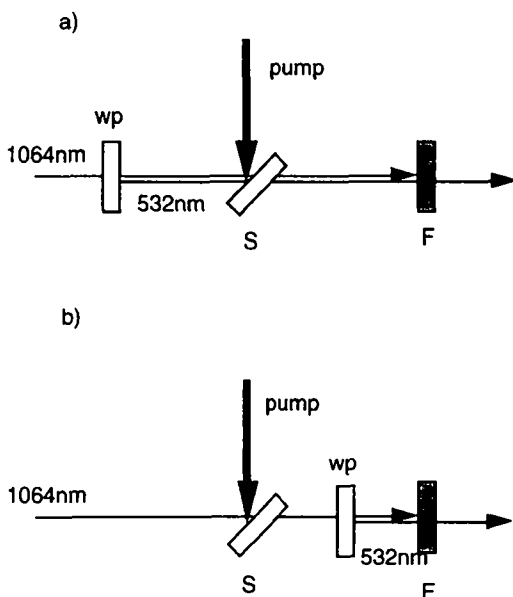

Fig. 7.4: Sketch of the experimental geometry for transient absorption measurements. (a) For 532 nm pulses that are generated in a crystalline quartz plate (wp) with a weak fundamental pulse at 1064 nm. (b) For the weak fundamental at 1064 nm after having passed the sample it generates 532 nm pulses in the wave plate (wp) that are detected.

The pump and probe experiments presented in chapter 6 have shown that the SHG depletion effect is not dependent on the polarization of the pump beam which excludes definitely third order nonlinear effects due to a high $\chi^{(3)}$ observed in four-wave mixing experiments [88]. Li et al. [74] have shown that C_{60} in solution can work as inverse saturable absorber so the question of linear absorption effects of the transient might play a role. This possibility has been ruled out in chapter 6 only for the fundamental wavelength at 1064 nm. With the transmission experiment sketched in figure 7.4 the transient absorption change due to the pump pulses were monitored. In figure 7.4a the set-up is shown by which the transmission is measured for a 532 nm beam generated by a quartz $\lambda/2$ waveplate (wp). The waveplate efficiency is much higher than that of the film thus dominating the measured signal. The measured transient absorption at 532 nm is shown in figure 7.5c. To measure the transient absorption at 1064 nm the waveplate is put behind the sample as seen in figure 7.4b. The results of the pump-and-probe transmission experiments are shown in figure 7.5. The linear absorption change is smaller than about 2 %, while the second harmonic signal generated in the C_{60} film is suppressed by 70 % under the same conditions as shown in figure 7.5a.
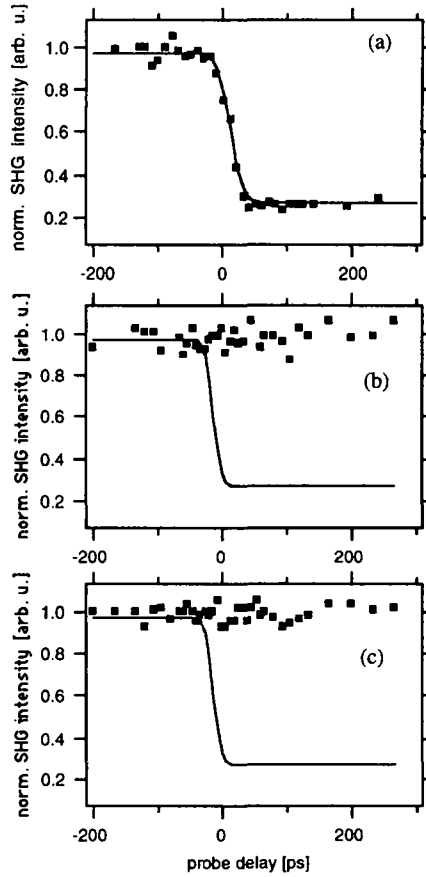
Fig. 7.5: Linear absorption transients taken in the geometry of figure 7.4 for C_{60} films. The pump-and-probe second-harmonic generation measurement is shown for comparison in (a). (b) transient at 1064 nm; (c) transient at 532 nm. No absorption effect to the pump pulse at 355 nm is observed in (b) and (c).

As pointed out in the single crystal experiment in chapter 6, the ratio of pumping photons per C_{60} molecules is lower than 4 %. This low ratio brought up the question of impurity effects. It is known from the literature that the long lifetime of the triplet exciton gives rise to many interesting photochemical processes. The reason is the possible excitation transfer onto other molecules like oxygen which show strong chemical reactivity in their excited state [100]. In this mechanism the oxygen induced etching of C_{60} to amorphous carbon under strong light illumination can be explained [104]. Without the presence of oxygen the already mentioned polymerization process will be favored.

In chapter 5 it was already shown that oxygen had a reversible intensity effect on the SHG signal. Following the in-situ SHG measurements in vacuum the influence of the pump beam in different environments has been tested. The pump efficiency at different oxygen pressures has been measured and did not show any influence on the pump and probe experiments as shown in figure 7.6. The same could be found in the single crystal experiments where second-harmonic signal suppression did not change when the experiments are undertaken in high vacuum (10^{-5} mbar).
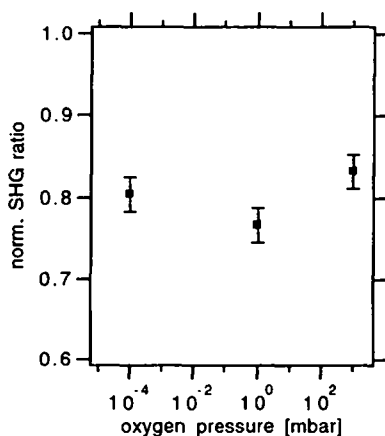

Fig. 7.6: Pump-and-probe normalized intensity for a C_{60} film grown and measured in-situ at 330 ps probe delay at different oxygen pressures in the vacuum chamber. The pump intensity is at saturation density of about 15 μJ/cm^2.

A second type of chemical transformation is the polymerization process. Since the vibrational modes are governed by the molecular character and the strong σ-bonds, the polymerization results in a loss of π-binding, which decreases the force constant of the σ-bond. This causes a
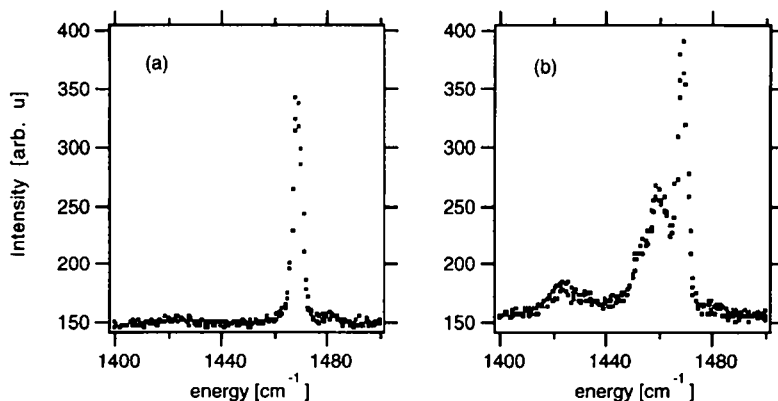
Fig. 7.7: Raman spectra of C_{60} films in vacuum in the region of the $A_2(2)$ mode measured with 1 mW focused on 5 mm². (a) shows the spectrum of the film after exposure to 30 μJ/cm² 355 nm pump pulses for 5 hours. (b) shows the spectrum of the same spot after polymerization with cw 514 nm laser light. The mode indicating polymerization appears at 1459 cm⁻¹.

frequency shift of 10 cm⁻¹ in the vibrational pinch mode down to 1659 cm⁻¹ as has been found by Eklund et al. [69].

In order to exclude polymerization in the pump-and-probe experiments in-situ prepared C_{60} films were exposed for about 5 hours to 355 nm pump pulses at 30 μJ/cm² and then measured with Raman spectroscopy at 514 nm using continuous wave illumination of less than 1 mW focused on about 5 mm². The sampling of one spectrum takes around 30 seconds. No signs of polymerization could be found as seen in figure 7.7a where only the Raman mode at 1469 cm⁻¹ appears. The polymerization is started by further illumination with higher intensities of the 514 nm line for some minutes. The polymerized state could immediately be detected in a low intensity measurement by the appearance of the additional line at 1459 cm⁻¹ (see figure 7.7b). Obviously polymerization does not occur in our pump-and-probe experiments due to the low light doses at 355 nm. It might in addition be possible that the 2 + 2 cycloaddition reaction efficiency is largely reduced for short pulses at low repetition rates (20 Hz) and that a further photochemical reaction step of the molecule in the triplet state is necessary. A second indication of an unpolymerized film is its solubility in chloroform even after several hours of pump treatment in vacuum. No polymer skins have been found on any of the UV pump pulse exposed films.
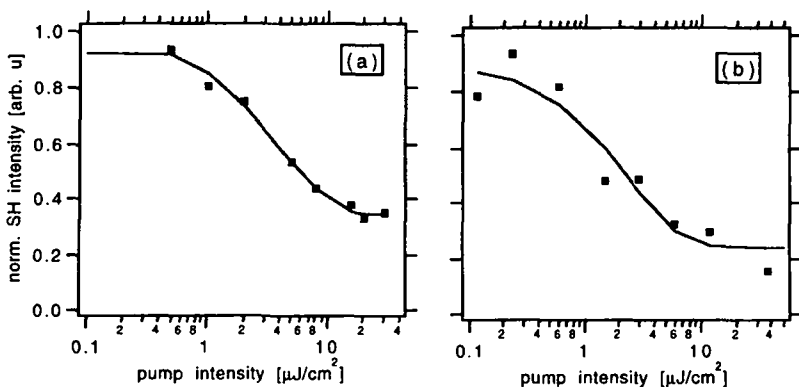
Fig. 7.8: Normalized second-harmonic signal at 330 ps probe delay as a function of pump intensity at 3.50 eV for C_{60} films prepared with different C_{70} impurity levels. With high purity (99.9 %) C_{60} (a), and a C_{70} impurity level of 1 % in the evaporation cell.

The low excitation density of C_{60} at SH signal suppression to 1/e (chapter 6.3) of only $8 \cdot 10^{-4}$ absorbed photons per C_{60} molecule might suggest the involvement of impurities in the suppression mechanism. The value suspiciously resembles the impurity content of the nominally 99.9 % pure C_{60} powder. Pump-and SHG probe experiments were therefore repeated for a C_{70} enriched film in order to check the influence of the major impurity, C_{70}. The C_{60} powder (99.9%, MER Corp.) has been mixed with pure C_{70} powder (96%) to increase the C_{70} impurity level by one order of magnitude. Figure 7.8 shows the efficiency of the pump pulse for two films with different C_{70} impurity level. The pump intensity at 1/e suppression is essentially the same, and does definitely not vary by one order of magnitude. This excludes the influence of C_{70} induced trapping effects and the possibility of exclusive generation of the second-harmonic signal by C_{70} molecules in solid C_{60} films.

7.5 Crystalline order

After we have ruled out any chemical impurity induced effect, one important structural effect was found for solid C_{60}. Figure 7.9 shows the dependence of the SHG signal suppression of the pump intensity for different C_{60} crystallinity. Figure 7.9(a) shows the situation for the single crystal, (b) for a film (1100 nm) deposited on a heated substrate and (c) for a film (2000 nm) deposited onto the substrate at room temperature. Absolute values of the SHG signal for different samples are difficult to compare. However, the normalized signal suppression has been found to vary strongly with the morphology of the solid state. This effect showed up for film thicknesses between 100 and 2000 nm, when the films were pumped with intensities

66

above the saturation of SH quenching. Figure 7.10 shows the intensity dependence for the probe delay at 330 ps for the highly polycrystalline film, which was grown onto a substrate at room temperature. Saturation intensity is reached for the films at intensities higher than 15 $\mu J/cm^2$.
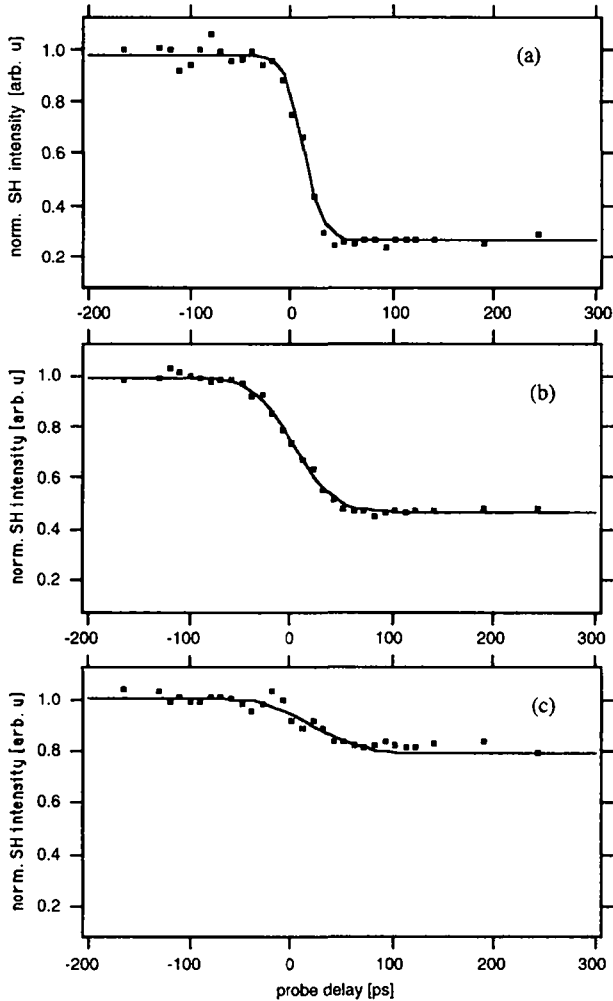

Fig. 7.9: Pump-and-probe SH transients with 3.50 eV pump energy in reflection from different samples of different structural quality. For (a) single crystal at 4 $\mu J/cm^2$. (b) and (c) are transients for thick (> 1000 nm) C_{60} films on quartz grown at different substrate temperatures $T = 160°C$ and $T = 20°C$, respectively. Shown are the transients for saturation pump density.
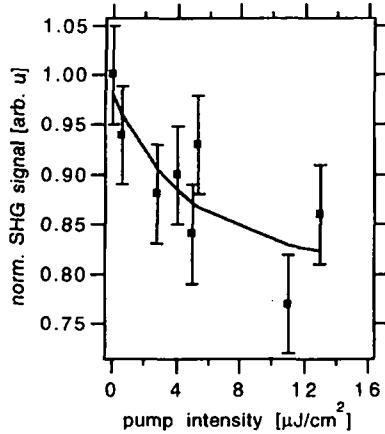
Fig 7.10: Normalized second-harmonic signal at 330 ps probe delay as function of pump intensity at 3.49 eV for a C_{60} film grown at room temperature onto a quartz substrate.

Henke et al [105] studied the crystalline ordering for the epitaxial growth of C_{60} on mica for different substrate temperatures ranging from room temperature to 200°C by X-ray scattering. They found a strong increase of crystalline order with temperature. The comparison with other growth studies [56] shows the same tendency. This result shows a possible relation between extension of crystallite size and SHG switching effect, which will be discussed in detail later in this chapter. It should be mentioned that all SHG studies cited in this work used room temperature growth conditions. Wilk et al showed in their in-situ SHG study AFM images of the grown films that exhibited grains of the order of several micrometers and mentioned as well difficulties in describing the initial stage of the thin film growth in their model [71]. This may indicate that even for molecular crystal systems the nonlinear response is very sensitive to the long range crystalline order. It is also possible that grain boundaries in the solid influence the SH signal from the bulk, a possibility which has not been considered in the references cited above. We will see in chapter 8 that interfaces reduce the lifetime of electronic excitations. Also grain boundaries may be very efficient in quenching excitation [106]. The increase of the unquenchable contribution with reduced crystal quality could thus result from significant SH contributions at grain boundaries.

7.6 Intrinsic solid state effect in C_{60}

Since photon induced reflectivity and absorption changes have been excluded as reasons for the switching effect and no correlation with impurities could be found in the preceding studies the effect must be considered to be an inherent C_{60} surface effect. By continuously changing the pump photon energy the SHG suppression efficiency has been analyzed.
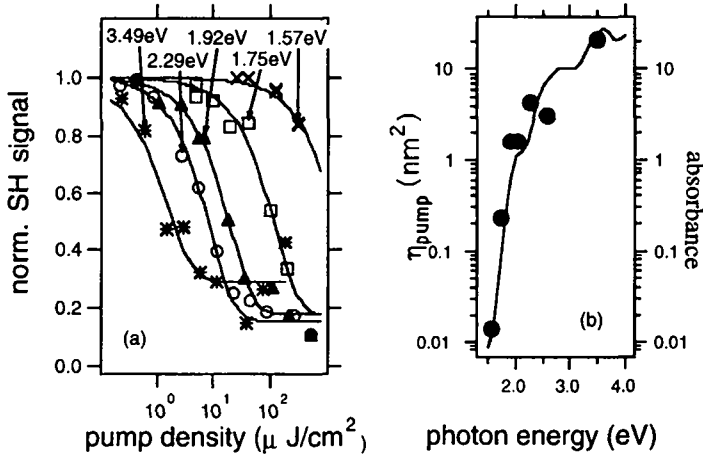

Fig. 7.11: (a) Quenching of the normalized SH signal of a thick film (ca. 250 nm) as a function of pump density for different photon energies at 300 ps probe delay. The solid lines are best fits to a single exponential. (b) SH quenching cross section as a function of photon energy (dots) compared to the film absorption (solid line) taken from Skumanich [107]. A scaling factor was used to overlay the two curves.

The intensity dependence of the quenching effect at 330 ps probe pulse delay has been measured for discrete photon energies of which some are shown in figure 7.11a. The fact that a significant cross section is still observed below the band gap of 2.3 eV indicates a substantial influence of excitonic states (see figure 7.3) on the quenching of the SH signal. The pump cross section η (see equation (6.10)) that quantifies the suppression efficiency of the pump photon, shows an onset of the quenching effect at 1.8 eV (see fig. 7.11b). The values follow the absorbance curve (inserted in fig. 7.11b) measured by Skumanich [107]. The agreement with this measurement shows that the absorbence is directly proportional to the pump cross section and demonstrates that the reduction in efficiency is only due to reduced absorption. Since the film thickness (250 nm) is bigger than the penetration depth between 3.56 eV (30 nm) and ≥ 2.5 eV (≈ 100 nm [87]) all incident photons are absorbed in the film. For a mere SH bulk

69

signal, the quenching cross section should be approximately constant. The experimental observation shows, however, a reduction in efficiency of more than one order of magnitude. It is thus very reasonable to consider the second-harmonic signal originating at least predominantly from the single crystal surface and excitations near the surface being the source of the signal reduction.

In the following paragraph the physical origin of the quenching will be discussed. As already mentioned in chapter 6 in the surface absorption model an effective cross section of the quenching by one photon between 1.6 eV and 3.6 eV can be given which corresponds to 19 nm^2. One might think of a delocalized excitation of this size, although this is unreasonable to suppose, since the excited molecular states that are predominately excited are assumed to be localized on one molecule (Frenkel excitons). Two different interpretations are possible in the framework of localized molecular excitations. Either a fixed excitation influences its environment over such a large area or a localized excitation has a sufficiently large probability to move from one molecule to the other by hopping.
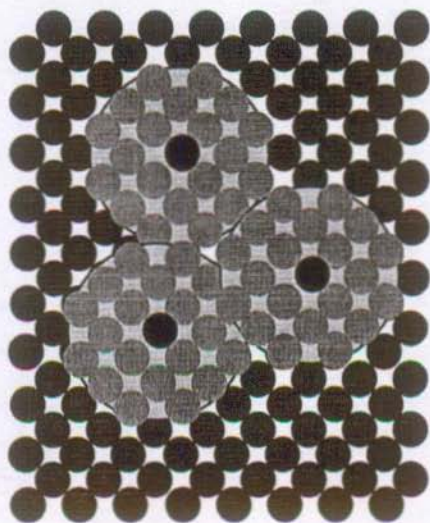

Fig. 7.12: Qualitative representation of the excitation cross section of the pump photons at the fcc(111) fullerite surface.

The cross section of 19 nm^2 corresponds to approximately 28 C_{60} molecules in the fcc (111) surface that can be reached in a random walk hopping model in the time of the pump pulse. In order to disturb the SHG the excitation has to "visit" these molecules on a time scale comparable to the laser pulse length. A lower limit for the resulting velocity can be given to be

≈1000 m/s. For a hopping process of excitons in molecular crystals a value of 60 m/s has been found in naphthalene [108]. Another possibility is that the exciton, even immobile localized on one single molecule can act as perturbation of the coherent phase of the second-harmonic process.

A. A. Villaeys et al. [109] developed a generalized susceptibility approach to transient nonlinear optical processes for the femtosecond time regime and could explain the oscillatory pattern in quantum beat measurements in organic compounds. Due to the molecular character of the C_{60} crystal the molecular density matrix formalism can be applied, which was developed to calculate the second-harmonic generation of molecular systems in the steady state case [110]. This theory was already successfully applied to the experiments of Heinz et al. for a rhodamine 6G layer on silica [111]. They could nicely reproduce the energy dependence of the two-photon resonant case. The formalism has been extended to a time resolved theory of the second-harmonic generation process, which may explain the nonlinear optical switching mechanism [112].
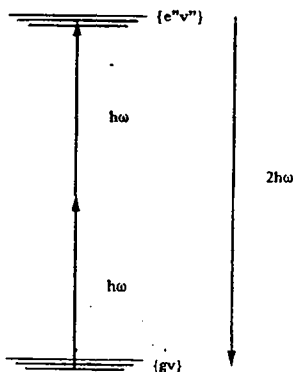

Figure 7.13: Energy-level schemes for the calculation of relaxation and dephasing of SHG in an molecular system for the non-resonant-resonant case. From Lin et al. [110].

The second-harmonic polarization is constituted of different contributions dependent on the resonant or off-resonant character of the second-order process. The combination scheme for the contributing situations are described by figure 7.13. In the case of C_{60} we are in the case of off-resonant/resonant energy levels, since the fundamental frequency is non-resonant. The dynamical evolution of the system, undergoing relaxation and dephasing processes is conveniently described by its density matrix $\rho(t)$ [113], and is derived from the Liouville equation

$$\frac{\partial \rho(t)}{\partial t} = -\tfrac{i}{\hbar} L_0 \cdot \rho(t) - \tfrac{i}{\hbar} L_1(t) \cdot \rho(t) - \Gamma \cdot \rho(t) \tag{7.1}$$

Where L_0, Γ, and $L_l(t)$ denote the zero-order Liouvillian of the unperturbed system, the damping operator, and the Liouvillian for the interaction between the system and radiation fields, respectively. Γ is the constant, which measures the perturbation of the SHG process and can be correlated to the pump pulse influence. Following the calculation for the NR - Resonant case, the influence of Γ can be studied, which corresponds to a dephasing of the microscopic SHG process. The influence of dephasing to the SHG has been demonstrated by Villaeys et al. and the results of their calculations can be seen in figure 7.14 a, b.
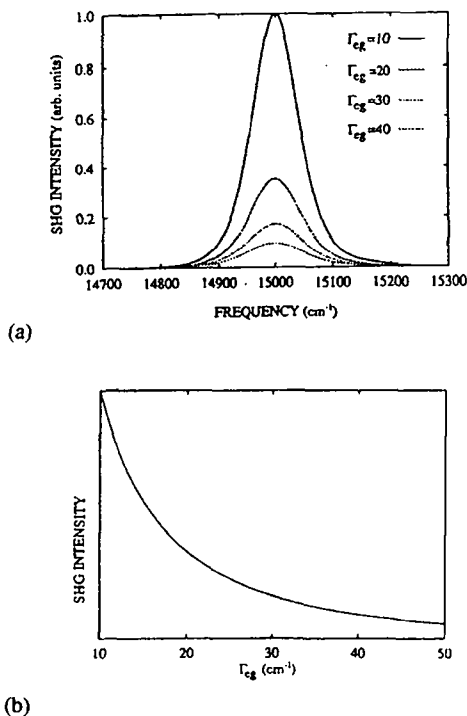
(a)

(b)

Figure 7.14: (a) Calculated frequency dependence of the integrated SHG intensity of a molecular system, for different values of the dephasing constants. (b) Variations of the integrated SHG intensity with the dephasing constants. From [109].

One may assume that in SH quenching the SH signal is reduced due to dephasing of the emitting states in the individual C_{60} molecules. The SH photons are then emitted not only in the direction of the fundamental beam but in all directions thus reducing the intensity measured by the detector. It is obvious that an exciton hopping onto a molecule in the process of emitting a SH photon will dephase the emitted wave. Since the dephasing takes place on a time scale of

some femtoseconds the process can be used to measure the excited state properties of systems in the picosecond range without retardation and will be used in the following to study buried interfaces of C_{60} solids.

7.7 Outlook

The possibility to explain the large effective SHG quenching volume by an incoherent transport process suggests the application of an elegant method to study diffusion of adsorbed species or excitations at surfaces. It was demonstrated for second-harmonic generation by Suzuki et al. [114] and Zhu et al. [115]. The idea is to create a spatial periodic pattern with a spacing $l_g = 2d = \frac{\lambda}{2\sin\phi} \cong 8\mu m$ by interference of two pump pulses, where ϕ is the angle between the two pump beams. In order to describe diffractive second-harmonic scattering from a surface grating along the x coordinate, the surface nonlinear susceptibility of formula 2.6 must be extended in a Fourier expansion as

$$\chi_s^{(2)}(x) = \sum_{n=-\infty}^{\infty} \chi_s^{(2)}(n) \cdot e^{ink_g x} \tag{7.2}$$

where k_g is the wave vector characterizing the grating of period $l_g = \frac{2\pi}{k_g}$. Under laser excitation at a frequency ω, a surface nonlinear polarization is induced with

$$\bar{P}_s^{(2\omega)}(x) = \sum_{n=-\infty}^{\infty} \chi_s^{(2)}(n) : \bar{E}_s^\omega \bar{E}_s^\omega \cdot e^{i(2k_x^\omega + nk_g)x} \tag{7.3}$$

Here $\bar{E}_s^\omega$ is the electric field of the pump beam at the surface, and the beams are assumed to be oriented so that the lines of the grating are perpendicular to the plane of incidence of the probe beam. The nonlinear polarization will lead to SH radiation emerging not only in the usual transmitted and specularly reflected directions but also in diffracted beams specified by the relation

$$k_x^{2\omega}(n) = 2k_x^\omega + nk_g \tag{7.4}$$

with $n = \pm 1, \pm 2, \dots$. The angular spacing between the diffracted beams for second-harmonic radiation will be half as great as for the linear diffraction of the fundamental radiation [116]. We now consider the time dependence of the intensity in the diffracted beams. The form of the diffusion equation

$$\frac{\partial\Theta}{\partial t} = \frac{\partial}{\partial x}\left(D\frac{\partial\Theta}{\partial x}\right) \tag{7.5}$$

implies that each Fourier component of the grating profile decays in a simple exponential fashion whenever the density dependence of the surface diffusivity D can be neglected. Assuming that the surface nonlinear susceptibility $\chi_1^{(2)}$ varies linearly with the excitation density, we obtain a time variation in the first-order diffracted second-harmonic intensity of

$$I_{SH}^{n=1}(t_0 + \Delta t) \propto \left|\Theta^{n=1}(t_0 + \Delta t)\right|^2 = \left|\Theta^{n=\pm 1}(t_0)\right|^2 \cdot \exp\left[\frac{-2D(t_0 + \Delta t)}{\left(\frac{l_g}{2\pi}\right)^2}\right] \tag{7.6}$$

where $\Theta^{n=1}$ denotes the first Fourier component of the adsorbate density. By monitoring the temporal decay of the diffracted pump-and-probe second-harmonic signal the diffusion constant D can be determined.

The grating experiment has been formed by spatially and temporally overlapping two pump pulses of equal intensities with photon energies of $\hbar\omega_x = 3.5$ eV under angles $\phi/2 = 0.65°$ off the surface normal. The diffraction pattern of the SH generated from the probe beam $\hbar\omega_0$ can be measured by rotating the sample about an axis perpendicular to the plane of incidence. A typical result of a second-harmonic diffraction measurement is shown in figure 7.15 at a probe delay of 0 ps.

Beside the specular second-harmonic signal the first order diffraction peaks is detected at angles of $\pm 2.54°$ off the specular peak as expected from equation 7.4. The sharp angular resolution of $0.025°$ results in a sharp grating profile. The second-harmonic intensity of the specular peak is suppressed to around 20% during the creation of the grating. Its temporal behavior is the same as for the normal pump-and-probe SHG experiments. The specular peak stays constant over the accessible delay time. The first order diffraction shows a completely different behavior with only a sharp peak of around 20% of the suppressed first order second-harmonic intensity. The peak duration is in the range of the time resolution of the laser pulses. The resulting propagation would be in the range of $2.0 \cdot 10^5$ m/s which is considerably too large for any exciton diffusion processes.
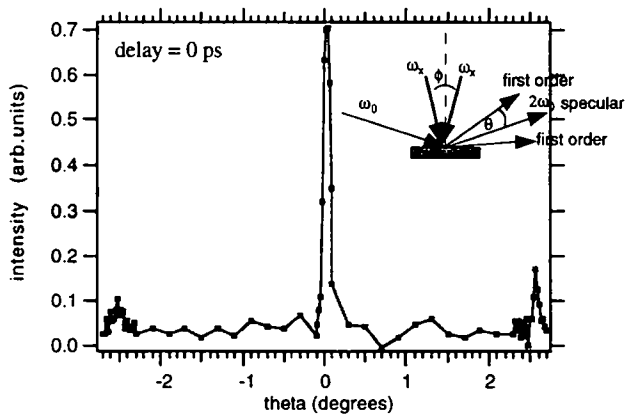

Figure 7.15: Second-harmonic intensity from a diffraction pattern of 8 μm micrometer spacing, generated by the interference of two pump pulses at 3.5 eV (see inset). Beside the specular peak the first order diffraction peaks are observable at the angular positions $\theta = \pm 2.54°$.
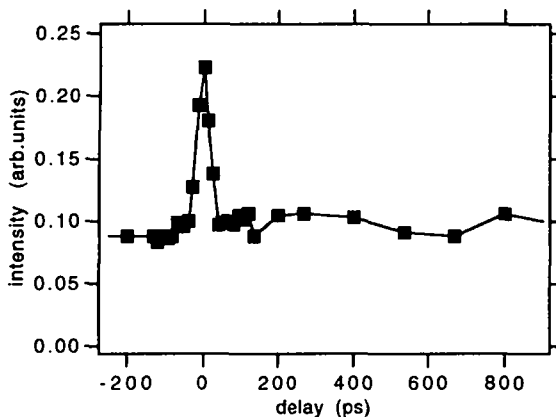
Fig 7.16: Pump-and-probe second-harmonic signal of the first-order diffraction peak that indicates a decay of the excitation grating faster than the temporal resolution of the experiment (45 ps).

A diffusion into the bulk does not occur since the specular intensity does not recover, which indicates no change of excitations at the surface. Since the value of $2 \cdot 10^5$ m/s and differes by orders of magnitude from typical propagation values about 60 m/s for excitons in molecular crystals (see 7.6) coherent processes might play a dominant role. Further experiments with different grating periods and at different wavelengths or temperatures have to be done to identify this process.

8. Interface states

As we have seen in chapter 6 and 7 the time and energy dependence of the SHG quenching for thick films of the order of several hundred nanometers are very similar to the ones of the C_{60} single crystal. From the above discussion it is reasonable to suppose that the second-harmonic signal is generated at the vacuum-C_{60} interface and is therefore sensitive to the properties of the excitons located near the surface. The missing decay of the SH quenching within one nanosecond suggest that excitons stay at the surface of the solid longer than in the bulk which hints at surface-trapped species. With respect to the described observation it is interesting to notice that a similar SH quenching effect was observed for C_{60} films protected by a SiO_2 capping and exposed to corona poling fields at 140°C [117]. Corona poled films were reported to exhibit a substantial increase in SHG efficiency. The quenching of SHG upon excitation by a UV pump pulse was interpreted as a generation of free carriers compensating for the effect of the exposure to the poling field. The sensitivity of the SH signal to the electric field at the surface is understandable, however, the effect may be different to ours. The quenching mechanism of pristine C_{60} is a more general effect. Up to now only switching at the C_{60}/vacuum interface has been considered. With decreasing film thickness the pump radiation will also reach the buried quartz/C_{60} interface as seen in figure 8.4.
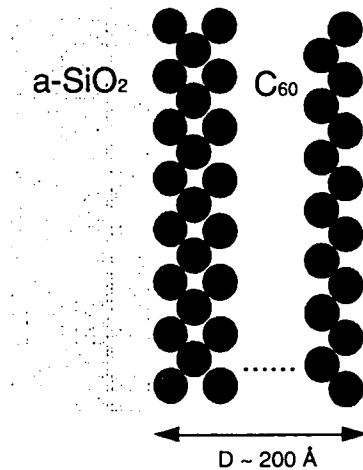

Fig. 8.1: Schematic picture of the quartz-C_{60} interface for a thin film.
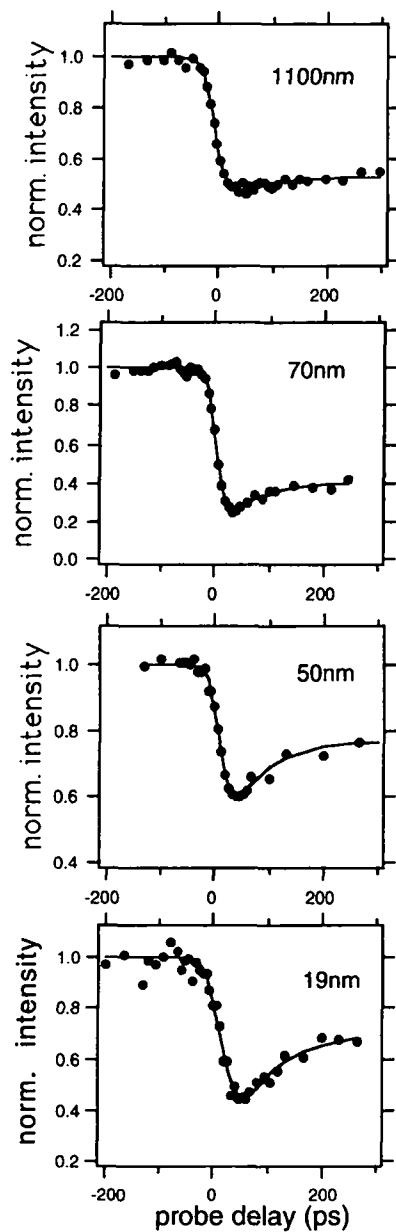
Fig. 8.2: 3.49 eV pump and SHG probe transients for films of *decreasing thickness as indicated in the figure.* The 1100 nm thick film exhibits a response similar to the single crystal (see figure 6.3). With decreasing film thickness a short lived state (70 ps) becomes prominent.

78

In the following, results for films below 100 nm thickness are discussed. Figure 8.2 shows the results of the pump-and-probe experiments in transmission geometry at a pump wavelength of 355 nm. In addition to the long lived state observed for crystals and thick films (see fig. 8.2a) a new state of reduced life time in the picosecond regime evolves for decreasing film thickness (fig. 8.2 b, c, d). This new state requires to extend the simple model of chapter 6 and to introduce two spatially separated states S_1 and S_2. We will see later that S_1 corresponds to the long lived state at the film surface while S_2 corresponds to the short lived (interface) state. The second-harmonic signal will then be described by the population of the ground states S_0^s and S_0^i and the excited states S_1^s and S_2^i which follow the rate equations

$$\frac{dn_0^s}{dt} = \frac{n_0^s}{\tau_1} - P^s(t) \qquad \text{and} \quad \frac{dn_0^i}{dt} = \frac{n_0^i}{\tau_2} - P^i(t) \tag{8.1a}$$

$$\frac{dn_1^s}{dt} = -\frac{n_1^s}{\tau_1} + P^s(t) \qquad \text{and} \quad \frac{dn_2^i}{dt} = -\frac{n_2^i}{\tau_2} + P^i(t) \tag{8.1b}$$

where $P^s(t)$ and $P^i(t)$ stand for the temporal pump pulse shape at the surface and the interface, respectively. The second-harmonic signal will consist of coherently superposed contributions of the susceptibilities of the populated states according to

$$S_{SHG} \propto \left| n_0^s(t) \cdot \chi_{S_0^s}^{(2)} + n_0^i(t) \cdot \chi_{S_0^i}^{(2)} + n_1^s(t) \cdot \chi_{S_1^s}^{(2)} + n_2^i(t) \cdot \chi_{S_2^i}^{(2)} \right|^2 \tag{8.3}$$

In order to determine the experimentally measured normalized signal one has to take into consideration the temporal form of the pump pulse, which is done by the convolution of the expression with a Gaussian $G(t)$

$$I_{norm}^{SHG}(t) = \frac{I^{SHG}(t)}{I_0^{SHG}} = \left| \sqrt{S(t-t')} \circ G(t') \right|^2 \tag{8.4}$$

We get analytically for $\tau_1 \to \infty$ for the long-lived state

$$I_{norm}^{SHG}(t) = \left| A_0 + \frac{A_1}{2}\left[1 - \text{erf}\left(\frac{t}{\sqrt{2\sigma^2}} \right) \right] + \frac{A_2}{2} e^{-\frac{t}{\tau_2}} \cdot e^{\frac{\sigma^2}{2\tau_2^2}} \cdot \left[1 - \text{erf}\left\{ \frac{1}{\sqrt{2}} \cdot \left(\frac{\sigma}{\tau_2} - \frac{1}{\sigma} \right) \right\} \right] \right|^2 \tag{8.5}$$

Where erf(t) denotes the error function defined as

$$\text{erf}(t) \equiv \int_{-\infty}^{t} \frac{1}{\sqrt{2\pi\sigma^2}} \exp\left(-\frac{x^2}{2\sigma^2} \right) dx \tag{8.6}$$

σ the Gaussian pulse width and A_0, A_1 and A_2 the effective strengths of the populated states. They are not important in the following, since the time constants are the important fit parameters to describe the measured results and only relative quantities will be considered. This formula

fits well the experimental results and the lifetimes of the excited states can be determined. Typical values for the rapid decrease of SHG are around 35 ± 5 ps, which coincides with the pulse width σ of the Nd:YAG laser system. The fitted value τ_2 for the interface state has been determined to about 70 ps, which is considerably shorter than the exciton state at the C_{60} surface. It is however also much too long for bulk states involving charge carriers [75] or free excitons [89], that play a role on the subpicosecond time scale.

One possible explanation for the 70 ps state is the appearance of a quantum confined excitonic state. In a study of multiple quantum wells of crystalline organic semiconductors a continuous reduction of exciton life time with decreasing film thickness was reported which results from the squeezing of the exciton volume [118]. Even though the layer thickness in the present case is of the same magnitude (<100 nm) the fact that we see a state with a life time which is independent of film thickness suggests that this model is not compatible with our observation. This is elucidated further, by the pump pulse intensity dependence of the short living state shown in figure 8.3. Pump efficiencies were measured at different time delays for the short and long living state.
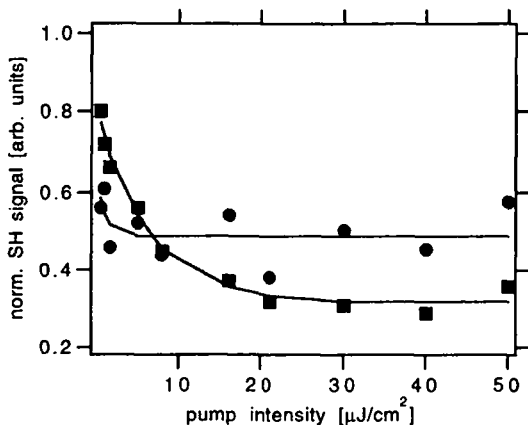

Fig. 8.3: Quenching of the normalized SH signal for a thin (≈ 30 nm) film as function of pump density for 3.5 eV photon energies at different probe delays. The dots show the measured dependence for the short-lived state at around 15 ps delay the squares the same measurement for the long-lived state at 330 ps delay. An explanation is illustrated in figure 8.4.

For decreasing film thickness, the ratio of the amplitude of the short lived state and the amplitude of the long lived state increases. This ratio is proportional to the ratio of the pump intensities present at the front of the film and the pump intensity at the back of the film for the known extinction depth of C_{60} for the 3.56 eV light of 30 nm [60, 87]. The absorption of the fundamental and SH photons can be neglected in this estimate. The attenuation of the pump

pulse P_s through the film explains furthermore the different pump power dependence of the two states shown in figure 8.3. One might consider a decreased pump cross section for the short lived state, but the real explanation is an attenuated pump intensity $P_i = P_s \cdot \exp(-\alpha d)$ at the internal interface, due to the finite penetration depth of the pump beam. This result further supports the assignment of the short lived state to the C_{60}/quartz interface, rather than a confinement effect.
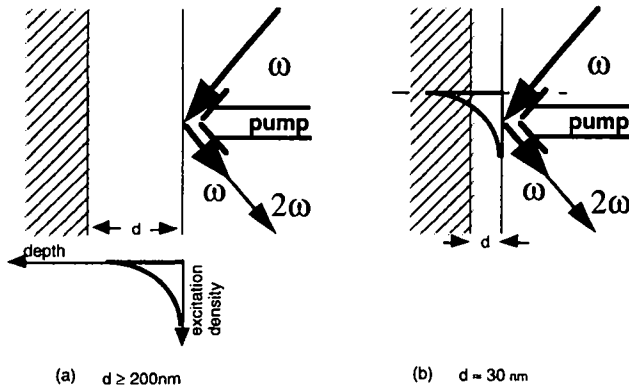

Fig. 8.4: Schematic image of the geometry of the pump-and-probe experiment for a thick ($\geq$ 200 nm) (a) and a thin ($\approx$ 30 nm) film geometry. The excitation density generated by the pump pulse has been added to illustrate the different concentration of excited states at the quartz/C_{60} interface resulting to the different behavior in figure 8.3.

The lifetime of 70 ps lies between the lifetimes of the free singlet exciton (< 20 ps) and its self-trapped form (250 ns). It is very likely that we are dealing in both cases (the surface and the internal interface) with similar types of excitations perhaps an interface trapped form with lifetimes of some pico- to nanoseconds. Interface excitons have a shorter lifetime due to defect induced recombination. Interface states can be quenched by the influence of a neighboring dielectric [119] due to excitation transfer is changed [120].

The small difference between absorption spectra of isolated molecules and the molecular crystal is regarded as an indication of the weakness of interaction between the molecular species in its solid state resulting in rather localized electronic ground states. Studies on C_{60} adsorption on metals and semiconductors have demonstrated a strong interaction leading to charge transfer and covalent bonding and can be measured by conventional techniques [54]. In these cases the electronic properties of the C_{60} layer at the interface are substantially altered. The coupling at the C_{60}/quartz interface will be much weaker. This relatively small interactions can be observed by the pump-and-SHG probe measurements described in this thesis and may serve as a tool to

study these interactions in detail. A possible approach and first results will be shown in chapter 9.

In this context one may now speculate about the role of internal interfaces in polycrystalline films. Extreme situations can be imagined for states at the C_{60}/C_{60} interfaces at the grain boundaries. If the life time of the exciton reduces far below our experimental resolution (45 ps) the short lived state will no more be observable. At the same time the long lived state will only exhibit a small amplitude even for large pump intensities. This resembles the observations for thin films with grain sizes smaller than several nanometers. As a consequence one would ebserve a "bulk" signal generated at internal interfaces which cannot be quenched due to the short life time of the excitation.

9. Excitation transfer

In chapter 8 it was shown that we have access to excitations at buried interfaces with the nonlinear pump-and-probe technique so that this method can be used to study the dynamical properties of electronic excitations at the interface. The coupling between the excited system and the substrate was constant for C_{60} on quartz. In this chapter the method will be applied to a new system in which the coupling can be adjusted. This is done by controlling the spatial distance between the excited molecule and the substrate. In the actual experiment a variable spacer layer will be inserted between a thin C_{60} film and a thick metal film. This allows to study the excitation dynamics in a range where classical energy transfer but also electron (hole) tunneling has to be considered. Most experiments in the past used rare gases condensed on solid substrates as spacerlayers. This procedure suffers, however, from experimental problems in the region of very short distances as seen for the experiment of Rossetti et al [121]. The organic spacer layer used in this thesis does overcome this problems since it is easier to control in this distance region.

In this chapter a system will be presented that might serve as model system to understand the contributing physical processes and that will be examined by STM and by pump-and-probe SHG.

9.1 Organic spacer layer

In the beginning of the 80ies long chains of amphiphilic molecules like fatty acids with high dielectric constants were used as insulating layers to study tunneling processes between metal electrodes. But real conductivity measurements were perturbed by hopping layer-to-layer electron conduction effects. Many of these preparational problems were later assigned to the low longtime stability of the layers. Pinholes and inhomogeneities in the films lead to failing of most of these studies especially when metal electrodes were evaporated for classical conductivity measurements.

On the other hand, distance dependent lifetime measurements of excited molecules deposited on top of these Langmuir-Blodgett layers could nicely reproduce the theoretical results of classical electrodynamics, which had been already predicted by Sommerfeld [122], studying the radio wave propagation near the earth's surface. The similarity of this system to the coupling of short-range dipole fields to surface waves lead to a good theoretical understanding of the underlying physical processes.

Drexhage studied the phosphorescence of dye molecules as function of distance to a substrate [119]. He used metal and insulator substrates on which Langmuir-Blodgett (LB) layers with a sheet of europium complexes were deposited that act as atomic oscillators (see figure 9.1). His study concentrated predominantly on the periodic behavior for larger distances above 2000 Å.
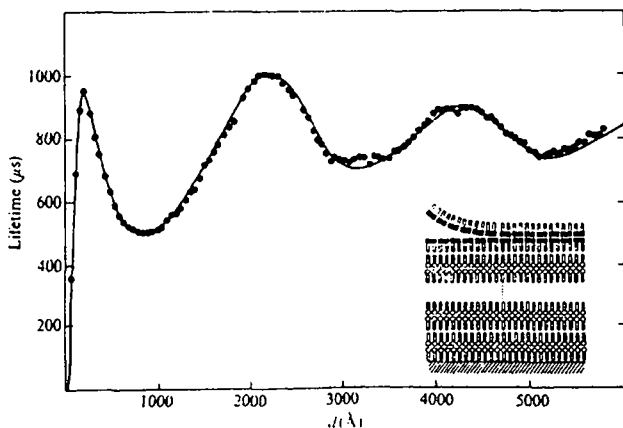

Fig. 9.1: Comparison of experiment (dots) and electromagnetic theory (solid curve) for the fluorescence lifetime of an excited europium complex as a function of the emitter molecule distance d above a silver substrate. Inset: construction of a spacer layer of fatty acid by the Langmuir-Blodgett technique. From [2].

The above mentioned problems prevented experiments in the region very close to the surface. Several other authors had to work under difficult experimental conditions (UHV, 4 K, etc...) to achieve small distances either due to the large surface reactivity of metals and its undefined surface structure (Pt, Al, Ag and even Au), complex spacer layers (CdAr, Ar, NH_3) or complex toplayer sensing molecules [121, 123, 124]. Since the early 90ies a new class of organic spacer layers for metal surfaces is known, thiols, which chemically passivate noble metal surfaces and define the distance to the surface. They build compact monolayers and inhibit metal atom diffusion through them depending on their chemical nature. Low energy electron techniques destroy them [125], which make them on the other hand useful for electron beam lithography [126]. General conductivity measurements have not yet been performed neither luminescence measurements. STM images of thiols on metal surfaces reveal super-structures that are discussed to have its origin in the lateral interaction between the adsorbed molecules [127]. Rubahn et al. measured recently indirectly the lifetime of sodium atoms on top of a thiol spacer layer by two photon laser fluorescence [128].

Of special interest are systems in which charge carriers have to pass a tunneling barrier between conducting and semiconducting materials (Metal-Insulator-Semiconductor systems). The electron transfer through insulating barriers is one effect which cannot be described by classical physics. Experimental studies have been done in the past using thin films of inorganic spacer layers [108]. A new phase of interest started with the development of the STM, which was meant to be restricted to conducting and semiconducting surfaces. Later it was found that it is also possible to image organic molecules on metal and semiconducting surfaces, which is still a subject of controversial discussions [129]. The major question might be brought to the point: What can be seen in the STM images, the real electronic structure of the adsorbate or its image in the electronic structure of the underlying substrate? Another unanswered question concerns the time scale of tunneling processes which is theoretically extensively studied but for which few experiments exist [130]. Besides this fundamental interest the understanding of the transfer of excitation from adsorbed molecules to solid substrates is of technological relevance since this effect is used in solar cells, in which the transfer of electrons from sensitizing molecules near the surface to the metal or semiconductor electrodes is used.

9.2 Experimental

In this chapter the pump-and-probe SHG technique is extended to study the interaction of the excitation in an adsorbed C_{60} molecule with a metal surface. Essential for the success of the experiment are the following points:

1. Thin gold films can be prepared as almost perfect single crystals, with extremely flat surfaces so that perturbing effects from field inhomogeneities induced by roughness can be excluded.

2. The thiol molecules clean the metal surface during their adsorption process chemically and prevent them from contamination. They are transparent over a wide frequency range, inert and can be used in defined lengths to control the spacer layer thickness. No orientational effects like birefringence have been observed for the used n-alkane thiols.

In this chapter the preparational procedure and its control by the STM are described.

9.2.1 Preparation of thin gold films with almost perfect Au(111) surface

Most studies of excitation transfer to metal surfaces have been performed with thin metallic films either sputtered or evaporated onto insulator substrates. Their surface structure can be considered in most cases highly amorphous (fig. 9.2a). When annealed for short times near to it's melting temperature in a Bunsen flame Cu, Ag or Au surfaces are polycrystalline with (111) terraces of less than 100 nm size (fig. 9.2b), [131].

For STM experiments and other local probes this might be sufficient. However, for optical experiments especially with highly spatially coherent laser light that averages over the large area, important features can be washed out. An example is the rotational anisotropy of the surface which is lost in vapor deposited films. So the microscopic and macroscopic quality of the surface should already be known, when studying its dynamics.

Gold films evaporated on mica, even subsequently flame annealed, yield Au(111) terraces of 100 nm maximum width that are separated by rough surface regions of several nanometers in height. Therefore a new preparation step has been added to get large homogenous single crystal terraces, with minimum macroscopic roughness. The as before prepared gold/mica samples have been flame annealed and afterwards glued onto flat substrates (silicon wafer). By chemical means the mica can be stripped of the gold film in organic solvents (THF, Aldrich, anhydrous) to expose the original gold/mica interface. Great care has to be taken to completely remove the mica layer. Further details can be found in the literature [132] .
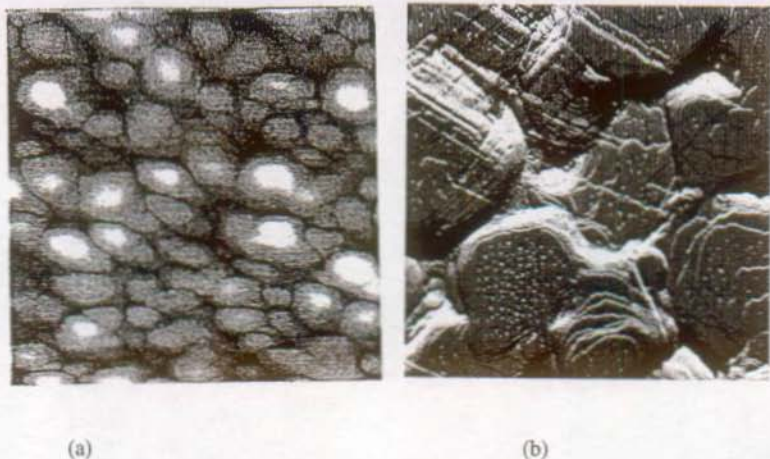
(a)   (b)

Fig. 9.2: STM images of gold films evaporated on heated mica: (a) at
50°C showing a rough surface (from [133]) and (b) at 300°C showing
large (111) faceted terraces. Image sizes: (a) 250 x 250 nm, (b) 300 x
300 nm.

The macroscopic roughness is defined by the cleaved mica surface as seen in figure 9.3b, c
where gold has been deposited on mica, that has been removed without additional flame
annealing. No rough region can be found, but the terraces are small compared to figure 9.3a.
Additional substrate heating during the deposition process and subsequent flame annealing
increases the width of the terraces and only monoatomic steps are seen over the whole film
surface (fig. 9.3d)

In this study gold (99.9999 % purity) was evaporated in a diffusion pumped vacuum chamber
at a base pressure of 10^{-6} mbar. The mica substrate is cleaved immediately before being
installed in the preparation chamber and is then degassed for at least 12 hours to remove water.
During the evaporation onto the substrate its temperature is held at 600 K and the deposition
rate of 1 Å/s is controlled by a quartz balance. After deposition of 200 nm of gold the substrate
is cooled down to room temperature and immediately cut into round pieces that are glued onto
silicon wafer discs. The samples are afterwards heated for one hour at 413 K. Immediately
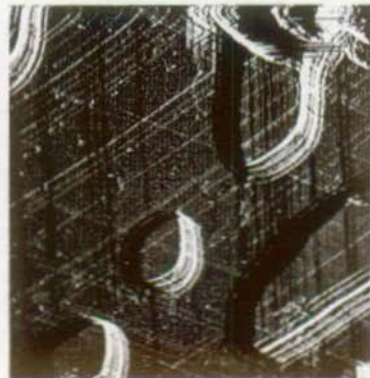before further treatment the mica was stripped off in THF (Fluka, anhydrous).

a)

b)

c)

d)

Fig. 9.3: STM images of gold surfaces prepared by the procedure described in the text. (a) Gold surface (as in fig. 9.2). Gold surface that was attached to the mica substrate where the substrate temperature during deposition was held at 50˚C (b), at 300˚C (c) and at 300˚C with additional flame annealing before lifting the mica (d). Image sizes: 300 x 300 nm.

9.2.2 Passivation of the gold

Most of the previous studies on thiol adsorption on metal surfaces were done using ellipsometry and contact angle measurement. It is generally accepted that the adsorption process takes place on two time scales. In a first step the adsorption follows Langmuir kinetics [2] and can be described as the chemical reaction of the thiols with the gold surface [134, 135]. The time constant depends mainly on the concentration of the thiol solution. There is still some discussion about the influence of the chain length. As a general rule it has been accepted that the longer the chain the faster the adsorption [136] which seems to be due to the chain-chain van-der-Waals interaction. The thickness of the spacer layer can be changed by choosing the number of methylene groups of the adsorbed molecule (fig. 9.4).
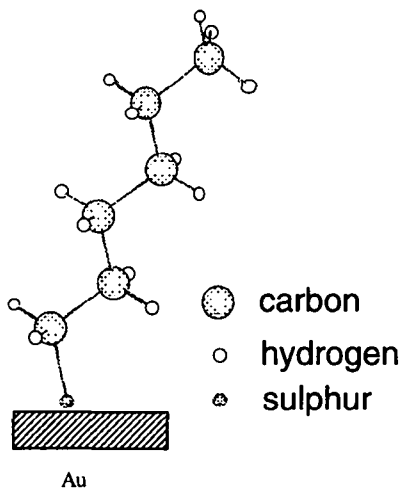

Au

Fig. 9.4: Schematical picture of a n-hexanethiol deposited on a gold surface. The sulfur group secures adhesion to the gold. The length of the molecule can vary using different numbers of methylene (-CH$_2$-) groups in the alkyl chain. The methyl group terminates the molecule and can be interchanged with different chemical groups.

The exact adsorption mechanism has not yet been well understood, but it is generally accepted, that it is connected with strong corrosion of the gold surface and that gold-molecule particles go into solution [137]. This corrosion process can be demonstrated eg. by using the STM tip to remove locally by the thiol corrosion several layers of gold from the surface [138]. By dipping the STM tip in a thiol solution, molecules can be brought near the tunneling contact. During scanning a particular area gold atoms are removed from the substrate. If the probed area is increased after several scans a rectangular hole is observed which corresponds the rectangle that has been scanned before. The corrosion process is highly concentration dependent and not yet

understood in detail.

However, after the gold surface is nearly completely covered with thiol molecules it is passivated against further corrosion. The second step in the adsorption process has been identified as orientational self-organization of the aliphatic carbon chains taking place on a longer time scale [139], [140]. The structural order in the layer depends on several factors. With decreasing chain length the stabilizing van-der-Waals interaction between the molecules becomes weaker which has been taken as possible explanation why the ellipsometric data deviate from the linear behavior in figure 9.5 [135]. These experiments of the AT&T group and further wetting measurements were explained with the present understanding of thiol layers on gold being disordered for chain lengths n < 10. However ellipsometry needs to include the dielectric constant as parameter to evaluate thin film thicknesses in the nanometer range. Evans et al. [141] argued on the basis of surface potential studies this constant to be chain length dependent due to screening of the chemically induced dipole in the adsorbed species R^+-S^--Au^+. This effect induces nonlinearities for short chain molecules which have not been taken into account for the analysis of previous ellipsometry data.

As in other organic spacers like LB-films irreversible disorder can be induced by heat. Even if thiols do not desorb for temperatures lower than 500 K [142] IR vibrational spectroscopy revealed a temperature induced order-disorder transition in the hydrocarbon chains around 370 K with increasing gauche conformation in the molecule [143]. That means that the molecules rotate around the carbon-carbon bonds. Nevertheless, the appearance of different phases in STM images even for hexanethiol [116] is a good indication for highly ordered films. Figure 9.6a shows that in STM images even without molecular resolution of single molecules these different phases can be observed indicated by the domain boundaries in the decanethiol layer. In this figure there are still etching pits observable, left over from the corrosion process during the adsorption. They are generally one gold layer deep and are also covered with thiols at the bottom [116]. They can be removed in an Oswald ripening process during annealing [144].

The photochemical stability of thiols, which is important for the pump-and-probe experiments where UV wavelengths are used, has been proven even for intense radiation in the range of 190-200 nm. This radiation was not able to break the C-S bond, which is known to be even stronger than the S-Au bond [145]. In contrast they seem to be highly sensitive to low energy electrons (< 3 keV) that are generally used in Auger spectroscopy [125].
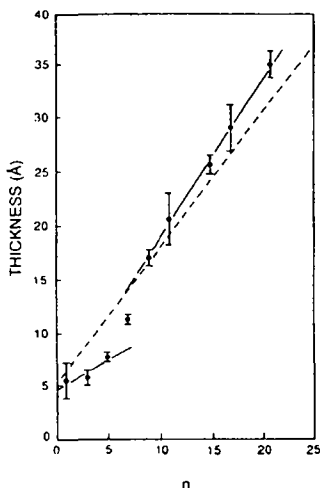
Fig. 9.5: Measured film thickness (dots) of n-alkanethiols adsorbed on gold; ellipsometric determined thickness (solid line) and estimated thickness for fully extended chains normal to the surface in Å (dashed line) are plotted against the number of methylene groups in the chain, n. From [135].

In this study commercially available thiols (Merck, p.a.) from n = 5 to 17 have been used, with standard concentrations of 1 mmol in ethanol (Merck, p.a.). Gold substrates were generally immersed in the solution for at least 12 hours to ensure good ordering of the layers. Only n-alkanethiols, with a methyl end group, has been used as spacer layers. They are compact, optically transparent and chemically inert, so that chemical reactions between the adsorbed molecule and the spacerlayer can be excluded. Either new prepared samples or cleaned samples were used. They were cleaned in chloroform (Fluka, p.a.) to remove the C_{60} layer and afterwards boiled in hot isodurene (Fluka, 90%) and furthermore heated to 250°C in an air circulated oven to remove the thiol layer. The next deposited thiol layer consisted always of molecules of longer chain length since they are known to replace residual shorter chain molecules.

9.2.3 Deposition of molecules onto passivated gold surfaces

Figure 9.6a shows the thiol covered gold surface before and Figure 9.6b after deposition of less than a monolayer of C_{60}, where the substrate was held at 358 K during the deposition process. The temperature did not exceed this value to prevent thiol desorption or temperature

91

induced disorder while still assuring high C_{60} mobility to form ordered crystalline structures. IR spectroscopy revealed no conformational disorder in docosane thiols films for up to 400 K heating in an inert atmosphere [146]. In figure 9.6a and b the etching pits are still present and domain boundaries (imaged as depression lines, $\approx 3\text{Å}$ deep) between different compact thiol phases are observable due to the short time annealing at elevated temperatures. The C_{60} molecules are even at room temperature still mobile but accumulate at imperfections like steps and domain boundaries [147]. Larger aggregates can be found in the etching pits (Fig. 9.6c, d), which are also completely covered by thiols.

Metal diffusion has been reported through different kinds of thiols, depending on the type of metal and the chemical activity of the functionalized group of the thiol. An overview can be found in [148]. In this study the substrate for the C_{60} molecules is formed by the inert methyl end group has been used and no penetration of the C_{60} molecules into the compact thiol layer or into the domain boundaries could be observed by STM for several hours. For the pump-and-probe experiments C_{60} layers were deposited onto the passivated gold substrate under the same conditions as for the insulator substrates studied in chapters 7 and 8 taking the same deposition times and deposition rates as for the 20 nm thick films on quartz. The thickness has been measured with the same profilometer method described in chapter 5, although being at the limit of resolution. However it can be stated that the thickness was reduced approximately by a factor of two compared to the deposition on quartz resulting in about 10 nm thick films. The reason may be a reduced sticking coefficient of the adsorbing molecules for the first layers. This is remarkable, since the clean gold surface revealed a higher sticking coefficient for C_{60} than quartz [149], which shows that the thiol passivation prevents efficient chemisorption assuring real van-der-Waals bonding of C_{60}.
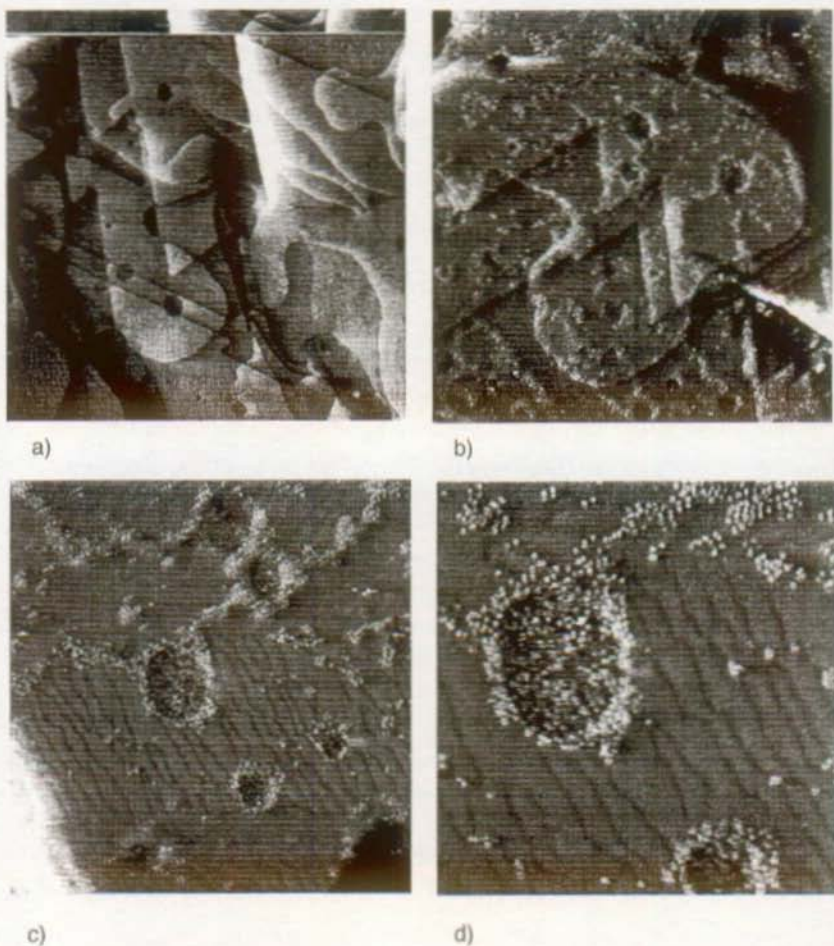
Fig. 9.6: STM image of a decanethiol covered gold surface before (a) and after deposition of less than a monolayer C_{60}. Preferential adsorption sites are etching pits and inhomogeneities in the thiol film like domain boundaries (c), (d). Image sizes: (a) and (b) 300 x 300 nm, (c) 150 x 150 nm, (d) 75 x 75 nm.

9.3 Excitation transfer between adsorbate and substrate

9.3.1 Theory of fluorescence decay time of a molecule in front of a mirror

Since the first reports of the effect of metal surfaces on the lifetime of an oscillating dipole, this phenomenon has been the subject of considerable theoretical and experimental effort. There are several mechanisms through which an electronically excited molecule, viewed as an oscillating dipole, can be influenced by the proximity of a metal surface. For molecules far from the surface (on the order of the wavelength of the dipole emission), the radiation process will be perturbed by the radiation field reflected from the metal. This "image effect" causes the excited state lifetime to decrease, if the reflected field is out of phase with the oscillating dipole, or to increase if it is in phase. In this way the experiment of Drexhage et al. in figure 9.1 can be understood. At smaller molecule-metal separations, additional mechanisms become important. Collective excitations in the metal (if any), such as bulk and surface plasmons, and electron-hole pair excitations, can act as energy acceptors, provided that energy and momentum can both be conserved. The excited molecule can also transfer energy through the field components of its dipole field to the electron gas of the metal, which through various scattering processes, can dissipate the energy into the bulk. This "lossy surface wave" mechanism is very efficient and can shorten the lifetime of an excited molecule by several orders of magnitude.

In the 1970's Chance, Prock, and Silbey et al. (CPS) [150], used the approach of Sommerfeld to solve the Maxwell equations for the boundary conditions of a point dipole above a semi-infinite planar surface of dielectric constant $\varepsilon(\omega)$, and were able to compute the lifetime of a classical dipole as a function of distance from a metal. Their treatment explores both the role of metal dissipative modes and the dependence of the energy transfer rate on the molecule-metal separation. Within this framework, the total decay rate of the excited molecule can be separated into radiative and nonradiative components, the latter representing the rate of energy transfer to the metal.

Following Chance et al. an oscillating dipole near a surface is driven by its own electric field which has been reflected from the interface. The equation of motion for the dipole μ_0 is

$$\ddot{\mu} + b_0\dot{\mu} + \omega^2\mu = \frac{e^2}{m}E_R \qquad (9.1)$$

where ω is the natural oscillation frequency of the undamped dipole, b_0 is the decay rate for the dipole in the absence of a reflecting surface, m is the effective mass of the dipole, and E_R is the reflected electric field at the dipole position. The reflected field will clearly oscillate with the same frequency and lifetime as the driven dipole. If one then assumes a functional form

$$\mu = \mu_0 e^{-i[\omega+\Delta\omega]t}e^{-b/2} \qquad (9.2)$$

94

and

$$E_R = E_0 e^{-i[\omega + \Delta\omega]t} e^{-bt/2} \tag{9.3}$$

and substitutes into the equation of motion, the frequency shift $\Delta\omega$ and the new decay rate b can be calculated. For the cases of interest here, the frequency shift is negligibly small. In terms of the expression for the quantum yield ($q = b_r/b_0$ with b_r being the radiative transfer rate), the normalized decay rate is found to be

$$\hat{b} \equiv \frac{b}{b_0} = 1 + \frac{3q\tilde{\varepsilon}_1}{2\mu_0 k_1^3} \text{Im}(E_0) \tag{9.4}$$

where $\tilde{\varepsilon}_1$ is the dielectric constant of the medium in which the dipole is imbedded, and k_1 is the absolut value of the wave vector in that medium. The calculation of the decay rate of the dipole in the presence of the surface thus becomes a problem of determining the reflected field E_0 at the dipole.

The details of the calculation depend upon the geometry of the dielectric interfaces and dipole orientation, and thus only the general procedure for the solution will be described here. Sommerfeld's treatment calculates the electric field from the Hertz vectors associated with the dipole (i.e. the electrodynamic vector potentials). In order to describe the spatial variation of the field, the dipole field is Fourier analyzed in terms of different wave vector components. In other words, the Hertz vectors are constructed as superposition of eigenfunctions which will produce the spatial variation of the dipole field. Once this superposition has been created, the effect of the reflecting surface on the dipole field can be included by matching the Maxwell boundary conditions for each Fourier (wave vector) component at the interface. The electric field can then be evaluated at the position of the dipole.

The general result for the reflected electric field at the dipole is an integral over all wave vector components of the form

$$E_R = \int_0^\infty \left[B \cdot \mathfrak{R}^p + C \cdot \mathfrak{R}^s \right] e^{-2l_1 \hat{d}_1} \frac{u^3}{l_1} du \tag{9.5}$$

where $\mathfrak{R}^p$ and $\mathfrak{R}^s$ and are the complex Fresnel reflection coefficients for waves polarized parallel to and perpendicular to the plane of incidence, $\hat{d}_1$ is the normalized distance from the dipole to the surface, and $l_1 = -i(1-u^2)^{1/2}$. The coefficients B and C are determined from the geometry and dipole orientation in a specific case. The term in brackets represents the amplitude change and the exponential is the phase change for each wave vector component of the electric field after reflection back to the dipole. Inserting this form for the reflected field into the expression for the decay rate yields:

$$\hat{b} = 1 + Aq \cdot Im \int_0^\infty \left[B \cdot \Re^p + C \cdot \Re^s \right] e^{-2l_1 \hat{d}_1} \frac{u^3}{l_1} du \qquad (9.6)$$

where q is the free molecule quantum yield, and the coefficients A, B, and C for various special cases have been evaluated by Chance et al. [150].

The second term of eq. 9.6 thus describes the modification of the total decay rate of an excited dipole due to its proximity to a surface. The imaginary part of the integrand describes the coupling of the various wave vector components of the dipole field to the decay channel available. As noted by Chance et al., the integral over all wave vector components in eq. 9.6 can be separated into contributions corresponding to the different decay mechanism. This separation can easily be rationalized in terms of a physical picture of the interaction of the dipole field with a surface.

The energy transfer to a metal surface takes place through the "static" and "induction" field of the dipole. The electric field of the dipole again induces a surface charge separation, but here the associated surface dipoles all have wavelengths smaller than that of the radiation field pattern. Thus, these dipole field components which will dissipate energy into the metal through some loss mechanism all have wave vectors greater than the photon wave vector. The integral in eq. 9.6 from $1 < u < \infty$ represents this total energy transfer rate into the metal. If the surface dipole wave vector matches an existing surface plasmon wave vector the dipole field component will transfer energy by exciting this surface charge oscillation, which can propagate far from the dipole position before decaying into bulk excitations. The part for $0 < u < 1$ in the integral 9.6 describes the transfer of energy to the mirror by way of the far field of the dipole and is responsible for the observed oscillations in the transfer rate for large distances. The results are the same as those given previously by Drexhage who used a method based on the far field of the dipole (interference method). This approach involves looking at the interference between the primary ray exiting directly from the dipole and the reflected ray from the mirror. The amplitude that results is converted to intensity and integrated over all angles θ. Thus the interference method gives only the effect of the mirror on the radiative decay-rate constant of the emitter. Finally, the integral expression in 9.6 gives the nonradiative rate constant b_{nr} for energy transfer to the mirror. CPS found that at small d, b_{nr} is proportional to d^{-3} as expected from the dimensionality of the problem. The same result was found by Kuhn using the Förster transfer rate of a dipole in front of a weak absorbing acceptor layer. There are however differences in the case of a strong absorbing mirror, as for example in the energy region of a surface-plasmon absorption. In this case the exact theory of CPS deviates from Kuhns theory. Especially for an infinitely thin absorbing metal layer the energy transfer rate should vary as d^{-4}, as one would expect from simple dimensionality considerations. In the case of quadrupole emitting sources higher order power laws are expected as for the case of an electric quadrupole which follows a d^{-6} law. A magnetic dipole that has a decay rate of d^{-1}, because the electric field falls off as R^{-2}.

9.3.2 Experimental results

All experiments in this chapter have been performed in the same optical geometry as described in chapter 6 for the single crystal. Under an angle of ca. 50° off the surface normal the unfocused pump beam covered an area significantly broader than the probed area on the sample. UV photons at 3.5 eV were used as pump and 1.17 eV photons as probe for the fundamental beam basically being the same geometry as for the previous pump-and-probe experiments in reflection. All measurements were done in saturation of SH quenching at a pump energy density of about 15 μJ/cm^2 .

A list of used thiols for the spacerlayers is given in table 9.1. In the following an abbreviated form indicating the number n of carbon atoms in the chain (including the methyl carbon) is used as related in table 9.1. Figure 9.7 shows the results of the pump-and-probe SHG experiments for different chain lengths (n = 8, 12, 18) of the thiol spacer layer.

n	name	formula	abbreviated form
6	hexanethiol	$CH_3(CH_2)_5SH$	thiol-6
8	octanethiol	$CH_3(CH_2)_7SH$	thiol-8
10	decanethiol	$CH_3(CH_2)_9SH$	thiol-10
12	dodecanethiol	$CH_3(CH_2)_{11}SH$	thiol-12
14	tetradecanethiol	$CH_3(CH_2)_{13}SH$	thiol-14
16	hexadecanethiol	$CH_3(CH_2)_{15}SH$	thiol-16
18	octadecanethiol	$CH_3(CH_2)_{17}SH$	thiol-18

Table 9.1: Names of straight-chain n-alkanethiols, $CH_3(CH_2)_{n-1}SH$ used here.
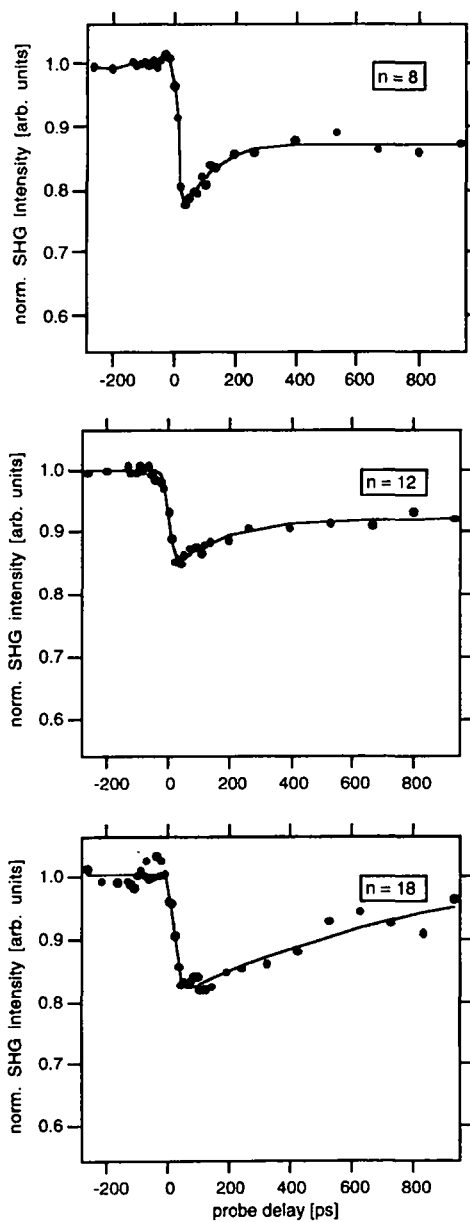
Fig. 9.7: Normalized pump-and-probe SH signal of a C_{60} film on top of thiol covered gold for different chain lengths (see text).

The interface state appears as for the thin films on insulating substrates (see chapter 8). A second component with long lifetime is also present due to the extended film thickness of about ten monolayers. This second-harmonic signal can be suppressed by approximately 20% at saturation pump energy of 15 $\mu J/cm^2$. The short lifetime interface state reduces the second-harmonic signal by ca. 15%. Neither the efficiency of the long living nor of the short living component varies with the chain length of the spacer molecules as can be seen from figure 9.8. These values can not be directly compared to the preceding measurements of the C_{60} single crystal and thin films since the gold surface gives also an additional strong second-harmonic signal. However, in the pump-and-probe experiments the relative signal change is measured. In order to analyze the source of the SH signal and its transient change a control experiment has been performed: After the typical pump-and-probe experiment in which the short lived state was apparent, the fullerene layer has been washed off by rinsing the sample with chloroform. In the following pump-and-probe experiment the signal stayed unchanged by the pump beam. Since the second harmonic signal from gold is still present any misalignment after rinsing can be ruled out by this procedure. By the way, the possibility to wash off the film demonstrates that no polymeric structures were created. In figure 9.7 fits according to the model from chapter 8 are shown. They give lifetimes of 87 ps, 185 ps and 517 ps for n = 8, 12 and 18. Such an evaluation has been employed for all spacer layers (n = 6 to n = 18).
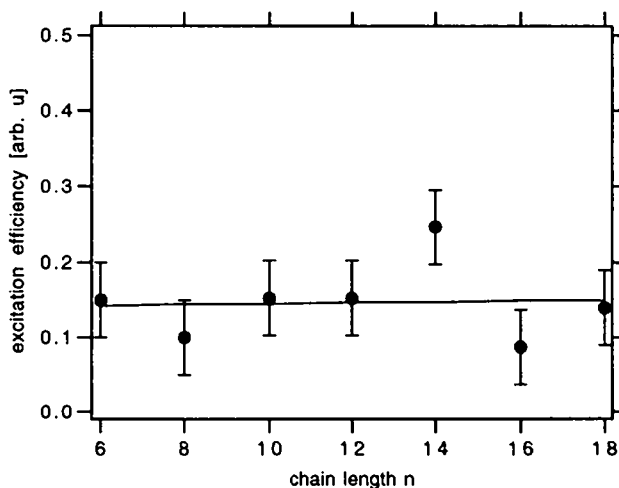

Fig. 9.8: Excitation efficiency for the short lived interface state for different chain length of the thiol molecules. In the limit of experimental resolution the efficiency stays constant in the measured region.
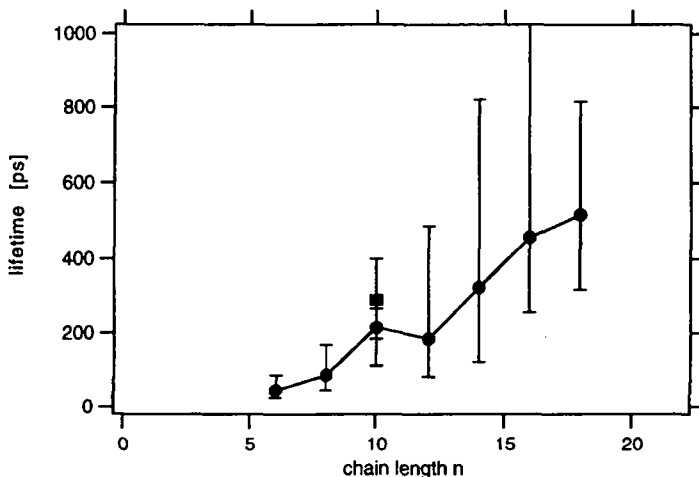
Fig. 9.9: Lifetime of the interface state in the C_{60} film near the gold surface measured by pump-and-probe second-harmonic generation for different chain length n (dots). For n = 10 the lifetime for a silver substrate (square) has been added from the measurement of fig 9.10.

Figure 9.9 shows the distance dependence of the excitation lifetime which decreases monotonously with shorter thiol chains. To compare the effect with a different metal surface C_{60} has been deposited on a decanethiol covered silver surface. The fitted lifetime from this measurement shown in figure 9.10b, is included in this series. The lifetime stayed in the range of the experiments with gold. This is noteworthy since silver exhibits a large surface plasmon absorption in the range of the pump frequency [151]. The unchanged behavior of C_{60} for silver rules out a plasmon related effect. The dots in figure 9.9 are the mean values of several (5 - 15) individual measurements on different spots on the sample. The error bars do not represent the error of this mean value but indicate typical deviations of the fits for the individual measurements.

A qualitative deviation from the typical behavior has been found for C_{60} on the shortest studied chain length, the hexane thiol. Using the same deposition parameters (T = 140°C) as for the other thiol covered gold substrates a qualitatively different result of the pump-and-probe experiments was obtained. As can be seen in figure 9.11b the normalized SHG signal does not decrease, but shows an enhancement of signal. Moreover, for negative delay times the normalized signal does not reach unity, which indicates an extremely long living state in the range of microseconds or even seconds. In a separate preparation with deposition of C_{60} at 20°C substrate temperature the usual behavior is seen (fig. 9.11a).
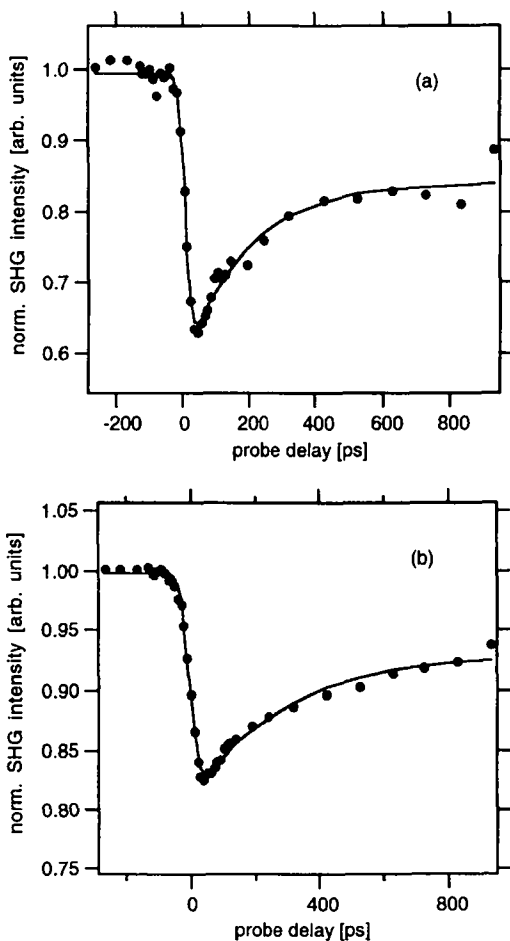
Fig. 9.10: Normalized pump-and-probe signal of a C_{60} film on a gold substrate (a) and a silver substrate (b) with a spacer layer of decanethiol. The fitted line gives lifetimes of 217 ps and 284 ps, resp.

A possible explanation of the significantly different behavior may be found in the penetration of C_{60} into the thiol layer which leads to a substantially enhanced coupling probably even to charge transfer. The change of sign in the short lived component can be understood by a phase shift (see chapter 4) between the SH amplitude created by C_{60} and the amplitude created at the gold surface with respect to the case of C_{60} separated from gold by the thiol layer.

An additional experiment of aC_{60} film (ca. 25 nm thickness) directly evaporated onto the bare

gold substrate is shown in figure 9.11c. The interface state has vanished completely and two long lived components are observed. One is an extremely long lived state ($\tau > 50$ ms) as described above. The second state resembles the one observed for the C_{60} crystals but with a phase inversion. These two observations, long lived component and phase inversion of the undisturbed C_{60} signal, demonstrate the similarity between the measurements of figures 9.11b and 9.11c. This similarity supports the assumption that C_{60} diffusion into the thiol layer has occurred in the measurement of figure 9.11b. A conclusive explanation for the creation of the extremely long lived component or an assignment to charge transfer can, however, not be given in the present stage.

C_{60} directly adsorbed on noble metal surfaces is known to interact strongly [54], [152], [153], [154]. The experiment with C_{60} on the hexanethiol spacer suggests that we observed the difference between C_{60} in direct contact with the electronic system of the metal and molecules only slightly perturbed by the metal surface. It is very likely that the hexanethiol layer is disordered due to the elevated temperature treatment and that thiol molecules have even been desorbed. However, the experiment with the cold substrate during deposition of the fullerenes shows evidently the passivating function of an even short thiol layer and supports the picture of an ordered structure at room temperature which is impenetrable for adsorbed species (as STM indicates as well) [116]. This picture is in contrast to conclusions drawn from wetting measurements. The complete disappearance of the short lived state in direct contact with the metal can have two reasons. Either the state has disappeared in reality due to the strong metal-C_{60} charge transfer or it lives on a time scale inaccessible to our picosecond laser system. The interaction of C_{60} films with the substrate is restricted to the very first layer [153, 154] where for example charge transfer between the metal and C_{60} creates a metallic character of the interface molecules. Since all short lived features disappear upon direct contact with gold it can be concluded that the excitation transfer takes place only between the very first molecular layer and the metal substrate. The second layer may also contribute to the excitation transfer, but probably does not generate a SH signal. So in a simple model of the experimental system only the immediate interface area has to be taken into account (Fig. 9.12). Contributions of the surface/vacuum interface are included in the long-living state whose distance to the gold substrate does not change much with thiol length d due to the larger film thickness D.
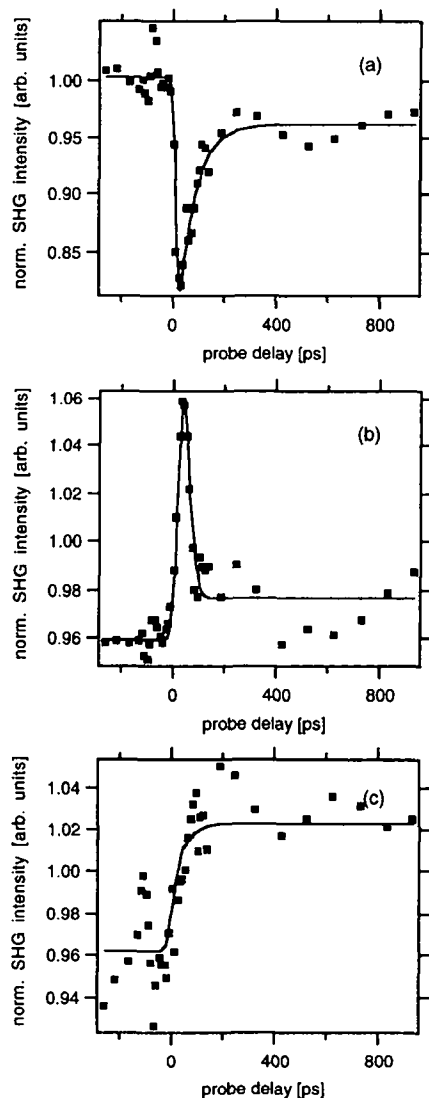
Fig. 9.11: Normalized pump-and-probe SH signals for a C_{60} film (10 nm) close to the metal surface separated by hexanethiol (a) and (b), and for a film (25 nm) in direct contact with the gold substrate (c). The difference between (a) and (b) is the substrate temperature during deposition of the C_{60} film, 85°C and 23°C, respectively. In (a) the fit to the model results in a lifetime of 62 ps.

9.3.3 Discussion

Gold surfaces are known to give a strong second-harmonic signal, which is attenuated by the thiol adsorption by ca. 40% for the fundamental frequency at 1.17 eV (1064 nm) for polycrystalline gold substrates [15]. In a frequency dependent SHG study it was shown that the phase of the second-harmonic response of this system does not play a role in this energy range. So the nonlinear optical susceptibilities can be assumed to be real, which is not obvious since gold nanoparticles were found to show small absorption at 2.34 eV (532 nm) due to a surface plasmon [155]. Nevertheless it is reasonable to believe that the surface plasmon does not survive the adsorption of thiols. The comparison between two different metal substrates can give further information about the role of the substrate. Silver is known to show a strong plasmon resonance in the energy region of 3.5 eV [151] which is not present in the case of gold. The fact that the two materials show the same influence on the excitation in the underlying film shows that the pump pulses act primarily on the C_{60} molecules and do not effect the substrate. As mentioned before no pump-and-probe effect was observed, when the C_{60} layer was removed. Thus it can be assumed that also the alkyl chain covered gold surface does not contribute to the pump-and-probe SHG experiment on C_{60}.
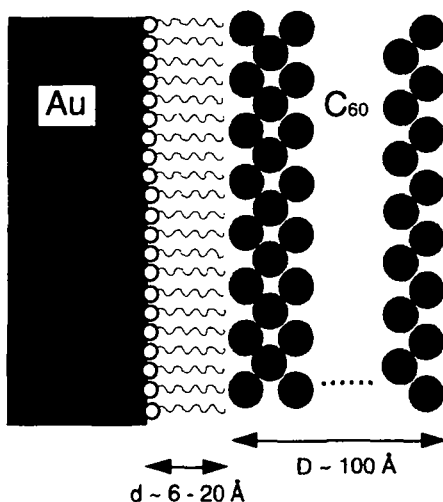

Fig. 9.12: Schematic model of the C_{60}/thiol/Au sandwich structure

The ellipsometric data from figure 9.5 can be taken to plot the rate of excitation transfer, which is inversely proportional to the lifetime, against the distance of the excited layer to the metal surface. The ellipsometry measurements of Porter et al. [135] found for each methylene chain a length of 1.5 Å and for the methylthiol (-S-CH$_3$) a length of 3.8 Å. The hypothetical values are

calculated with covalent bonds and van-der-Waals radii for a film in which the thiol molecules perpendicularly arranged on the surface are 1.3 Å and 5.6 Å. respectively. If an average tilt of 25° is introduced into this model the values change to 1.1 Å and 5.1 Å. The latter values were used to calculate the distance to the metal substrate in figure 9.13 since the inclination of the molecules has been further supported by other techniques like IR spectroscopy [142].

The experimental data points in figure 9.13 were fitted to different models of excitation transfer. One possible mechanism for the excitation transfer is the well-known case considered by Förster for a single acceptor molecule [156]. In the present case this would be equivalent to the interaction of the exciton dipole moment with a localized dipole moment in the metal substrate. Considering only electric fields the well-known d^{-6} law for two interacting dipoles can be found as discussed before. Evidently this law does not fit at all to the measured data as indicated by the dash-dotted line in figure 9.13. In order to account for the 3-dim. acceptor material the decay rate has to be integrated over the half space of the metal substrate resulting in a d^{-3} behavior. Higher quadrupole terms increase the power law exponent.
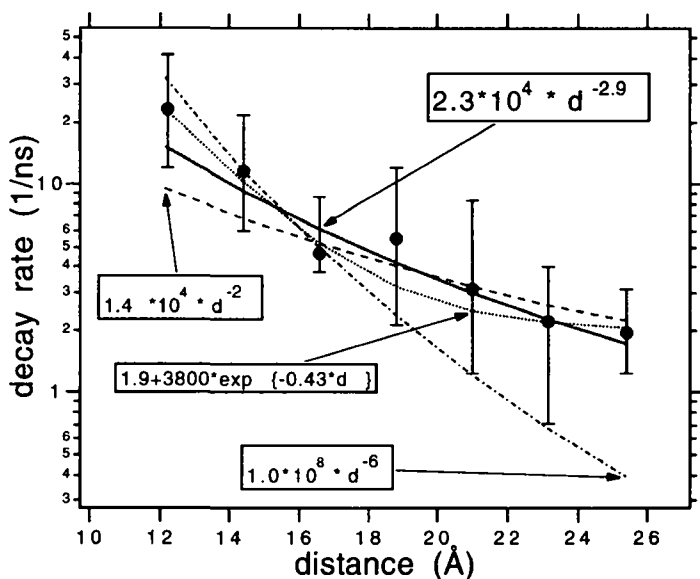

Fig. 9.13: Experimentally measured decay rates of the interface state from figure 9.9 versus distance to the gold substrate. The data has been fitted to polynomial functions of different order as indicated and to the function of eq. (9.7). A three-parameter fit by an exponential function is included (dotted curve).

CPS discussed the contributions from magnetic dipoles in this geometry [150], which results in a d^{-1} law. Taking the exponents as additional fit parameter the following dependence can be found

$$n(d) = A \cdot d^\gamma \tag{9.7}$$

with $A = 2.3 \ 10^4$ 1/ns and $\gamma = -2.9$, which coincides very well to the radiationless excitation transfer of Kuhns theory for a system of dipoles interacting with an infinitely weakly absorbing acceptor layer and the exact theory of CPS for a dipole interaction with a bulk metal surface.

Kuhn et al. found in a different experiment the fluorescence decay of an organic dye quenched by viologen and separated by LB layers of different chain length to be exponential in the range of 20 - 30 Å [157]. The data presented here, covering nearly the same distance region, can also be well fitted by an exponential behavior as illustrated by the dotted line in figure 9.13. However, this is not surprising since a third fitting parameter is included in the fitting formula. In a two parameter fit without constant term the fit is much worse at long distances. Alivisatos et al. [124] found for biacetyl separated by NH_3 from Ag(111) a deviation from the d^{-3} behavior for thicknesses from 28 to 457 Å. They explained this in the CPS scheme as energy transfer to electrons localized at the metal surface. Rossetti et al. [121] found for pyrazine deposited on argon/polycrystalline silver the d^{-3} behavior for distances down to 125 Å. For thinner spacer layers they found a constant transfer rate. They observed as well a double exponential behavior in their decay rate for distances below 400 Å that they attributed to surface roughness and/or surface contamination, which is an inherent difficulty of the experiment, since they had to work at 4 K. Our experiment covering the most interesting range of spacing (10 - 30 Å) demonstrates that the d^{-3} behavior found by Vaubel et al [123] extends to even shorter distances. The results do not exhibit the deviation as observed by Rossetti et al.

For even smaller distances tunneling must become an important decay channel for the excitons. Since the tunneling current is directly proportional to the transition probability between resonant states [158] the analytical form will not be a mere exponential function but of the form

$$J_T \propto d^{-1} \cdot \exp(-Ad) \tag{9.8}$$

So for very small distances the inverse to the distance term should dominate the tunneling process. The transition from the energy transfer mechanism to tunneling processes will be difficult to determine. For distances smaller than 2.5 Å, where tunneling becomes important local-field effects in the linear and nonlinear optical properties of adsorbed molecules complicate the interpretation of optical experiments [159].

10. Outlook

Second-harmonic generation was applied to the investigation of chemical and physical processes at surfaces and interfaces for two semiconducting systems. One of which is of major technological importance already, the other maybe in the future.

Using a ps pulsed laser system the dynamics of excited state at surfaces and interfaces are studied. The pump-and SHG probe method by the interference grating technique can be extended to study in detail transport processes of the electronic excitation in the C_{60} crystal.

Energy transfer from an adsorbed molecular system to the underlying substrate has been studied for one particular sandwich structure. The current experiments can be further extended to cover a larger range of distances between the excited C_{60} molecules and the metal substrate. Shorter distances can also be realized, however, in these cases there are still uncertainties about the structure of the organic spacer layer. Up to now hexanethiol was assumed not to build a compact structure according to ellipsometry measurements as mentioned above. The success of the pump-and-probe second-harmonic generation experiment indicates that this is probably not the case. This gives hope to proceed the experiments with this kind of spacer layer also for shorter distances. Here, probably, sub-picosecond resolution will be necessary. Larger distances can be covered by multilayer growth with other self assembly thiols. Investigation into another direction might be the use of different functional end groups of the thiol molecules. This will give insight into the chemical bonding of adsorbates to the functional group. Furthermore other substrates than metals can be used like e. g. semiconductors. Here, it may be very interesting to study the second-harmonic response for different photon energies with special emphasis on resonance effects between substrate and adsorbate states.

11. References

[1] D. A. Long, *Raman spectroscopy* (McGraw Hill, New York, 1977).

[2] A. Zangwill, *Physics at surfaces* (Cambridge university press, Cambridge, 1988).

[3] P. N. Butcher and D. Cotter, *The Elements of Nonlinear Optics* (Cambridge University Press, Cambridge, 1991).

[4] C. Flytzanis,"Theory of Nonlinear Optical Susceptibilities", in *Quantum Electronics: A Treatise* , 1, H. Rabin and C. L. Tang, Eds. (Academic Press, New York, 1975), .

[5] N. Bloemberge,"General Introduction", in *Quantum Electronics: A Treatise* , I, H. Rabin and C. L. Tang, Eds. (Academic Press, New York, 1975), .

[6] H.-J. Krause, "Nichtlineare optische Spektroskopie an Grenzflächen", Ph.D thesis, Aachen, 1994.

[7] Y. R. Shen, *The Principles of Nonlinear Optics* (John Wiley & Sons, New York, 1984).

[8] F. Zernicke, J. Opt. Soc. Am. **54**, 1215 (1964).

[9] A. Yariv and P. Yeh, *Optical waves in crystals, propagation and control of laser radiation* (Wiley and Sons, New York, 1984).

[10] V. G. Dmitriev, G. G. Gurzadyan and D. N. Nikogosyan, *Handbook of Nonlinear Optical Crystals* (Springer, Berlin, 1991).

[11] J. A. Giordmaine and R. C. Miller, Phys. Rev. Lett. **14**, 973 (1965).

[12] R. B. Hall, J. N. Russel, J. Miragliotta and P. R. Rabinowitz,"Studies of Bonding and Reaction on Metal Surfaces Using Second-Harmonic and Sum-Frequency Generation", in *Chemistry and Physics of Solid Surfaces VIII* , 22, R. Vanselow and R. Howe, Eds. (Springer, Berlin, 1990), .

[13] Y. R. Shen, Ann. Rev. Mater. Sci. **16**, 69 (1986).

[14] G. L. Richmond, J. M. Robinson and Y. L. Shannon, Prog. Surf. Sci. **28**, 1 (1988).

[15] F. Eisert, "Untersuchung selbstorganisierender Monolagen mit optischer Frequenzverdopplung (SHG)", Ph.D thesis, Heidelberg, 1993.

[16] G. A. Reider, U. Höfer and T. F. Heinz, Phys. Rev. Lett. **66**, 1994 (1991).

[17] N. Bloembergen and P. S. Pershan, Phys. Rev. **128**, 606 (1962).

[18] T. Stehlin, M. Feller, P. Guyot-Sionnest and Y. R. Shen, Opt. Lett. **13**, 389 (1988).

[19] T. F. Heinz, M. M. T. Loy and W. A. Thompson, Phys. Rev. Lett. **54**, 63 (1985).

[20] Y. Tang, L. J. Simpson and T. E. Furtak, Phys. Rev. Lett. **67**, 2814 (1991).

[21] B. Pettinger, J. Lipkowski, S. Mirwald and A. Friedrich, J. Electroanal. Chem **329**, 289 (1992).

[22] C. H. Lee, R. K. Chang and N. Bleombergen, Phys. Rev. Lett. **18**, 167 (1967).

[23] D. Guidotti, T. A. Driscoll and H. J. Gerritsen, Solid State Commun. **46**, 337 (1983).

[24] H. W. K. Tom, T. F. Heinz and Y. R. Shen, Phys. Rev. Lett. **51**, 1983 (1983).

[25] J. A. Litwin, J. E. Sipe and H. M. v. Driel, Phys. Rev. B **31**, 5543 (1985).

[26] W. Daum, H.-J. Krause, U. Reichel and H. Ibach, Phys. Rev. Lett. **71**, 1234 (1993).

[27] G. Lüpke, D. J. Bottomley and H. M. v. Driel, Phys. Rev. B **47**, 10389 (1993).

[28] J. I. Dadap, B. Doris, Q. Deng, M. C. Downer, J. K. Lowell and A. C. Diebold, Appl. Phys. Lett. **64**, 2139 (1994).

[29] A. Yariv, *Optical Electronics* (Saunders College Publishing, Philadelphia, 1991).

[30] H. J. Krause and W. Daum, Appl. Phys. Lett. **60**, 2180 (1992).

[31] H.-J. Krause and W. Daum, Appl. Phys. B **56**, 123 (1993).

[32] G. J. Pietsch, Appl. Phys. A **60**, 347 (1995).

[33] Y. J. Chabal, A. L. Harris, K. Raghavachari and J. C. Tully, Int. J. Mod. Phys. B **7**, 1031 (1993).

[34] P. Guyot-Sionnest, P. Dumas, Y. J. Chabal and G. S. Higashi, Phys. Rev. Lett. **64**, 2156 (1990).

[35] P. Jakob, P. Dumas and Y. J. Chabal, Appl. Phys. Lett. **59**, 2968 (1991).

[36] E. H. Poindexter, Semicond. Sci. Technol. **4**, 961 (1989).

[37] C. R. Helms and B. E. Deal, *The Physics and Chemistry of the Si-SiO$_2$ Interface"* (Plenum Press, New York, 1988).

[38] S. A. Akhmanov, N. I. Koroteev and I. L. Shumay, *Nonlinear Optical Diagnostics of Laser-Excited Semiconductor Surfaces* (Harwood academic publisher, chur, 1989).

[39] E. H. Nicollian and J. R. Brews, *MOS Physics and Technology* (Wiley and Sons, New York, 1983).

[40] E. H. Poindexter and P. J. Caplan, J. Vac. Sci. Technol. A **6**, 1352 (1988).

[41] C. Herring and N. M. Johnson,"Hydrogen Migration and Solubility in Silicon", in *Hydrogen in Semiconductors* , 34, J. I. Pankove and N. M. Johnson, Eds. (Academic Press, Boston, 1991), pp. 225.

[42] F. J. Himpsel, F. R. McFeely, A. Taleb-Ibrahimi, J. A. Yarmoff and G. Hollinger,"Microscopic Structure of the SiO_2/Si Interface", in *The Physics and Chemistry of SiO_2 and the Si-SiO_2 Interface* , 1, B. E. D. C. R. Helms, Eds. (Plenum Press, New York, 1988), pp. 219.

[43] D. Jost, W. Lüthy, H. P. Weber and R. P. Salathé, Appl. Phys. Lett. **49**, 625 (1986).

[44] J. L. Daschbach, P. R. Fischer, D. E. Gragson, D. Demarest and G. L. Richmond, J. Phys. Chem. **99**, 3240 (1995).

[45] L. L. Kulyuk, D. A. Shutov, E. E. Strumban and O. A. Aktsipetrov, J. Opt. Soc. Am. B **8**, 1766 (1991).

[46] C. H. Bjorkman, C. E. Shearon, Y. Ma, T. Yasuda, G. Lucovsky, U. Emmerichs, C. Meyer, K. Seo and H. Kurz, J. Vac. Sci. Technol. A **11**, 964 (1993).

[47] C. H. Bjorkman, T. Yasuda, C. E. Shearon, Y. Ma, G. Lucovsky, U. Emmerichs, C. Meyer, K. Leo and H. Kurz, J. Vac. Sci. Technol. B **11**, 1521 (1993).

[48] J. T. Fitch, C. H. Bjorkman, G. Lucovsky, F. H. Pollak and X. Yin, J. Vac. Sci. Technol. B **7**, 775 (1989).

[49] S. V. Govorkov, V. I. Emel'yanov, N. I. Koroteev, G. I. Petrov, I. L. Shumai and V. V. Yakolev, Sov. Phys. Tech. Phys. **34**, 56 (1989).

[50] S. V. Govorkov, N. I. Koroteev, G. I. Petrov, I. L. Shumay and V. V. Yakovlev, Appl. Phys. A **50**, 440 (1990).

[51] A. Y. Abdullaev, S. V. Govorkov, P. K. Kashkarov, N. I. Koroteev, G. I. Petrov and I. L. Shumai, Sov. Phys. Solid State **29**, 1094 (1987).

[52] P. R. Fischer, J. L. Daschbach, D. E. Gragson and G. L. Richmond, J. Vac. Sci.

Technol. A **12**, 2617 (1994).

[53] J. H. Weaver and D. M. Poirier, Eds. *Solid state Properties of Fullerenes and Fullerene-based Materials, Solid State Physics*, vol. 48, F. S. H. Ehrenreich, Eds. (Academic Press, New York, 1994).

[54] S. J. Chase, W. S. Bacsa, M. G. Mitch, L. J. Pilione and J. S. Lannin, Phys. Rev. B **46**, 7873 (1992).

[55] G. Gensterblum, L.-M. Yu, J.-J. Pireaux, P. A. Thiry, R. Caudano, J.-M. Themlin, S. Bouzidi and F. Coletti, Appl. Phys. A **56**, 175 (1993).

[56] K. Tanigaki, S. Kuroshima and T. W. Ebbesen, Thin Solid Films **257**, 154 (1995).

[57] w. Krakow, N. M. Rivera, R. A. Roy, R. S. Ruoff and J. J. Cuomo, Appl. Phys. A **56**, 185 (1993).

[58] J. Z. Liu, J. W. Dykes, M. D. Lan, P. Klavins, R. N. Shelton and M. M. Olmstead, Appl. Phys. Lett. **62**, 531 (1993).

[59] M. A. Verheijen, C. W. v. Hasselt and T. Rasing, Surf. Sci. **251/252**, 467 (1991).

[60] A. F. Hebard, R. C. Haddon, R. M. Fleming and A. R. Kortan, Appl. Phys. Lett. **59**, 2109 (1991).

[61] W. Krätschmer, L. D. Lamb, K. Fostiropoulos and D. R. Huffman, Nature **347**, 354 (1990).

[62] A. F. Hebard, O. Zhou, Q. Zhong, R. M. Fleming and R. C. Haddon, Thin Solid Films **257**, 147 (1995).

[63] C. Pan, M. P. Sampson, Y. Chai, R. H. Hauge and J. L. Margrave, J. Phys. Chem. **95**, 2994 (1991).

[64] J. Abrefah, D. R. Olander, M. Balooch and W. J. Siekhaus, Appl. Phys. Lett. **60**, 1313 (1992).

[65] R. A. Jishi, M. S. Dresselhaus, G. Dresselhaus, K. A. Wang, P. Zhou, A. M. Rao and P. C. Eklund, Chem. Phys. Lett. **206**, 187 (1993).

[66] K.-A. Wang, A. M. Rao, P. C. Eklund, M. S. Dresselhaus and G. Dresselhaus, Phys. Rev. B **48**, 11375 (1993).

[67] A. M. Rao, *et al.*, Science **259**, 955 (1993).

[68] P. Zhou, *et al.*, Appl. Phys. Lett. **60**, 2871 (1992).

[69] P. C. Eklund, A. M. Rao, P. Zhou, Y. Wang, K. Wang, G. T. Hager and J. M. Holden, Mat. Sci. Eng. B **19**, 154 (1993).

[70] P. C. Eklund, A. M. Rao, P. Zhou, Y. Wang and J. M. Holden, Thin Solid Films **257**, 185 (1995).

[71] D. Wilk, D. Johannsmann, C. Stanners and Y. R. Shen, Phys. Rev. B **51**, 10057 (1995).

[72] G. Gu, W. Zhang, H. Zen, Y. Du, Y. Han, W. Zhang, F. Dong and Y. Xia, J. Phys. B At. Mol. Opt. Phys. **26**, L451 (1993).

[73] D. G. McLean, R. L. Sutherland, M.'C. Brant, D. M. Brandelik, P. A. Fleitz and T. Pottenger, Opt. Lett. **18**, 858 (1993).

[74] C. Li, L. Zhang, R. Wang, Y. Song and Y. Wang, J. Opt. Soc. Am. B **11**, 1356 (1994).

[75] S. D. Brorson, M. K. Kelly, U. Wenschuh, R. Buhleier and J. Kuhl, Phys. Rev. B **46**, 7329 (1992).

[76] W. J. Blau, H. J. Byrne, D. J. Cardin, T. J. Dennis, J. P. Hare, H. W. Kroto, R. Taylor and D. R. M. Walton, Phys. Rev. Lett. **67**, 1423 (1991).

[77] H. Hoshi, N. Nakamura, Y. Maruyama, T. Nakagawa, S. Suzuki, H. Shiromaru and Q. Achiba, Jpn. J. Appl. Phys. A **30**, L1397 (1991).

[78] X. K. Wang, T. G. Zhang, W. P. Lin, S. Z. Liu, G. K. Wong, M. M. Kappes, R. P. H. Chang and J. B. Ketterson, Appl. Phys. Lett. **60**, 810 (1992).

[79] B. Koopmans, A.-M. Janner, H. T. Jonkman, G. A. Sawatzky and F. v. d. Woude, Phys. Rev. Lett. **71**, 3569 (1993).

[80] B. Koopmans, A. Anema, H. T. Jonkman, G. A. Sawatzky and F. v. d. Woude, Phys. Rev. B **48**, 2759 (1993).

[81] J. R. Heflin, D. C. Rodenberger, R. F. Shi, M. Wu, N. Q. Wang, Y. M. Cai and A. F. Garito, Phys. Rev. A **45**, R4233 (1992).

[82] K. B. Eisenthal, Annu. Rev. Phys. Chem. **43**, 627 (1992).

[83] S. A. Akhmanov, N. I. Koroteev, G. A. Paitia, I. L. Shumay, M. F. Galjautdinov, I. B. Khaibullin and E. I. Shtyrkov, J. Opt. Soc. Am. B **2**, 283 (1985).

[84] E. V. Sitzmann and K. B. Eisenthal, J. Phys. Chem. **92**, 4579 (1988).

[85] P. Guyot-Sionnest, J. El. Spec. Rel. Phen. **64**, 1 (1993).

[86] M. K. Kelly, P. Etchegoin, D. Fuchs, W. Krätschmer and F. Fostiropoulos, Phys. Rev. B **46**, 4963 (1992).

[87] S. L. Ren, *et al.*, Appl. Phys. Lett. **59**, 2678 (1991).

[88] F. Li, J. Song, S. Qian and Y. Li, in Proc. of *SPIE* , Z. H. Kafafi, Eds. (SPIE, San Diego, 1994), .

[89] T. W. Ebbesen, T. N. Thomas, R. A. Taylor, J. F. Ryan, D. Mihailovic and R. Zamboni, Europhys. Lett. **25**, 403 (1994).

[90] S. Saito and A. Oshiyama, Phys. Rev. Lett. **66**, 2637 (1991).

[91] R. W. Lof, M. A. v. Veenendaal, B. Koopmans, H. T. Jonkman and G. A. Sawatzky, Phys. Rev. Lett. **68**, 3924 (1992).

[92] S. G. Louie, in *Progress in Fullerene Research* H. Kuzmany, J. Fink, M. Mehring and S. Roth, Eds. (World Scientific, Kirchberg, 1994), .

[93] J.-M. Themlin, S. Bouzidi, F. Coletti, J.-M. Debever, G. Gensterblum, L.-M. Yu, J.-J. Pireaux and P. A. Thiry, Phys. Rev. B **46**, 15602 (1992).

[94] G. Gensterblum, J. J. Pireaux, P. A. Thiry, R. Caudano, J. P. Vigneron, P. Lambin and A. A. Lucas, Phys. Rev. Lett. **67**, 2171 (1991).

[95] R. Zamboni, M. Muccini, R. Danieli, C. Taliani, H. Mohn, W. Müller and H. U. t. Meer, in Proc. of *SPIE* , Z. H. Kafafi, Eds. San Diego, 1994), pp. 120.

[96] T. W. Ebbesen, T. Tanigaki and S. Kuroshima, Chem. Phys. Lett. **181**, 501 (1991).

[97] R. V. Bensasson, T. Hill, C. Lambert, E. J. Land, S. Leach and T. G. Truscott, Chem. Phys. Lett. **201**, 326 (1993).

[98] Y. Zeng, L. Biczok and H. Linschitz, J. Phys. Chem. **96**, 5237 (1992).

[99] M. R. Wasielewski, M. P. O'Neil, K. R. Lykke, M. J. Pellin and D. M. Gruen, J. Am. Chem. Soc. **113**, 2774 (1991).

[100] J. W. Arbogast, A. P. Darmanyan, C. S. Foote, Y. Rubin, F. N. Diederich, M. M. Alvarez, S. J. Anz and R. L. Whetten, J. Phys. Chem. **95**, 11 (1991).

[101] T. Tsubo and K. Nasu, Solid State Commun. **91**, 907 (1994).

[102] P. J. Bounds and W. Siebrand, Chem. Phys. Lett. **75**, 414 (1980).

[103] A.-M. Janner, B. Koopmans, H. T. Jonkman and G. A. Sawatzky,"Exciton propagation studied by temperature dependent optical second-harmonic generation from C_{60} films", in *Physics and Chemistry of Fullerenes and Derivatives* , H. Kuzmany, J. Fink, M. Mehring and S. Roth, Eds. (World Science, New Aork, 1995), pp. 234.

[104] M. Manfredini and P. Milani, Appl. Phys. Lett. **66**, 153 (1995).

[105] S. Henke, K. H. Thürer, S. Geier, B. Rauschenbach and B. Stritzker, Appl. Phys. A **60**, 383 (1995).

[106] H. J. Byrne, L. Akselrod, C. Thomsen, A. Mittelbach and S. Roth, Chem. Phys. Lett. **204**, 461 (1993).

[107] A. Skumanich, Chem. Phys. Lett. **182**, 486 (1991).

[108] B. Mann, J. Appl. Phys. **42**, 4393 (1971).

[109] A. A. Villaeys and J. C. Vallet, Phys. Rev. A **41**, 2796 (1990).

[110] S. H. Lin, R. G. Alden, A. A. Villaeys and V. Pflumio, Phys. Rev. A **48**, 3137 (1993).

[111] T. F. Heinz, C. K. Chen, D. Ricard and Y. R. Shen, Phys. Rev. Lett. **48**, 478 (1982).

[112] A. A. Villaeys, V. Pflumio and S. H. Lin, Phys. Rev. A **49**, 4996 (1994).

[113] A. Yariv, *Quantum electronics* (John Wiley & Sons, New York, 1989).

[114] T. Suzuki and T. F. Heinz, Opt. Lett. **14**, 1201 (1989).

[115] X. D. Zhu, T. Rasing and Y. R. Shen, Phys. Rev. Lett. **61**, 2883 (1988).

[116] A. Hirstein, personal communication.

[117] X. K. Wang, T. G. Zhang, P. M. Lundquist, W. P. Lin, Z. Y. Xu, G. K. Wong, J. B. Ketterson and R. P. H. Chang, Thin Solid Films **257**, 244 (1995).

[118] F. F. So and S. R. Forrest, Phys. Rev. Lett. **66**, 2649 (1991).

[119] K. H. Drexhage, Eds. *Interaction of light with monomolecular dye layers*, *Progress in optics*, vol. 12, E. Wolf, Eds. (North-Holland, Amsterdam, 1974).

[120] M. Cho and R. J. Silbey, Chem. Phys. Lett. **242**, 291 (1995).

[121] R. Rossetti and L. E. Brus, J. Chem. Phys. **73**, (1980).

[122] A. Sommerfeld, Ann. Phys. Leipz. **28**, 665 (1909).

[123] G. Vaubel, H. Baessler and D. Möbius, Chem. Phys. Lett. **10**, 334 (1971).

[124] A. P. Alivisatos, D. H. Waldeck and C. B. Harris, J. Chem. Phys. **82**, 541 (1985).

[125] H. Rieley, N. J. Price, R. G. White, R. I. R. Blyth and A. W. Robinson, Surf. Sci. **331**, 189 (1995).

[126] R. C. Tiberio, H. G. Craighead, M. Lercel and T. Lau, Appl. Phys. Lett. **62**, 476 (1993).

[127] O. Cavalleri, personal communication.

[128] K. Bammel, J. Ellis and H.-G. Rubahn, Chem. Phys. Lett. **201**, 101 (1993).

[129] E. Tosatti,"The physics of tip-surface approaching: Speculations and open issues", in *Highlights in Condensed Matter Physics and Future Prpspects* , 285, L. Esaki, Eds. (Plenum Press, New York, 1991), pp. 631.

[130] T. Dittrich and P. Hänggi, Phys. Bl. **51**, 957 (1995).

[131] W. Haiss, D. Lackey, J. K. Sass and K. H. Besocke, J. Chem. Phys. **95**, 2193 (1991).

[132] M. Hegner, P. Wagner and G. Semenza, Surf. Sci. **291**, 39 (1993).

[133] S. Buchholz, H. Fuchs and J. P. Rabe, J. Vac. Sci. Technol. A **15**, 5433 (1991).

[134] M. Buck, M. Grunze, F. Eisert, J. Fischer and F. Träger, J. Vac. Sci. Technol. A **10**, (1992).

[135] M. D. Porter, T. B. Bright, D. L. Allara and C. E. D. Chidsey, J. Am. Chem. Soc. **109**, 3559 (1987).

[136] A. Ulman, *An Introduction to Ultrathin Organic Films* (Academic Press, Inc., Boston, 1991).

[137] K. Edinger, A. Gölzhäuser, K. Demota, C. Wöll and M. Grunze, Langmuir **9**, 4 (1993).

[138] R. Becker, unpublished results (1996).

[139] G. Hähner, C. Wöll, M. Buck and M. Grunze, Langmuir **9**, 1955 (1993).

[140] C. D. Bain, E. B. Troughton, Y.-T. Tao, J. Evall, G. M. Whitesides and R. G. Nuzzo,

J. Am. Chem. Soc. **111**, 321 (1989).

[141] S. D. Evans and A. Ulman, Chem. Phys. Lett. **170**, 462 (1990).

[142] R. G. Nuzzo, L. H. Dubois and D. L. Allara, J. Am. Chem. Soc. **112**, 558 (1990).

[143] C. Naselli, J. F. Rabolt and J. D. Swalen, J. Chem. Phys. **82**, 2136 (1985).

[144] O. Cavalleri, A. Hirstein and K. Kern, Surf. Sci. **360**, L960 (1995).

[145] A. R. Knight,"Photochemistry of thiols", in *The chemistry of the thiol group* , 1, S. Patai, Eds. (John Wiley & Sons, London, 1974), pp. 455.

[146] R. Becker, "Fourier-transformed Infrarotspektroskopie an polymeren Langmuir-Blodgett Filmen", *Diplomarbeit thesis, Heidelberg, 1992.*

[147] E. Delamarche, B. Michel, H. Kang and C. Gerber, Langmuir **10**, 4103 (1994).

[148] D. R. Jung and A. W. Czanderna, Critical Reviews in Solid State and Materials Sciences **19**, 54 (1994).

[149] Y. Kuk, D. K. Kim, Y. D. Suh, K. H. Park, H. P. Noh, S. J. Oh and S. K. Kim, Phys. Rev. Lett. **70**, 1948 (1993).

[150] R. R. Chance, A. Prock and R. Silbey,"Molecular fluorescence and energy transfer near interfaces", in *Advances in chemical physics* , 37, S. A. R. I. Prigogine, Eds. (John Wiley and Sons, New York, 1978), pp. 1.

[151] H. Ehrenreich and H. R. Philipp, Phys. Rev. **15**, 1622 (1962).

[152] E. I. Altman and R. J. Colton, Surf. Sci. **279**, 49 (1992).

[153] A. J. Maxwell, P. A. Brühwiler, A. Nilsson, N. Mårtensson and P. Rudolf, Phys. Rev. B **49**, 10717 (1994).

[154] T. R. Ohno, Y. Chen, S. E. Harvey, G. H. Kroll, J. H. Weaver, R. E. Haufler and R. E. Smalley, Phys. Rev. B **44**, 13747 (1991).

[155] F. Hache, Ph.D thesis, Université de Paris, 1988.

[156] T. Förster,"Modern Quantum Chemistry", in *Modern Quantum Chemistry* , III, O. Sinanoglu, Eds. (Academic Press, New York, 1965), .

[157] H. Kuhn, J. Photochem. **10**, 111 (1979).

[158] J. Frenkel, Phys. Rev. **36**, 1604 (1930).

[159] P. Ye and Y. R. Shen, Phys. Rev. B **28**, 4288 (1983).

117

CURRICULUM VITAE

Name:	René L. Becker
Age:	30
Date of Birth:	25.4.1966
Nationality:	German
Marital Status:	Married
Home Address:	Av Druey 14bis
	CH-1018 Lausanne
	Switzerland

SECONDARY EDUCATION:

Aug. 1976 - May 1985   Aloisiuskolleg, Bonn-Bad Godesberg, Germany

Oct. 1985 - Dec. 1986   National service

UNIVERSITY EDUCATION:

Oct. 1986 - Sept. 1988   Studies in Physics at the Friedrich-Wilhelms University, Bonn, Germany

Oct. 1988 - July 1990   Graduate studies in Physics at the Ruprecht-Karls University, Heidelberg, Germany

Oct. 1990 - July 1991   Postgraduate studies in Surface Science (M.Sc.) at the Interdisci-plinary Research Centre for Surface Science, Liverpool

Aug. 1991 - Nov. 1992   Diploma in Physics at the 'Institut für Angewandte Physikalische Chemie', Heidelberg University

Jan. 1993 - May 1996   PhD project at the 'Institut de Physique Expérimentale, 'Ecole Polytechnique Fédérale de Lausanne'   funded by the 'Deutschen Akademischen Austauschdienstes' (DAAD)

Remerciements

A tous ceux qui ont contribué à l'élaboration de cette thèse:
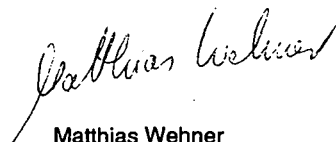
Vorwort

Die hier vorgestellte Arbeit entstand während meiner Tätigkeit am Laboratoire de Thermique Appliquée et de Turbomachines an der École Polytechnique Fédérale de Lausanne (EPFL), im Rahmen des Projektes "Spaltströmung im Turbinenspitzenschnitt". Für dessen Finanzierung danke ich der Asea Brown Boveri AG in Baden (ABB) sowie dem Nationalen Energie-Forschungs-Fond (NEFF).

Zum Abschluß einer solchen Arbeit hält man gerne Rückschau und blickt auf den Anfang zurück. Ich erinnere mich, wie Herr Professor Dr. A. Bölcs zu Beginn unterstrich, daß zum Gelingen einer solchen Arbeit, neben fachlichen Kenntnissen vor allem Durchhaltevermögen erforderlich ist. Hierin kann ich Ihm heute zustimmen. Insbesondere eine experimentelle Arbeit erfordert immer wieder das Bewältigen von Rückschlägen, ein großes Maß an Beharrlichkeit und die Bereitschaft von neuem zu beginnen.

An dieser Stelle möchte ich daher allen meinen herzlichsten Dank aussprechen, die zum Gelingen dieser Arbeit beigetragen haben. Herrn Professor Dr. A. Bölcs möchte ich für seine fachliche Unterstützung danken. Für die technische Betreuung des Projektes sei den Herren Dr. J. Bütikofer, Dr. B. Schönung und C. Mumm, von der Abteilung Dampfturbinen, der ABB Kraftwerke AG in Baden gedankt. Für die Durchführung der numerischen Rechnungen mit unstrukturiertem Netz danke ich Herrn Dr. C. Hustad. Herrn Prof. Dr. J. Denton, Cambridge, der während eines Aufenthaltes sein Programm an die Lavaldüsengeometrie anpaßte, sei ebenfalls gedankt.

Nachdrücklich gedankt sei weiterhin den Mechanikern, für die sorgfältig ausgeführten Arbeiten, meinen Kollegen, für das angenehme Betriebsklima und die gute Zusammenarbeit sowie der Sekretärin und "guten Seele" des Labors, Frau Annick Despont, die sehr zum reibungslosen Betrieb des Labors beiträgt.

Eine wichtige Hilfe, in Form von Motivation und Ansporn wurde mir von Seiten meiner Frau Andrea und meiner beiden Kinder Marie und Leo zuteil, wofür Ihnen ebenfalls herzlich gedankt sei.

Lausanne, im Mai 1996   Matthias Wehner

II